UNIVERSITY OF CALGARY

High-Resolution Infrared Spectroscopy of CO_2-Kr and water-CO_2 Complexes in the 3.5-4.3 µm Region

&

Finite Difference Time Domain Analysis of Grating Coupled Silicon-on-Sapphire Microring Resonators

by

Travis Gartner

A THESIS

SUBMITTED TO THE FACULTY OF GRADUATE STUDIES

IN PARTIAL FULFILMENT OF THE REQUIREMENTS FOR THE

DEGREE OF MASTER OF SCIENCE

GRADUATE PROGRAM IN PHYSICS AND ASTRONOMY

CALGARY, ALBERTA

MAY, 2023

Abstract

This thesis is comprised of two parts, the first being a spectroscopic study of the CO_2-Kr complex in the 4.3 μm region with consideration for isotopic splitting and broadening alongside a spectroscopic study of water-CO_2 complexes in the 3.5-4.3 μm region with consideration for tunnelling splitting due to internal rotation. The second part comprises a finite difference time domain study of grating coupled silicon-on-sapphire microring resonators for use at 4.28 μm.

The infrared spectrum of the CO_2-Kr complex is studied in the region of the carbon dioxide ν_3 fundamental vibration (~2350 cm^{-1}). Tunable IR radiation from an OPO is employed to record absorption spectrum of the complex generated in a pulsed supersonic slit jet. The spectrum exhibits broadening and splitting of transitions due to mass dependence of the five Kr isotopes with natural abundances exceeding 2%. Good simulation of the spectrum is achieved by scaling the vibrational and rotational parameters. This scaling model is particularly important for the combination band involving the intermolecular bending mode where many isotope splittings are observed. As with other CO_2-rare gas complexes, we also observe weak hot bands of CO_2-Kr transitions corresponding to the hot band originating in the CO_2 intramolecular bend. From these we determine a splitting of 1.418 cm^{-1} between the in-plane and out-of-plane bend of CO_2, due to the neighboring Kr atom.

Spectra of water - CO_2 dimers are also studied using a tunable mid-infrared source to probe a pulsed slit jet supersonic expansion. H_2O-CO_2 and D_2O-CO_2 are observed in the CO_2 ν_3 fundamental region (~2350 cm^{-1}), D_2O-CO_2 is also observed in the D_2O ν_3 fundamental region (~2790 cm^{-1}), and HDO-CO_2 is observed in the HDO O-D stretch fundamental region (~2720 cm^{-1}), all for the first time in these regions. Analysis of the spectra yields excited state rotational

parameters and vibrational shifts. Most importantly, they also yield the first experimental values of the ground state internal rotation tunneling splittings for D_2O-CO_2 (0.003 cm^{-1}) and HDO-CO_2 (0.0234 cm^{-1}). The latter value is a direct determination made possible by the reduced symmetry of HDO-CO_2. These results provide stringent and easily interpreted tests for theoretical water - CO_2 potential energy surface calculations.

A finite difference time domain (FDTD) study of silicon-on-sapphire (SoS) ring resonators is conducted. In this study a modal analysis is conducted in COMSOL Multiphysics which resolves the effective mode distribution of varying geometries of air clad SoS waveguides. This modal analysis comprises the calculation of the effective mode index of the waveguides, group index, evanescent field ratio, and interaction parameter in consideration for the waveguide's suitability as a trace gas sensor for carbon dioxide. Three-dimensional ring resonator structures are simulated in COMSOL and the resulting resonance spectrum is presented with quality factors as high as ~51,000. The ring resonator is deigned to overlap CO_2 absorptions near the 4275 nm mark. Fully etched grating couplers on the SoS wafer platform are designed and optimized in the Ansys Lumerical software suite by apodizing both the period and fill factor of the gratings; optimization of the structure is carried out by means of a python-based minimization gradient algorithm. The resulting structures have a theoretical coupling efficiency of ~40% for vertically incident free space light. A mask layout is generated by means of a python based script which places grating optimized structures from Lumerical onto a 9mm x 9mm chip area. An initial manufacturing run was conducted by Applied Nanotools and the resulting chip is currently undergoing laboratory testing and characterization efforts.

Table of Contents

List of Tables

List of Illustrations, Figures, and Graphics

Part I

High-Resolution Infrared Spectroscopy of van der Waals Clusters of CO_2-Kr and water-CO_2 (water = H_2O, D_2O, HDO) in the 3.5-4.3 μm Region

1. Introduction

1.1 Weak Intermolecular Forces

Intermolecular forces are the attractive and repulsive forces between atoms and molecules that give rise to countless natural phenomena. These forces are responsible for the physical and chemical characteristics of substances such as shape, viscosity, boiling point, and surface tension, among others. They are directly responsible for the dynamics of events such as aerosol formation [1], protein folding [2], and molecular adsorption [3]. Strong intermolecular interactions, such as ionic and covalent bonding, result in an attraction between atoms and molecules that act either through the electrostatic attraction (and repulsion) between permanently charged bodies (ionic) or through the direct sharing of electrons (covalent). These types of intermolecular forces are relatively hard to "break" even when the system in question is subject to significant thermal agitation. For instance, the lattice network of a diamond, one of the worlds hardest natural substances, is made of a structure of covalently bonded carbon atoms. The widely distributed electron cloud of the carbon atoms in the diamond lattice results in bonds almost impervious to thermal breakage as well as extremely high surface tension (which is why its hard to scratch a diamond) and melting points. These types of "strong" interactions occur over very small distances, down to the order of picometers (10^{-12} m). Conversely, there is a subset of "weak" intermolecular forces that govern molecular dynamics at larger distances (on the order of nanometers, 10^{-9} m) that are not dependent on the electronic state of the bodies interacting. These types of forces are called the van der Waals forces, named after the Dutch physicist Johannes Diderik van der Waals and were first discovered in the late 1800's [4]. Van der Waals forces arise due to the interactions of electronically neutral atoms and molecules, the strength of which is highly dependent on the interaction distance between the bodies. The three commonly referred to types of van der Waals

forces are listed below in Table 1.1. The type of van der Waals interaction depends on the polarized state of the atoms/molecules in question and whether they have a permanent or induced multipole.

Table 1.1: Types of van der Waals forces

Van der Waals Force	Description
Keesom Interactions [5]	Electrostatic interaction between permanent multipoles in molecules (eg. ionic and polar molecules)
Debye Force [6]	Interaction between a permanent multipole and an induced multipole in molecules
London Dispersion Force [7]	Interaction between (or due to) instantaneous multipoles in molecules due to electron cloud dynamics

Numerous factors can affect the relative strength of the van der Waals interaction, these include the number of electrons present in the molecule, as the polarizability of the molecule is proportional to the strength of its possible charge centre. The shape of the molecule also plays a role in its interaction strength with long, unbranched molecules benefitting from stronger dispersion forces due to the ease with which they are instantaneously polarized. Van der Waals forces are also additive, meaning that localization of a charge center leads to a larger interaction strength. An example of this is the ubiquitous “microfibre” cloth which exploits this attribute by localizing millions of micrometer/nanometer thick fibres into an array, with each one “sticking” to dirt particles as the cloth is wiped over a surface. While the interaction strength of a single fibre and dirt particle is small, the overall strength of the additive interaction of all the fibres results in a strong (relatively speaking) van der Waals interaction with the dust particles that allows the cloth to pick up and hold better than a traditionally woven material of larger fibre size.

The behavior of van der Waals forces are highly dependent on the intermolecular distance of the interaction. At longer distances the forces are attractive and fall into the categories listed in Table 1. At short distances the forces become repulsive due to either the direct repulsion of positive charge centers in atomic nuclei or the overlap of transient negative charge centers in the electron clouds of the molecules. At extremely long distances the interaction strength of the van der Waals force becomes extremely weak and does not play a role in molecular dynamics (>10 Å). The molecular dynamics of the van der Waals forces can be approximated, in their simplest form, by the Lennard-Jones potential, which models one-dimensional pairwise interactions between neutral atoms or molecules. The strength of the Lennard-Jones potential function is proportional to $\frac{1}{r^6}$, where r is the intermolecular distance between the interacting particles. It is formulated as [8]:

$$V = 4\varepsilon[(\frac{\sigma}{r})^{12} - (\frac{\sigma}{r})^{6}] \tag{1.1}$$

where ε is the depth of the Lennard-Jones potential well and σ is the intermolecular distance where the potential is zero. The resulting shape of the potential function is shown in Figure 1.1 below.

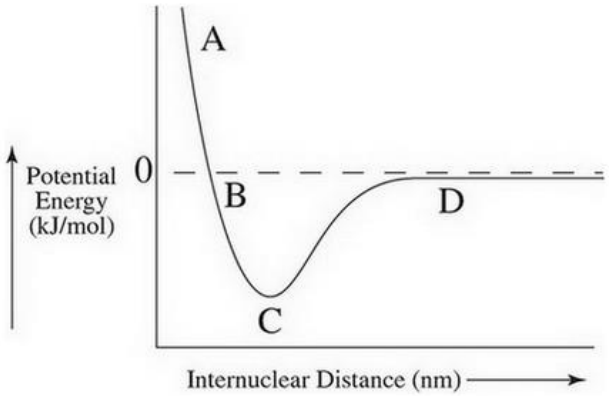

Figure 1.1: Graph of the Lennard-Jones potential

From Figure 1.1 we can see that Section A denotes the repulsive portion of the potential as the intermolecular distance between particles approaches zero. Section B denotes attraction between the particles as the van der Waals forces dominate and bonds form at point C. The distance between the bottom of the well (Point C) and the dashed line is proportional to the binding energy of the molecule and in this section of the potential the molecule exists in a discrete set of bound energy states. As the intermolecular distance increases, we know that the potential drops off as $\frac{1}{r^6}$, so the potential quickly approaches zero at long distances and the interaction no longer occurs (eg. total energy approaches zero and the molecule enters an unbound state). At room temperature thermal agitations of the molecules undergoing a van der Waals interaction are enough to separate the particles to sufficient distance that the interaction completely breaks down, which determines that this type of molecular clustering will not stabilize at high temperatures. This is why, in part, CO_2 molecules in air do not bond and form a solid at ambient temperature; thermal energy in the motion of the particles is greater than any possible van der Waals forces present between CO_2 molecules. Because of the potential dynamics listed above, van der Waals forces are frequently referred to as "non-permanent" forces and thus do not possess a direction as the transient nature of the interaction is usually extremely short lived.

To study these interactions in a laboratory setting the molecules must be sufficiently cooled in their translational, rotational, and vibrational degrees of freedom such that thermal motion is reduced to the point where van der Waals forces dominate the intermolecular interaction and clusters can be formed for long enough periods to study. This is achieved using a supersonic jet expansion; a method used to create weakly bound molecular clusters by means of a high-pressure gas expansion through an orifice into a low-pressure vacuum chamber. Theory behind this methodology can be found in Section 3.1.

1.2 Previous Studies on CO_2-Kr

High resolution spectroscopy of weakly bound van der Waals complexes gives direct information on intermolecular forces and interaction dynamics. Due to the ease with which they are created in a laboratory setting, CO_2-Rg (rare gas) clusters are some of the simplest to study and for which fully coupled intra- and inter-molecular rovibrational calculations are now possible. High resolution infrared spectra of such molecules can validate theoretical molecular dynamics of such systems and provide insight into such phenomena as atmospheric line broadening and protein folding. Determination of rotational and vibrational transitions arising from excitation of molecular energy levels can help to determine the shape and minima of potential energy surfaces for the bound states of such molecules and those of similar shape and composition.

CO_2-Rg clusters are the perfect candidate for study by high resolution spectroscopy, with the first known microwave study of CO_2-Ar being published in 1979 by Steed *et al.* [9] which used molecular beam electric resonance spectroscopy to establish an equilibrium T-shaped structure for the CO_2-Ar complex with the Ar atom located to the side of the CO_2 monomer, adjacent to the C atom; this equilibrium shape would later be validated for the remaining CO_2-Rg clusters in several other studies. Effective intermolecular distances between the C and Rg atoms in the complexes have been determined to range from 3.29 Å for CO_2-Ne [10] to 3.81 Å for CO_2-Xe [11]. Microwave and infrared spectra have been recorded for the CO_2-Rg family extensively since these initial studies with some key contributions as follows; CO_2-He [12], -Ne [13], -Ar [14], and -Xe [15]. Furthermore, the $(CO_2)_2$-Rg and CO_2-$(Rg)_2$ trimers have also been studied with infrared spectra for $(CO_2)_2$-Ne/Ar/Kr/Xe reported in the ν_3 region (2350 cm^{-1}) [16] and spectra for CO_2-$(Ne/Ar/Kr/Xe)_2$ recorded in the ν_3 region as well as in the combination band region (2377 cm^{-1})

[17]. The CO_2-$(Rg)_2$ trimer study incorporates a model for the isotopic dependence of the $(Rg)_2$ dimer atoms similar for that used in this thesis for CO_2-Kr as outlined in Section 4.1.1.

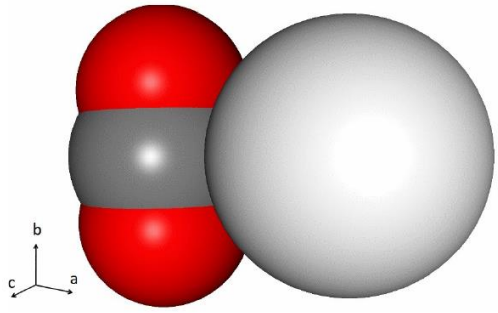

Figure 1.2: Equilibrium configuration of CO_2-Kr and inertial axes

It has been determined by Randall *et al*. [10] and Fraser *et al.* [18] that CO_2-Kr is T-shaped in its equilibrium configuration with an intermolecular distance (C-Kr) of 3.62 Å [10]. CO_2-Kr is thus a non-linear molecule with 3N-6 normal vibrational modes (N is the number of nuclei in the complex) which are listed in Table 1.2 below along with their relative frequencies. A graphical depiction of these vibrational modes can be seen in Figure 1.3.

Table 1.2: Vibrational modes and frequencies of the CO_2-Kr complex

Vibrational Mode	Wavenumber (cm^{-1})
CO_2 v_1 symmetric stretch	~1388
CO_2 v_2 in-plane bend	~667
van der Waals stretch	~32
CO_2 v_2 out-of-plane bend	~667
CO_2 v_3 asymmetric stretch	~2350
Intermolecular bend	~30

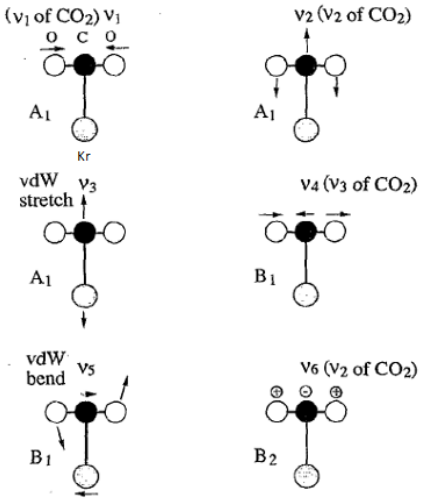

Figure 1.3: Graphical depiction of the vibrational modes of the CO_2-Kr complex. Graphic adapted from [29]

Fraser *et al.* [18] have reported microwave and infrared spectra of the CO_2-Kr complex in in the CO_2 $\nu_1+\nu_3$ (3700 cm^{-1}) and $2\nu_2+\nu_3$ (3600 cm^{-1}) regions by means of pulsed-nozzle Fourier-transform spectroscopy while Randall *et al.* [10] have reported spectra in the CO_2 ν_3 fundamental region (2350 cm^{-1}) by probing a pulsed molecular beam using a diode laser. Later on Iida *et al*. [19] and Konno *et al*. [20] reported microwave (CO_2-Kr) and infrared spectra ($^{12}C^{18}O_2$-Kr) in the CO_2 ν_3 region (2314 cm^{-1}) by means of pulsed-nozzle Fourier transform spectroscopy and using diode lasers, respectively. Of all the transitions reported in these studies only a handful of microwave transitions are attributable to the various isotopes of the Kr atom in the CO_2-Kr complex; Fraser *et al*. measured some K=0 transitions involving the ^{82}Kr, ^{84}Kr, ^{86}Kr isotopes while Iida *et al.* reported a handful of transitions attributable for the K=0, 2 subbands in ^{84}Kr. To date there have been no infrared studies which explore the isotopic dependence of Kr in the CO_2-Kr complex.

1.3 Previous Studies on water-CO_2

Water and carbon dioxide molecules exist in abundance on our planet and are responsible for a plethora of natural phenomena that govern the world around us. Living organisms depend on both water and carbon dioxide for direct sustenance and respiration and both molecules are important for innumerable industrial processes that define our daily life. Our atmosphere is made up of anywhere from 0-4% water vapor and roughly 0.04% carbon dioxide, although these quantities are constantly in flux due to both natural processes and man-made industrial processes that emit and sequester both as by-products. Understanding and quantization of the possible interactions between these two molecules is of the utmost importance as we move to understand humanity's impact on the natural world, determining, for instance, how emission of CO_2 as a greenhouse gas effects atmospheric warming and ocean solvation.

The spectrum of the CO_2-H_2O/D_2O/HDO complexes were first studied in the microwave region by Peterson *et al.* [21] in 1984 by means of molecular-beam-electronic-resonance spectroscopy. This study determined two important characteristics of these complexes; firstly, it was determined that the complex was planar in orientation with a T-shape hinged on the CO_2 unit, while the water monomer was determined to be O-bonded to the C atom along the *a*-inertial axis of the molecule. Figure 1.4 below shows the equilibrium configuration for the complex.

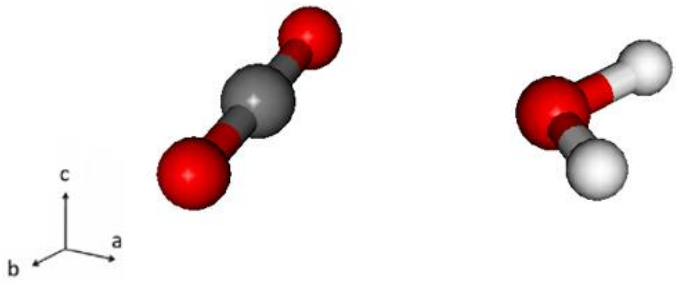

Figure 1.4: Equilibrium configuration of CO_2-H_2O and inertial axes

Secondly it was shown that internal rotations of the monomers around this axis were possible which would give way to tunnelling splittings of the energy levels due to the symmetry of the identical atoms about this axis (O in the CO_2 unit, H in the H_2O unit; likewise for D in D_2O monomer). Block *et al*. [22] later studied this complex (along with water-acetylene) in the infrared region (~3μm) by means of optothermal detection in the O-H asymmetric stretch region of the water unit. This gave a direct measurement of the tunnelling splittings due to internal rotation of the momoners of 0.1356 cm^{-1} and a potential barrier height to tunnelling of 305 cm^{-1}. Columberg *et al.* [23] then studied the microwave spectra of all three complexes via pulsed nozzle Fourier-transform microwave spectroscopy. They determined a potential barrier height of 305.3 cm^{-1} for the water and deuterium complexes but were not able to obtain these values for the HDO bonded isotopomer. Further studies of the complex include the Lauzin *et al.* [24] and Bogomov *et al.* [25] assignment of the CO_2-H_2O complex in the 2OH overtone range (1.4μm) by means of a supersonic jet expansion via cavity ring down spectroscopy as well as Andersen *et al.'s* [26] THz absorption spectrum study of CO_2-H_2O in the intermolecular ν_2 bend region of water (60-180cm^{-1}) observing the out-of-plane wagging, in-plane rocking and torsional motion of the water monomer via a neon matrix setup. Lastly, Felker *et al.* [27] carried out 5-dimensional (5D) quantum bound state calculations for the water and deuterium containing isotopomers for the total angular momentum values J=0, 1, 2 determining a tunnelling splitting of the lowest rotational state of the complexes ($A_1' \rightarrow A_1''$) of 0.1447 cm^{-1} for CO_2-H_2O and 0.0039 cm^{-1} for CO_2-D_2O

1.4 Present Work

This thesis provides an in-depth report of the rovibrational spectra of the CO_2-Kr and CO_2-H_2O/D_2O/HDO complexes in the 3.5-4.3μm region. The CO_2-Kr complex is examined in the region of the CO_2 ν_3 fundamental stretch (2350 cm^{-1}) along with previously recorded microwave

data with account for a parametrized dependence of the isotopic mass of the Kr atom. Also observed, for the first time, is the combination band involving the intermolecular bend as well as the "hot band" corresponding to the CO_2 $(01^11)\leftarrow(01^10)$ transition. The CO_2-H_2O/D_2O complexes are explored, for the first time, in the region of the CO_2 ν_3 fundamental (2350 cm^{-1}) by means of a supersonic jet expansion probed by a tunable Optical Parametric Oscillator (OPO) mid-infrared source. CO_2-D_2O is studied in the region of the D_2O ν_3 fundamental (2720 cm^{-1}) and lastly CO_2-HDO is studied in the OD stretching region (2700cm^{-1}). Studies of the CO_2-H_2O/D_2O/HDO complexes account for the tunnelling splitting of energy states resulting from the permutations of identical nuclei in the complexes due to internal monomer rotation. Derivation of the relevant theoretical background necessary for the assignment of rovibrational transitions in these complexes is presented in Chapter 2. Chapter 3 will present the experimental setup used to collect and analyze the data in the various spectra. Chapters 4 and 5 will present analysis of the spectra for these complexes and discuss outcomes and next steps for this research.

2. Theoretical Background

2.1 Rigid-Rotor Hamiltonian

In its simplest form the Hamiltonian describing the rotation of a three-dimensional rigid body, such as a molecule, can be written as [28]

$$\hat{H}_{rot} = A\hat{J}_a^2 + B\hat{J}_b^2 + C\hat{J}_c^2 \tag{2.1}$$

where $\hat{J}_i^2$ are the spatial components of the total angular momentum operator $\hat{J}^2$, and a, b, and c are defined as the principal axes of the body such that its moments of inertia (I) about each axis are given as

$$I_a < I_b < I_c \tag{2.2}$$

and A, B, and C are the rotational constants of the body defined as

$$A = \frac{\hbar}{4\pi I_a},\ B = \frac{\hbar}{4\pi I_b},\ C = \frac{\hbar}{4\pi I_c} \tag{2.3}$$

Derivations of the total angular momentum operator $\hat{J}^2$ and its components $\hat{J}_i^2$ can be found in [29] and are omitted here for space. Important definitions, commutation relations and values relating to the total angular momentum operator can be found in Appendix A.

The spatial coordinates (x, y, z) are assigned to the principal axes in one of six possible representations depending on the situation under study. These representations are given in Table 2.1, with *r* and *l* corresponding to right or left-handed coordinate systems respectively.

Table 2.1: Principal axes mapping conventions for the rotational Hamiltonian

	I^r	I^l	II^r	II^l	III^r	III^l
x	b	c	c	a	a	b
y	c	b	a	c	b	a
z	a	a	b	b	c	c

Molecules can be classified as follows based on their moments of inertia about the principal axes:

Table 2.2: Classification of molecules based on moments of inertia about the principal axes

Molecule Type	Axial Relation
Linear	$I_b = I_c, I_a = 0$
Prolate Symmetric Top	$I_a < I_b = I_c$
Oblate Symmetric Top	$I_a = I_b < I_c$
Spherical Top	$I_a = I_b = I_c$
Asymmetric Top	$I_a < I_b < I_c$

Rovibronic energy levels (E_{rve}) for molecules of the various types listed in Table 2.2 can be obtained by solving the time-independent Schrödinger equation for the rigid rotor Hamiltonian, that is, to solve the following

$$\widehat{H}_{rve}|\psi_{rve}\rangle = E_{rve}|\psi_{rve}\rangle \tag{2.4}$$

where ψ_{rve} is the total rovibronic wavefunction of the molecule.

The complexes under investigation in this thesis, CO_2-Kr (and its isotopologues) along with CO_2-H_2O/D_2O/HDO, are planar asymmetric top molecules, and as such the energy levels for an asymmetric top will be derived below. To arrive at these solutions in a meaningful manner we must first explore the energy level calculations for a symmetric top molecule.

2.2 Symmetric Top Energy Level Solutions

The solution to the Schrödinger equation for the prolate symmetric top (in I^r) representation will be provided. A similar method can be used for an oblate symmetric top with $\hat{J}_a$ replaced by $\hat{J}_c$ and k_a replaced by k_c and by adopting III^r representation for the molecule.

For a prolate symmetric top, the axis of symmetry is taken to be the *a*-axis, and I^r representation is used to describe the moments of inertia of the molecule (here $z=a$). The rotational Hamiltonian of a prolate symmetric top can thus be written as follows, noting that for a prolate (oblate) symmetric top $I_b=I_c$ ($I_a=I_b$)

$$\widehat{H}_{rot} = A\hat{J}_a^2 + B(\hat{J}_b^2 + \hat{J}_c^2) \tag{2.5}$$

or

$$\widehat{H}_{rot} = B\hat{J}^2 + (A - B)\hat{J}_z^2 \tag{2.6}$$

The Schrödinger equation becomes

$$\widehat{H}_{rot}|\psi_{rot}\rangle = E_{rot}|\psi_{rot}\rangle \tag{2.6}$$

$$B\hat{J}^2 + (A - B)\hat{J}_z^2|\psi_{rot}\rangle = E_{rot}|\psi_{rot}\rangle \tag{2.7}$$

In I^r representation Equation A.8 (Appendix A) for a prolate symmetric top becomes

$$\left[\widehat{H}_{rot}, \hat{J}_a\right] = i\left(\frac{1}{2I_b} - \frac{1}{2I_c}\right)\left(\hat{J}_b\,\hat{J}_c + \hat{J}_c\hat{J}_b\right) = 0 \quad as\ I_b = I_c \tag{2.8}$$

Thus, $\widehat{H}_{rot}, \hat{J}_a, \hat{J}_Z, and\ \hat{J}^2$ all must share a common set of eigenfunctions, $|J\ k_a\ m\rangle$, where m is the projection of the total angular momentum onto the symmetry axis in the space fixed frame, with the following eigenvalues [29]

$$\widehat{H}_{rot}|J\ k_a\ m\rangle = E_{rot}|J\ k_a\ m\rangle \tag{2.9}$$

$$\hat{J}^2\hbar^2|J\ k_a\ m\rangle = J(J+1)\hbar^2|J\ k_a\ m\rangle \tag{2.10}$$

$$\hat{J}_a\hbar|J\ k_a\ m\rangle = k_a\hbar|J\ k_a\ m\rangle \tag{2.11}$$

$$\hat{J}_Z\hbar|J\ k_a\ m\rangle = m\hbar|J\ k_a\ m\rangle \tag{2.12}$$

Applying equations 2.9-2.12 to equation 2.7 with $|\psi_{rot}\rangle = |J\ k_a\ m\rangle$ one easily arrives at the energy level expression for a prolate symmetric top as

$$E_{rot} = BJ(J+1) + (A-B)\ {k_a}^2 \tag{2.13}$$

Similarly, for an oblate symmetric top, one obtains the following

$$E_{rot} = BJ(J+1) + (B-C)\ {k_c}^2 \tag{2.14}$$

For a symmetric top each energy level labelled by a value of *J* will have *(2J+1)* states corresponding to the value of k_a while each state labelled by a value of *(J, k_a)* will have *(2J+1)* states corresponding to the value of *m*. This leads to a *2(2J+1)* fold degeneracy for symmetric top energy states for $K_a \neq 0$ and *(2J+1)* for $K_a=0$.

2.3 Asymmetric Top Molecules

In the case of asymmetric top molecules rotational motion cannot be described in terms of a conserved motion about an axis of the molecule [28, 29], this means that the rotational constants, A, B, and C, have distinct values. This implies that $\widehat{H}_{rot}$ does not commute with $\hat{J}_z$, as is the case for a symmetric top molecule (equation 2.8), as its moments of inertia about each principal axis are different (Table 2.2). As such, k_a (or k_c), the prolate (oblate) symmetric top quantum number for the projection of the total angular momentum onto the symmetry axis of the molecule in the

molecule-fixed frame, may not be considered a "good" quantum number, but rather a label. To solve the Schrödinger equation for an asymmetric top molecule one must use symmetric top wavefunctions as the basis set of the Hamiltonian and diagonalize it to find the associated energies. The rotational Hamiltonian for an asymmetric top is written as [29]

$$\widehat{H}_{rot} = \frac{B+C}{2}\hat{J}^2 + \left(A - \frac{B+C}{2}\right)\hat{J}_z^2 + \frac{B-C}{4}[\,(\hat{J}_m^+)^2 + \,(\hat{J}_m^-)^2] \tag{2.15}$$

Where $\hat{J}_m^{\pm}$ are the angular momentum ladder operators in the molecule fixed frame, whose properties are given below. Choosing the basis set for a prolate symmetric top (eg. z=a), one can see that the only non-vanishing elements of the asymmetric top Hamiltonian are found to be:

$$\langle J\ k_a|\hat{J}^2|J\ k_a\rangle = J(J+1) \tag{2.16}$$

$$\langle J\ k_a|\,\hat{J}_z^2|J\ k_a\rangle = \ k_a^2 \tag{2.17}$$

$$\langle J\ k_a \pm 2|\widehat{J}_m^{\mp})^2|J\ k_a\rangle = \sqrt{[J(J+1) - \ k_a(\,k_a \pm 1)]\,[J(J+1) - (\,k_a \pm 1)(\,k_a \pm 2)]} \tag{2.18}$$

As $-J \le k_a \le +J$ it is easy to see that all matrix elements vanish for the $J = 0$ block of the Hamiltonian and as such $E_{rot}\ (J = 0) = 0$. For $J = 1$, the Hamiltonian takes the form [29]:

$$\widehat{H}_{rot} = \begin{matrix} \\ \langle 1-1| \\ \langle 1\,0| \\ \langle 1+1| \end{matrix} \begin{matrix} \begin{matrix} |1-1\rangle & |1\,0\rangle & |1+1\rangle \end{matrix} \\ \begin{pmatrix} C + \frac{A+B}{2} & 0 & \frac{A-B}{2} \\ 0 & A+B & 0 \\ \frac{A-B}{2} & 0 & C + \frac{A+B}{2} \end{pmatrix} \end{matrix} \leftrightarrow \widehat{H}_{rot} = \begin{matrix} \\ \langle 1-1| \\ \langle 1+1| \\ \langle 1\,0| \end{matrix} \begin{matrix} \begin{matrix} |1-1\rangle & |1+1\rangle & |1\,0\rangle \end{matrix} \\ \begin{pmatrix} C + \frac{A+B}{2} & \frac{A-B}{2} & 0 \\ \frac{A-B}{2} & C + \frac{A+B}{2} & 0 \\ 0 & 0 & A+B \end{pmatrix} \end{matrix} \tag{2.19}$$

The top left 2x2 block of the block diagonalized Hamiltonian (2.19), yields the eigenvalue problem

$$\begin{vmatrix} C + \frac{A+B}{2} - \ \lambda & \frac{A-B}{2} \\ \frac{A-B}{2} & C + \frac{A+B}{2} - \ \lambda \end{vmatrix} = 0 \tag{2.20}$$

The solutions of (2.20) are the energy eigenvalues $\lambda = A + B,\ \lambda = B + C$. Thus, the three solutions for the $J = 1$ block are $A + B, A + C$ and $B + C$. Labelling of the energy levels for the asymmetric top is done via a correlation diagram that connects the energies of a prolate symmetric top with an oblate symmetric top. Figure 2.1 below shows the correlation diagram for an asymmetric top

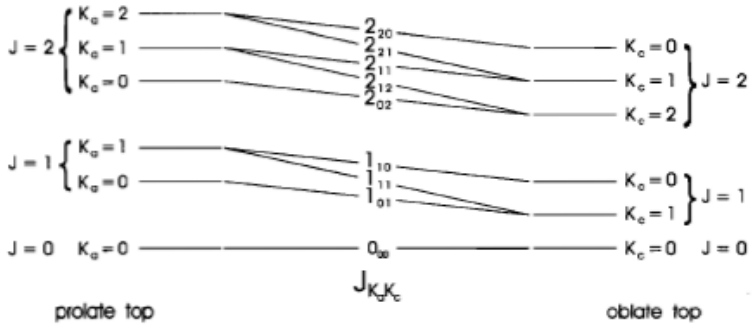

Figure 2.1: Asymmetric top – symmetric top energy level correlation diagram [29]

Note that from the outcomes for a symmetric top we see for a prolate top $(A - B) > 0$ and for an oblate top $(C - B) < 0$, so as k_a increases rotational energy for a prolate top increase while as k_c increases the rotational energy for an oblate top decrease. Calculating asymmetric top rotational energy levels for increasing values of *J* becomes a numeric exercise due to the growing size of the Hamiltonian matrix. Table 2.3 below shows the outcomes for the first few values of the rotational angular momentum *J*.

Table 2.3: Asymmetric top energy levels for values of J = 0, 1, 2

J_{kakc}	$E(J_{kakc})$
0_{00}	0
1_{10}	A + B
1_{11}	A + C
1_{01}	B + C
2_{20}	$2A + 2B + 2C + 2[(B-C)^2 + (A-C)(A-B)]^{1/2}$
2_{21}	4A + B + C
2_{11}	A + 4B + C
2_{12}	A + B + 4C
2_{02}	$2A + 2B + 2C - 2[(B-C)_2 + (A-C)(A-B)]^{1/2}$

2.4 Centrifugal (Higher Order) Distortion Terms

The bonds between atoms in a molecule are not perfectly rigid but distort due to centrifugal forces created as the molecule rotates. This results in the addition of higher order centrifugal distortion terms in the rotational energy expression for polyatomic molecules. This transforms the rotational energy expression for the prolate symmetric top into the following [29]

$$E_{rot} = BJ(J+1) + (A-B)K^2 - D_J[J(J+1)]^2 - D_K K^4 - D_{JK}J(J+1)K^2 \qquad (2.21)$$

Where D_J, D_K, D_{JK} are the diagonal centrifugal distortion terms arising out of the solution to the Schrodinger equation. Similar terms apply in the case of an asymmetric top, which, to higher order is given as [28]

$$\hat{H}_{rot} = \frac{B+C}{2}\hat{J}^2 + \left(A - \frac{B+C}{2}\right)\hat{J}_z^2 + \frac{B-C}{4}[\,(\hat{J}_m^+)^2 + \,(\hat{J}_m^-)^2] - D_J\hat{J}^4 - D_{JK}\hat{J}^4\hat{J}_z^2 + D_K\hat{J}_z^4 +$$

$$\delta_J\hat{J}^2[\,(\hat{J}_m^+)^2 + \,(\hat{J}_m^-)^2] + \delta_k[\,(\hat{J}_m^+)^4 + \,(\hat{J}_m^-)^4] \qquad (2.22)$$

Where δ_k and δ_J are off-diagonal quartic centrifugal constants.

2.5 Symmetry

A classification of the energy levels of a molecule can be obtained from its symmetry group. The symmetry group of a molecule is a group whose elements commute with the Hamiltonian of the molecule and can help classify the symmetry of the energy levels of the molecule using the groups character table. The symmetry group of a molecule is called its Complete Nuclear Permutation Inversion (CNPI) group, which contains all possible ways to permute and invert identical atoms within the molecular structure. While this is the most complete group for determining energy states of a molecule based on its symmetry it can allow for permutations of the atoms which "break" bonds in the structure in its equilibrium configuration, and as such may not be entirely representative of the true orientation of the molecule under the group operations. The molecular symmetry group (MS) of a molecule is a subgroup of the CNPI that removes such infeasible operations and leaves behind only those which do not alter the equilibrium configuration (and thus energy) of the molecule. It is this symmetry group which is used in the symmetry classification of energy states and possible transitions for the molecule.

CO_2-Kr is an asymmetric top molecule, T-shaped in its equilibrium configuration, and belongs to the C_{2v} point group. The C_{2v} point group possesses four symmetry elements, which are identified in the character table for this group shown below. They are the identity operator (E), the 2-fold rotational symmetry axis (C_{2a}), and two reflection planes (σ_{ab}, σ_{ac}). These symmetry elements act on the nuclear coordinates of the atoms in the molecule. Note that the C_{2v} point group is isomorphic to the C_{2v} (MS) group as well as the group of equivalent rotations which act on the Euler angles defining molecular coordinates. These three isomorphisms can be seen in Table 2.4 below. The character table is the characters of irreducible representations of the symmetry of the

molecule using Mulliken Notation, where label A (Γ =+1) is symmetric about the principal axis of rotation and B (Γ =-1) is antisymmetric.

Table 2.4: Character table for the C_{2v} symmetry group

	C_{2v} (M)	E	(12)	E*	(12)*			
	Eq. Rot.	R^0	R^{π}_a	R^{π}_c	R^{π}_b			
	C_{2v}	E	C_{2a}	σ_{ab}	σ_{ac}	Axis	Rotation	Translation
Γ (symmetry species)	A_1	1	1	1	1	a		T_a
	A_2	1	1	-1	-1		R_a	
	B_1	1	-1	-1	1	c	R_b	T_c
	B_2	1	-1	1	-1	b	R_c	T_b

In the table above the operation E is known as the identity operator and leaves all nuclear coordinates unchanged. (12) permutes identical atoms labelled 1 and 2 respectively; these are the two O-atoms in CO_2-Kr. E* inverts all nuclear coordinates in the molecule.

CO_2-HDO is also a planar molecule, T-shaped at the CO_2 unit and O-bonded to the HDO unit with the H and D molecules "bending" away from the CO_2 monomer. This complex possesses G_4 symmetry as shown in Table 2.5.

Table 2.5: Character table for the G_4 symmetry group

	Eq. Rot.	R^0	R^{π}_a	R^{π}_c	R^{π}_b			
	G_4	E	(34)	E*	(34)*	Axis	Rotation	Translation
Γ (symmetry species)	A_1	1	1	1	1	a		T_a
	A_2	1	1	-1	-1		R_a	
	B_1	1	-1	-1	1	c	R_b	T_c
	B_2	1	-1	1	-1	b	R_c	T_b

In the table above the operation (34) permutes the identical oxygen atoms in the CO_2 monomer in the CO_2-HDO complex.

CO_2-H_2O/D_2O complexes belong to the G_8 isometric symmetry group. This group possesses eight symmetry operations including the permutations (12), switching identical hydrogen/deuterium nuclei, (34), switching oxygens in the CO_2 monomer, and (12)(34) which is the successive permutation of atoms 1 and 2 followed by atoms 3 and 4. The character table for G_8 is listed below.

Table 2.6: Character table for the G_8 symmetry group

	G_8	E	(12)(34)	E*	(12)(34)*	(12)	(34)	(12)*	(34)*			
	Eq. Rot.	R^0	R^{π}_z	R^{π}_y	R^{π}_x	R^0	R^{π}_z	R^{π}_y	R^{π}_x	Axis	Rotation	Translation
Γ (symmetry species)	A_1'	1	1	1	1	1	1	1	1	z		T_z
	A_2'	1	1	-1	-1	1	1	-1	-1		R_z	
	B_1'	1	-1	-1	1	1	-1	-1	1	y	R_x	T_y
	B_2'	1	-1	1	-1	1	-1	1	-1	x	R_y	T_x
	A_1''	1	1	1	1	-1	-1	-1	-1			
	A_2''	1	1	-1	-1	-1	-1	1	1			
	B_1''	1	-1	-1	1	-1	1	1	-1			
	B_2''	1	-1	1	-1	-1	1	-1	1			

2.5.1 Symmetry of the Vibrational Modes of CO_2-Kr

CO_2-Kr is a non-linear molecule with *(3N-6)* modes of vibration, *N* being the number of atoms in the molecule. Theses modes are depicted graphically in Figure 1.3. To determine the modes of vibration of the CO_2-Kr molecule each atom in the molecule is assigned a three-dimensional cartesian displacement vector (Δa, Δb, Δc) (or (Δx, Δy, Δz) in general cartesian coordinates) related to its spatial coordinates in the I^r representation. The symmetry operations of the C_{2v} group are applied to each displacement vector to determine its character representation. If the displacement vector is unchanged by the operation, it is assigned a +1 character, 0 if it is moved, and -1 if the vector is reversed. Table 2.7 below shows the 12-dimensional reducible cartesian representation of the group for CO_2-Kr.

Table 2.7: Reducible cartesian representation of CO_2-Kr under C_{2v} symmetry operations

C_{2v}	E	C_{2a}	σ_{ab}	σ_{ac}
Γ	12	-2	4	2

This representation can be written in terms of the irreducible representations of the C_{2v} (MS) group using the following reduction formula [29]:

$$a_n = \frac{1}{h}\sum_x \chi_r^x \chi_i^x n^x \tag{2.23}$$

Where,

a_n = number of symmetry species *n* present

h = order of the symmetry group (number of symmetry elements)

n^x = number of operations in the class (from character table)

χ^x_r = character of the reducible representation

χ^x_i = character of the irreducible representation (from character table)

Using this formula to determine the irreducible representation of the CO_2-Kr molecule gives the following:

$$a_{A_1} = ¼ [(12•1•1)+(-2•1•1)+(4•1•1)+(2•1•1)] = 4A_1 \tag{2.24}$$

$$a_{A_2} = ¼ [(12•1•1)+(-2•1•1)+(4•-1•1)+(2•-1•1)] = A_2 \tag{2.25}$$

$$a_{B_1} = ¼ [(12•1•1)+(-2•1•1)+(4•-1•1)+(2•-1•1)] = 3B_1 \tag{2.26}$$

$$a_{B_2} = ¼ [(12•1•1)+(-2•-1•1)+(4•-1•1)+(2•1•1)] = 4B_2 \tag{2.27}$$

From this we determine the total irreducible cartesian representation to be:

$$\Gamma_{cart} = 4A_1+A_2+3B_1+4B_2 \quad (2.28)$$

Cross referencing this with the rotational and translational columns from C_{2v} character table (Table 2.4) we can deduce the symmetries for the translational, rotational, and vibrational representations as follows:

$$\Gamma_{vib} = \Gamma_{cart} - \Gamma_{trans} - \Gamma_{rot} \quad (2.29)$$

$$\Gamma_{trans} = A_1+B_1+B_2 \quad (2.30)$$

$$\Gamma_{rot} = A_2+B_1+B_2 \quad (2.31)$$

$$\Gamma_{vib} = 3A_1+B_1+2B_2 \quad (2.32)$$

We see six modes of vibration for the CO_2-Ar molecule, $\Gamma_{vib} = 3A_1+B_1+2B_2$ as expected. To classify each of these modes we label each bond in the molecule and determine how it is affected by the symmetry operations of the group (with the molecule in the *ab*-plane). The two C-O bonds are labelled r_1 and r_2 respectively, while the C-Kr bond is labelled r_3. This is shown in Table 2.8.

Table 2.8: Symmetries of the bond transformations of CO_2-Kr under C_{2v} operations

C_{2v}	E	C_{2a}	σ_{ab}	σ_{ac}	Symmetry
r_1	r_1	r_2	r_1	r_2	
r_2	r_2	r_1	r_2	r_1	
r_3	r_3	r_3	r_3	r_3	A_1
r_1+r_2	r_1+r_2	r_1+r_2	r_1+r_2	r_1+r_2	A_1
r_1-r_2	r_1-r_2	r_2-r_1	r_1-r_2	r_2-r_1	B_2

Considering how the bonds are affected by the symmetry operations of the group allows us to classify the symmetry of the vibrational modes based on the groups irreducible representations as follows

Table 2.9: Symmetry of the vibrational modes of CO_2-Kr

Vibrational Mode	Symmetry Species (Γ)
CO_2 ν_1 symmetric stretch	A_1
CO_2 ν_2 in-plane bend	A_1
van der Waals stretch	A_1
CO_2 ν_2 out-of-plane bend	B_1
CO_2 ν_3 asymmetric stretch	B_2
Intermolecular bend	B_2

2.5.2 Symmetry of the Vibrational Modes of CO_2-H_2O/D_2O

By the same methodology as above the eighteen-dimensional reducible cartesian representation for CO_2-H_2O/D_2O using the symmetry operations of the G_8 group are listed below. Explicit derivation of this representation can be found in Appendix D. Note that for these complexes the assignment of the inertial axes in I^r representation is $x=b$, $y=c$, $z=a$.

Table 2.10: Reducible cartesian representation of CO_2-H_2O/D_2O under G_8 symmetry operations

G_8	E	(12)(34)	E*	(12)(34)*	(12)	(34)	(12)*	(34)*
Γ	18	-2	6	2	12	-4	4	4

Writing this in terms of the irreducible representations of G_8 via Equation 2.23 we get

$$\Gamma_{cart} = 5A_1' + A_2' + 4B_1' + 5B_2' + A_1'' + A_2'' + B_2'' \tag{2.33}$$

By Equation 2.29, and using the G_8 character table to determine the translational and rotational symmetries of the molecule we arrive at the symmetry of its vibrational modes

$$\Gamma_{vib} = 4A_1' + 2B_1' + 3B_2' + A_1'' + A_2'' + B_2'' \tag{2.34}$$

These complexes are non-linear and should possess *3N-6=12* vibrational modes; indeed, by the reduction formula this is what we find. The assignment of the symmetries for the vibrational modes studied in this thesis are listed below via the transformation of the atomic bonds under the

symmetry operations of the G_8 group. These vibrational modes are the asymmetric stretch of the CO_2 unit (bonds r_3-r_4) and the asymmetric stretch of the H_2O/D_2O unit (bonds r_1-r_2)

Table 2.11: Symmetries of the bond transformations of CO_2-H_2O/D_2O under G_8 operations for the CO_2 and H_2O/D_2O asymmetric stretch

G_8	E	(12)(34)	E*	(12)(34)*	(12)	(34)	(12)*	(34)*	Symmetry
r_1	r_1	r_2	r_1	r_2	r_2	r_1	r_2	r_1	
r_2	r_2	r_1	r_2	r_1	r_1	r_2	r_1	r_2	
r_3	r_3	r_4	r_3	r_4	r_3	r_4	r_3	r_4	
r_4	r_4	r_3	r_4	r_3	r_4	r_3	r_4	r_3	
$\chi(r_1-r_2)$	1	-1	1	-1	-1	1	-1	1	B_2''
$\chi(r_3-r_4)$	1	-1	1	-1	1	-1	1	-1	B_2'

2.5.3 Symmetry of the Vibrational Modes of CO_2-HDO

Strictly speaking CO_2-HDO belongs to a C_s symmetry possessing only the identity element and a reflection plane in which the molecule lies as its symmetry operations. However, to correctly label its rovibronic transitions one must treat it with G_4 symmetry to consider possible permutations of the identical O nuclei in the CO_2 monomer which can lead to tunnelling splittings in the energy levels of the vibrational states [36]. CO_2-HDO is a non-linear molecule with the same equilibrium structure as CO_2-H_2O/D_2O and as such should have *3N-6=12* vibrational modes. Applying the symmetry operations of the G_4 group, where (34) is the interchange of the oxygen atoms in the CO_2 unit and eliminating (12) and associated operations (as the HDO unit does not have any identical atoms), the following reducible cartesian representation is obtained.

Table 2.12: Reducible cartesian representation of CO_2-HDO under G_4 symmetry operations

G_4	E	(34)	E*	(34)*
Γ	18	-2	6	4

In terms of the irreducible representations of the symmetry group this can be written as

$$\Gamma_{cart} = 6A_1 + A_2 + 5B_1 + 6B_2 \quad (2.35)$$

Subtracting the translational and rotational symmetries from the Cartesian representation yields the symmetries of the twelve vibrational modes for CO_2-HDO

$$\Gamma_{vib} = 5A_1 + 3B_1 + 4B_2 \quad (2.36)$$

Labelling the bonds in the complex in the same manner as done for CO_2-H_2O/D_2O, we can label the vibrational state of interest, that of the OD stretch studied here, by its irreducible representation in the G_4 group

Table 2.13: Symmetry of the OD stretching mode of CO_2-HDO

G_4	E	(34)	E*	(34)*	Symmetry
r_{OD}	r_{OD}	r_{OD}	r_{OD}	r_{OD}	A_1

2.5.4 Coriolis Interactions in CO_2-Kr

An object in motion in a frame of reference that rotates with respect to an inertial frame will undergo a Coriolis force perpendicular to the axis of rotation. In a rotating molecule the Coriolis force will affect the energies of vibrational and rotational levels. The effect can significantly change spectral features for doubly degenerate or near-degenerate levels [30]. Teller [31] was the first to show that the Coriolis forces due to each component in a degenerate vibration in a rotating symmetric top molecule lead to an excitation in the other components. Due to the rotation of the molecule, the path of the vibrations (movement of the atoms) take on elliptical shapes rather than straight lines, resulting in an associated angular momentum for each degenerate vibration that interacts with the pure rotational angular momentum of the molecule.

The Coriolis interaction between the vibrational and rotational modes in a molecule can be shown with the addition of an interaction term to the Hamiltonian of the molecule, $\widehat{H}_{corr}$. The derivation of the Coriolis interaction between vibrational levels for symmetric tops can be found

in Appendix C. It is a relatively straight forward exercise as symmetric tops have a preferred symmetry axis.

In the case of an asymmetric top molecule the determination of the interaction term is not as straightforward as there is no preferred axis in the molecule fixed frame. The absence of degenerate symmetry species leads to Coriolis interactions about the three perpendicular axes that can all occur independently [32]. The type of Coriolis interaction between vibrational states in an asymmetric top molecule can be determined from the vibrational selection rule that states the product of the vibrational symmetry species of the interacting states (Γ_v' , Γ_v'') must be the species of the rotation (Γ_R) about this axis [33]. This is given as:

$$\Gamma_v' \otimes \Gamma_v'' = \Gamma_R \tag{2.37}$$

In the case of the degenerate intramolecular bending modes of the CO_2 unit in CO_2-Kr studied in this thesis, the selection rule is as follows,

$$\Gamma_{in-plane} \otimes \Gamma_{out-of-plane} = \Gamma_R \tag{2.38}$$

$$A_1 \otimes B_1 = B_1 \tag{2.39}$$

which determines the species of rotation to be of symmetry B_1, and hence, as seen from the C_{2v} character table, interacting through a rotation about the *b*-axis.

A complete derivation of the Hamiltonian for Coriolis interactions between degenerate vibrational levels can be found in [34]. Of note is the vibrational matrix element for Coriolis interactions about the α-axis which is of the form:

$$\hat{H}_{corr} = -2B_\alpha \xi_{r,s}^\alpha (\hat{Q}_r \hat{p}_s - \hat{Q}_s \hat{p}_r) \hat{J}_\alpha \tag{2.40}$$

Where B_α is the molecular rotational constant associated with the α-axis (α = a, b, or c) , $\xi_{r,s}^{\alpha}$ is the Coriolis interaction term (-1< ξ<1) between vibrational states r and s, $\hat{p}_r$ is the momentum operator associated with the r[th] normal vibrational coordinate $\hat{Q}_r$, and $\hat{J}_\alpha$ is the rotational angular momentum operator about the α-axis. The definition of the rotational operators $\hat{J}_\alpha$ is as follows, expanded in terms of the ladder operators $\hat{J}_+$, $\hat{J}_-$ [34] and the quantum numbers *J* and $K = k_a \; or \; k_c$ depending on choice of inertial representation. Notation of the Wang transformation [35], $|J\; K_\pm\rangle = \frac{1}{\sqrt{2}}[|J\; K\rangle \pm |J{-}K\rangle]$, is also used.

$$\hat{J}_a|J\; K_\pm\rangle = K|J\; K_\mp\rangle \tag{2.41}$$

$$\hat{J}_b|J\; K\pm\rangle = \tfrac{1}{2}[J(J+1) - K(K+1)]^{1/2}|J\;(K+1)\pm\rangle + \tfrac{1}{2}[J(J+1) - K(K-1)]^{1/2}|J\;(K-1)\pm\rangle \tag{2.42}$$

$$\hat{J}_c|J\; K\pm\rangle = \tfrac{-i}{2}[J(J+1) - K(K+1)]^{1/2}|J\;(K+1)\pm\rangle + \tfrac{i}{2}[J(J+1) - K(K-1)]^{1/2}|J\;(K-1)\pm\rangle \tag{2.43}$$

The selection rules have already determined that the symmetry species of the rotation coupling the vibrational modes to be B_1 (around the *b*-axis), thus there will be a *b*-type Coriolis coupling between vibrational states.

The matrix elements of the Coriolis Hamiltonian between the vibrational states *r* (CO_2 in-plane bend) and *s* (CO_2 out-of-plane bend) about the *b*-axis is obtained as follows:

$$\langle J'K'\pm|\langle r=0, s=1|-2B\xi_{r,s}^{b}(\hat{Q}_r\hat{p}_s - \hat{Q}_s\hat{p}_r)\hat{J}_b|r=1, s=0\rangle|J\; K\pm\rangle \tag{2.44}$$

The vibrational coordinate and momentum operators result in a matrix element whose value is one [34]. Thus, only the rotational component is left to operate on the vibrational states giving the matrix elements:

$$-2B\xi_{r,s}^{b}\langle J'K'\pm|\hat{J}_b|J\; K\pm\rangle = \tag{2.45}$$

$$-2B\xi_{r,s}^{b}\{\frac{1}{2}[J(J+1)-K(K+1)]^{\frac{1}{2}}+\frac{1}{2}[J(J+1)-K(K-1)]^{\frac{1}{2}}\} \quad (2.46)$$

From the expression above, both the strength of the interaction parameter $\xi_{r,s}^{b}$and the values of *J* and *K* for a given state will determine how large of an effect the Coriolis coupling between vibrations will have on its energy.

2.5.5 Symmetry Species of Rotational States in CO_2-Kr and water-CO_2

The rotational symmetry species of an asymmetric top molecule are determined by correlating between the rotational symmetries of limiting case prolate and oblate symmetric top molecules as the rotational wavefunctions of the asymmetric top are linear combinations of symmetric top wavefunctions. The result depends on the state of k_a and k_c (whether they are even "e" or odd "o"). The explicit calculations for the determination of the rotational symmetry species of a complex like CO_2-Kr is carried out in Appendix C for completeness. Alternative to the direct calculation of the rotational symmetry species of the wavefunction one may employ what are called the "asymmetric top symmetry rules" for the rotational states of the molecule [28] which assign these states based on the irreducible representations of the symmetry group which satisfy the placement of certain characters based on rotations of π about the three inertial axes of the molecule. These rules state the following:

- "ee" states transform as the totally symmetric representation of the point group (eg. the irreducible representation with a character of +1 for every operation of the group).
- "eo" states transform as the representation with a character of +1 for operation equivalent to the rotation R_a^{π} and -1 for R_b^{π} and R_c^{π}
- "oe" states transform as the representation with a character of +1 for operation equivalent to the rotation R_c^{π} and -1 for R_a^{π} and R_b^{π}

- "oo" states transform as the representation with a character of +1 for operation equivalent to the rotation R_b^π and -1 for R_a^π and R_c^π

Applying either the direct calculation of the rotational symmetry species or the asymmetric top symmetry rules yields the same outcome. For CO_2-Kr and CO_2-HDO, which belong to the $C_{2V}(M)$ and G_4 symmetry groups respectively we obtain (remembering $C_{2V}(M)$ is isomorphic to G_4)

Table 2.14: Rotational symmetry species of CO_2-Kr and CO_2-HDO

Γ_{rot}	$k_a k_c$
A_1	ee
A_2	eo
B_1	oo
B_2	oe

For CO_2-H_2O/D_2O, which belongs to the G_8 molecular symmetry group, we obtain

Table 2.15: Rotational symmetry species of the CO_2-H_2O/D_2O complexes

Γ_{rot}	$k_a k_c$
A_1'	ee
A_2'	eo
B_1'	oo
B_2'	oe

2.5.6 Symmetry of Tunnelling States in water-CO_2

Internal rotation of a group of atoms about a fixed axis resulting in the exchange of identical atoms within the molecule leads to a tunnelling splitting of the possible energy states. If the symmetry group of the molecule is composed of rotations about a fixed axis, then this group must be Abelian and of infinite order (as rotations of all possible angles are possible about the fixed

axis) [37]. As an Abelian group the symmetry species, Γ , of the rotations, τ_i, must be satisfy the relation

$$\Gamma(\tau_1)\Gamma(\tau_2) = \Gamma(\tau_1 + \tau_2) \tag{2.47}$$

This relation is only satisfied by an exponential term which takes the following form

$$\Gamma^m(\pm\tau) = e^{im\tau}, \quad m = 0, \pm 1, \pm 2, \ldots \tag{2.48}$$

This exponential relation requires that, for any value of m, a 2π rotation about the fixed axis acts as the identity operator E. Thus, for an arbitrary wavefunction defined by the coordinates (r, φ, τ) it can be written

$$\varphi_m(r, \varphi, \tau - \tau_0) = P_{\tau_0}\varphi_m(r, \varphi, \tau) = \Gamma^m(\varphi_0)\varphi_m(r, \varphi, \tau) = e^{(-im\tau_0)}\varphi_m(r, \varphi, \tau) \tag{2.49}$$

Where P_{τ_0} is the projection operator pertaining to a rotation about the fixed axis by angle τ_0.

So, we see that any eigenfunction for a Hamiltonian defined by a symmetry group of all possible rotations about a fixed axis must be given by [37]

$$\varphi_m(r, \varphi, \tau) = f(r, \varphi)\, e^{im\tau} \tag{2.50}$$

Where $f(r, \varphi)$ is the portion of the wavefunction dependent only on (r, φ). As previously stated in Section 1.3, it has been determined that internal rotations between the monomers in the CO_2-H_2O/D_2O/HDO complexes are possible which leads to energy level splitting of rovibrational states. From the basis set for these rotations, defined above as $e^{im\tau}$, we can readily determine the symmetry of these tunnelling states and the associated possible transition types between them. The CO_2-H_2O/D_2O/HDO complexes are planar in orientation with the molecule lying along the spatial *z*-axis (inertial *a*-axis); this axis corresponds to the van der Waals bond between monomers and is

where the internal rotation occurs. A parameter, τ, is defined as the angle of internal rotation about this axis, as shown in Figure 2.2 below

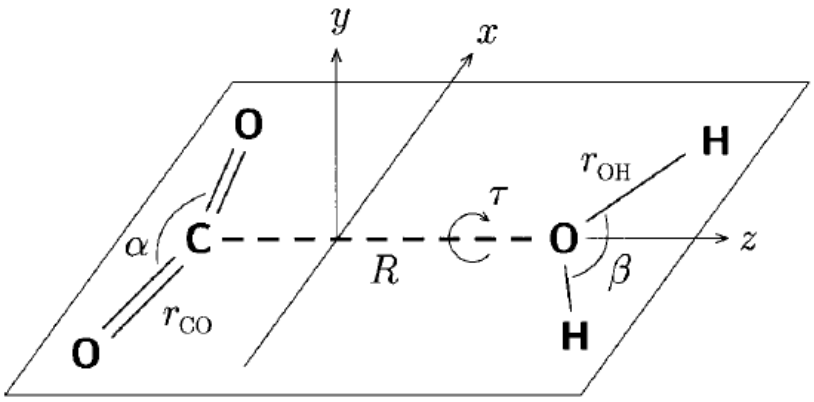

Figure 2.2: Equilibrium configuration and intermolecular Jacobi coordinates (α, β, τ) of CO_2-H_2O [23]

The symmetry states due to tunneling motions around this axis are determined by how this rotation angle, τ, transforms with the operations of the symmetry group of the molecule, that is, under the permutations and inversions of identical nuclei in the G_4 (for CO_2-HDO)/G_8 (for CO_2-H_2O/D_2O) groups. These transformations are listed in the following tables. Note that as the integer value, m, can take on positive and negative value, the transformation properties of the basis function are evaluated for both signs.

Table 2.16: Calculation of tunnelling basis states due to internal rotation of the monomers in the CO_2-H_2O/D_2O complexes

G_8	E	(12)(34)	E*	(12)(34)*	(12)	(34)	(12)*	(34)*
τ	τ	τ	-τ	-τ	π+τ	π+τ	π-τ	π-τ
$e^{+i\|m\|\tau}$	$e^{+i\|m\|\tau}$	$e^{+i\|m\|\tau}$	$e^{-i\|m\|\tau}$	$e^{-i\|m\|\tau}$	$(-1)^{\|m\|}e^{+i\|m\|\tau}$	$(-1)^{\|m\|}e^{+i\|m\|\tau}$	$(-1)^{\|m\|}e^{-i\|m\|\tau}$	$(-1)^{\|m\|}e^{-i\|m\|\tau}$
$e^{-i\|m\|\tau}$	$e^{-i\|m\|\tau}$	$e^{-i\|m\|\tau}$	$e^{+i\|m\|\tau}$	$e^{+i\|m\|\tau}$	$(-1)^{\|m\|}e^{-i\|m\|\tau}$	$(-1)^{\|m\|}e^{-i\|m\|\tau}$	$(-1)^{\|m\|}e^{+i\|m\|\tau}$	$(-1)^{\|m\|}e^{+i\|m\|\tau}$
sum	1	1	1	1	$(-1)^{\|m\|}$	$(-1)^{\|m\|}$	$(-1)^{\|m\|}$	$(-1)^{\|m\|}$
difference	1	1	-1	-1	$(-1)^{\|m\|}$	$(-1)^{\|m\|}$	$(-1)^{\|m+1\|}$	$(-1)^{\|m+1\|}$

Table 2.17: Calculation of tunnelling basis states due to internal rotation of the monomers in the CO_2-HDO complex

G_4	E	(12)	E*	(12)*
τ	τ	π+τ	-τ	π-τ
$e^{+i\|m\|\tau}$	$e^{+i\|m\|\tau}$	$(-1)^{\|m\|}e^{+i\|m\|\tau}$	$e^{-i\|m\|\tau}$	$(-1)^{\|m\|}e^{-i\|m\|\tau}$
$e^{-\|m\|\tau}$	$e^{-i\|m\|\tau}$	$(-1)^{\|m\|}e^{-i\|m\|\tau}$	$e^{+i\|m\|\tau}$	$(-1)^{\|m\|}e^{+i\|m\|\tau}$
sum	1	$(-1)^{\|m\|}$	1	$(-1)^{\|m\|}$
difference	1	$(-1)^{\|m\|}$	-1	$(-1)^{\|m+1\|}$

When m=0 we see that all characters for the basis set are +1 under the operations of the G_4 and G_8 groups and as such the symmetry of the m=0 state must be A_1 and A_1' respectively. This corresponds to the lowest energy tunnelling state of the molecule. For higher order integer values, we must take the linear combination of the basis states with differing sign (this is the "sum" and "difference" entries in Tables 2.16 and 2.17 above) to determine the symmetry of the tunnelling states. As can be seen from the table above, for the $m=\pm1$ and $m=\pm2$ sets, the symmetry of the tunnelling states for the CO_2-H_2O/D_2O and CO_2-HDO complexes in terms of their corresponding irreducible representations in the symmetry groups are defined as follows (note that the in-phase linear combination of wavefunctions is symmetric while the out-of-phase combination is antisymmetric and thus the former is of lower energy):

Table 2.18: Symmetries of the tunnelling states due to internal rotation of the monomers in CO_2-H_2O/D_2O/HDO

CO_2-HDO	Tunneling State	CO_2-H_2O/D_2O	Tunneling State
Γ|m=0>	A_1	Γ|m=0>	A_1'
Γ[|m=1>+|m=-1>]	B_2	Γ[|m=1>+|m=-1>]	A_1''
Γ[|m=1>-|m=-1>]	B_1	Γ[|m=1>-|m=-1>]	A_2''
Γ[|m=2>+|m=-2>]	A_1	Γ[|m=2>+|m=-2>]	A_1'
Γ[|m=2>-|m=-2>]	A_2	Γ[|m=2>-|m=-2>]	A_2'

2.5.7 Nuclear Spin Statistical Weights

Certain features in molecular spectra such as specific intensity patterns and alterations can be attributed to the statistical weights of rovibronic states due to nuclear spin. The Pauli exclusion principle places an additional constraint on the symmetry requirements of the total internal wavefunction of the molecule; identical nuclei, being indistinguishable, can at most, in their exchange, change the sign of the total wavefunction. The total internal wavefunction of the molecule in a totally symmetric ground electronic state is given as the product of the rovibrational wavefunction (ψ_{rve}) and the nuclear spin wavefunction ψ_{ns} [29]

$$\psi_{int} = \psi_{rve}\psi_{ns} \tag{2.51}$$

The Pauli exclusion principle states that the total internal wavefunction must be invariant under even/odd exchange of bosons and under even exchange of fermions. Odd exchange of fermions results in a sign change to the wavefunction. To form a basis set for the total internal wavefunction the product of the symmetry species of the rovibronic state Γ_{rve} and of the nuclear spin state Γ_{ns} must include the symmetry species of the total internal wavefunction.

The statistical weight character representation of the symmetry species of Γ_{rve} can be determined via the following formula [29]:

$$\chi_{rve}^{sw}[P] = 2\prod(2I_a + 1)(-1)^{2I_a(n_a-1)} \tag{2.52}$$

$$\chi_{rve}^{sw}[P^*] = 0 \tag{2.53}$$

Where $\chi_{rve}^{sw}[P]$ and $\chi_{rve}^{sw}[P^*]$ are the characters under permutation P and inversion P^* operations of the corresponding symmetry group respectively and n_a is the set of nuclei having their nuclear

spin I_a operated on. Applying equations 2.52 - 2.53 to the four operations of the G_4 symmetry group (E, (12), E*, (12) *) yields the following statistical weight calculation for CO_2-Kr:

$$\chi_{rve}^{sw}[E] = 2[(2(0)+1)(-1)^0(2(0)+1)(-1)^0(2(0)+1)(-1)^0(2(0)+1)(-1)^0] = 2 \quad (2.54)$$

$$\chi_{rve}^{sw}[(12)] = 2[(2(0)+1)(-1)^0(2(0)+1)(-1)^0(2(0)+1)(-1)^0(2(0)+1)(-1)^0] = 2 \quad (2.55)$$

$$\chi_{rve}^{sw}[E^*] = 0 \quad (2.56)$$

$$\chi_{rve}^{sw}[(12)^*] = 0 \quad (2.57)$$

with $I_{carbon} = 0$, $I_{krypton} = 0$ and $I_{oxygen} = 0$

And the following reducible representation:

Table 2.19: Reducible character representation for statistical weights of CO_2-Kr

SW	E	(12)	E*	(12)*
Γ_{sw}	2	2	0	0

Applying the reduction equation 2.23 to Table 2.19 yields the following irreducible representation for the statistical weights of CO_2-Kr:

$$\Gamma_{sw} = A_1 + A_2 \quad (2.58)$$

From the statistical weight calculation, we can arrive at the following symmetry species determination for the nuclear spin function of the molecule:

Table 2.20: Statistical weights of symmetry species for the CO_2-Kr molecule

Γ_{sw} [CO_2-Kr]	Statistical Weight
A_1	1
A_2	1
B_1	0
B_2	0

Here we notice that only two of the symmetry species are present with a 1:1 weight whereas the states with species B_1 and B_2 are not allowed.

By the same methodology one can calculate the nuclear spin statistical weights for the CO_2-H_2O/D_2O/HDO complexes and obtain the following

Table 2.21: Statistical weights of symmetry species for the CO_2-H_2O/D_2O/HDO complexes

Γ_{sw} [CO_2-H_2O]	Statistical Weight
A_1'	3
A_2'	0
B_1'	0
B_2'	0
A_1''	0
A_2''	0
B_1''	0
B_2''	1

Γ_{sw} [CO_2-D_2O]	Statistical Weight
A_1'	6
A_2'	0
B_1'	0
B_2'	0
A_1''	0
A_2''	0
B_1''	0
B_2''	3

Γ_{sw} [CO_2-HDO]	Statistical Weight
A_1	1
A_2	0
B_1	0
B_2	0

2.5.8 Rovibronic Selection Rules

Knowing the symmetry species of the vibrational, rotational, tunneling and spin states of a molecule allows for the identification of states that can be connected by an electric dipole transition in the presence of electromagnetic radiation. For asymmetric top molecules three types of transitions are possible, *a*-, *b*-, and *c*-type (or hybrid combinations of these types) which are defined as [29]:

Table 2.22: Transition type criteria for asymmetric tops

Transition	ΔK_a	ΔK_c
a-type	0	±1
b-type	±1	±1
c-type	±1	0

A vibrationally allowed transition must satisfy the following equation:

$$\Gamma_{init}^{vib} \otimes \Gamma_{\mu\alpha} \otimes \Gamma_{final}^{vib} \supset \Gamma(T_\alpha) \tag{2.59}$$

Where Γ_{init}^{vib} and Γ_{final}^{vib} are the ground and final vibrational symmetry species of the molecule, $\Gamma_{\mu\alpha}$ is the symmetry species of the dipole moment of the molecule along axis α = a, b, or c, and $\Gamma(T_\alpha)$ is the symmetry species of the translational coordinate pertaining to the α axis. The ground vibrational state must transform as the totally symmetric representation of the symmetry group (the irreducible representation with character of +1 under all group operations), so for G_4 this means $\Gamma(T_\alpha) = A_1$ and for G_8 $\Gamma(T_\alpha) = A_1{}'$

A rovibronically allowed transition must satisfy the following equation [29]:

$$\Gamma_{init}^{rve} \otimes \Gamma_{final}^{rve} \otimes \Gamma^* \supset A_1 \text{ or } A_1' \tag{2.60}$$

which implies,

$$\Gamma_{init}^{rve} \otimes \Gamma_{final}^{rve} \supset \Gamma^* \tag{2.61}$$

Where $\Gamma^{rve} = \Gamma_{tun} \otimes \Gamma_{vib} \otimes \Gamma_{rot} \otimes \Gamma_{spin}$ is the total internal wavefunction and $\Gamma^* = A_2 \text{ or } A_2{}'$ for G_4 and G_8 respectively (the irreducible representation in the symmetry group that holds a +1 character under all permutations and -1 under all inversions).

In this section the rules for the rovibronic transition from the ground vibrational state to CO_2 v_3 asymmetric stretch for the CO_2-H_2O complex will be explicitly derived. Calculations for the transitions connecting additional states (as studied in this thesis) in the CO_2-H_2O/D_2O/HDO complexes as well as CO_2-Kr can be found in Appendix D.

First the symmetry of the total internal wavefunction must be calculated for both the ground and excited states of the possible transition, which is simply a product of the symmetries of the previously calculated tunnelling, vibrational, rotational and spin states of the molecule. The total internal wavefunction for CO_2-H_2O must belong to the representations B_1'' or B_2'' in the G_8 group as, by the Pauli exclusion principle, these are the representations that are invariant under exchange of equivalent oxygen atoms in the molecules (bosons) and change sign under the exchange of the equivalent hydrogen atoms (fermions). Calculation of the total internal wavefunction for the ground vibrational state A_1' is thus

Table 2.23: Calculated symmetries of the total internal wavefunction of the ground vibrational state of CO_2-H_2O

$\Gamma_{rot} \otimes \Gamma_{spin} \otimes \Gamma_{tun} \otimes \Gamma_{vib}$						$\Gamma_{tot} = B_1''$ or B_2''
A_1' (ee) A_2' (eo) B_1'(oo) B_2' (oe)	$\otimes$	A_1' (3) B_2'' (1)	$\otimes$	A_1' A_1''	$\otimes$	A_1'	$1B_2''$ (ee, A_1') $1B_1''$ (eo, A_1') $3B_1''$ (oo, A_1'') $3B_2''$ (oe, A_1'')

The total internal wavefunction for the excited vibrational state representative of the CO_2 asymmetric stretch B_2' is

Table 2.24: Calculated symmetries of the total internal wavefunction for the CO_2 asymmetric stretching vibrational state of CO_2-H_2O

$\Gamma_{rot} \otimes \Gamma_{spin} \otimes \Gamma_{tun} \otimes \Gamma_{vib}$						$\Gamma_{tot} = B_1''$ or B_2''
A_1' (ee) A_2' (eo) B_1'(oo) B_2' (oe)	$\otimes$	A_1' (3) B_2'' (1)	$\otimes$	A_1' A_1''	$\otimes$	B_2'	$3B_2''$ (ee, A_1'') $3B_1''$ (eo, A_1'') $1B_1''$ (oo, A_1') $1B_2''$ (oe, A_1')

Using Equation 2.61 we can use the total internal wavefunctions of the initial and final states to determine the transition type for the excitation as follows

Table 2.25: Determination of the ground-to-CO_2 asymmetric stretching vibration transition for the CO_2-H_2O complex

Γ_{init}^{rve}	$\otimes$	Γ_{final}^{rve}	$\supset A_2'$
$1B_2''$ (ee, A_1'')		$3B_2''$ (ee, A_1'')	$1B_2''$ (ee, A_1') → $1B_1''$ (oo, A_1')
$1B_1''$ (eo, A_1'')		$3B_1''$ (eo, A_1'')	$1B_2''$ (eo, A_1') → $1B_2''$ (oe, A_1')
$3B_1''$ (oo, A_1')	$\otimes$	$3B_1''$ (oo, A_1')	$3B_1''$ (oo, A_1'') → $3B_2''$ (ee, A_1'')
$3B_2''$ (oe, A_1')		$3B_2''$ (oe, A_1')	$3B_2''$ (oe, A_1'') → $3B_1''$ (eo, A_1'')

From Table 2.25 we see that the transition from the ground vibrational state to the CO_2 asymmetric stretching state is represented by a *b*-type transition *(Δk_a=±1, Δk_c=±1).* This transition connects the (ee) and (eo) states in the lower tunnelling state (A_1') of the ground vibrational state to the (oo) and (oe) states in the lower tunnelling state of the CO_2 asymmetric stretch as well as the (oo) and (oe) states in the upper tunnelling state (A_1'') of the ground vibrational state to the (ee) and (eo) states in the upper tunnelling state of the CO_2 asymmetric stretch. These transitions are depicted in Figure 2.3 below

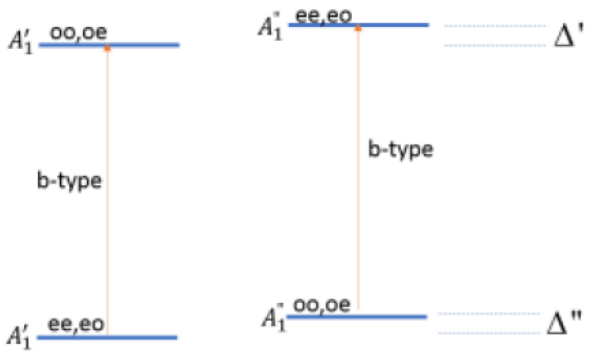

Figure 2.3: Tunneling diagram for the CO_2 ν_3 transition of CO_2-H_2O. Δ' and Δ'' indicate the tunneling splitting's for the ground and excited states

From Figure 2.3 we can see that the difference in band origins for the two *b*-type transitions leads to a determination of the difference in tunnelling splittings between the upper and lower vibrational states ($\Delta' - \Delta''$). This is a direct result of the symmetry of the total internal wavefunction for the CO_2 ν_3 vibration. The same conclusion is drawn for the CO_2-D_2O complex in this region as it possesses the same symmetry (see Appendix D). In the case of the CO_2-D_2O complex in the D_2O ν_3 region, the symmetry of the total internal wavefunction allows for the determination of the sum of tunnelling splittings of the lower and upper vibrational states ($\Delta' + \Delta''$). For CO_2-HDO in the O-D stretch region the symmetry of the wavefunction allows for independent determination of tunnelling splittings for the lower and upper vibrational states (see Appendix D). Tunelling splittings will be discussed in detail in Section 4.

3. Methods

3.1 Supersonic Jet Expansion

The supersonic jet expansion method was chosen to create the clusters of interest for spectroscopic inspection in this thesis. This method of molecular complexation was initially developed by Kantrowitz *et al.* [38] in the 1950's to cool a bulk gas to low temperatures while avoiding possible condensation pathways. A supersonic jet allows a high-pressure gas to be expanded into a low-pressure region via a small nozzle. As the gas mixture is expanded into the low-pressure region through the nozzle molecules collide frequently with each other effectively narrowing the velocity distribution of the bulk gas. Figure 3.1 below shows a schematic diagram of a typical jet expansion.

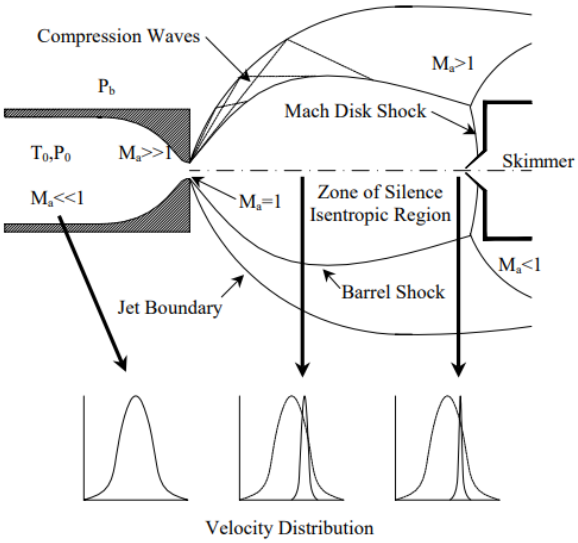

Figure 3.1: Schematic of supersonic jet expansion and resulting velocity distribution [39]

The collisions at the nozzle result in the cooling of internal degrees of freedom of the gas involved in the expansion. In the "zone of silence" the number of collisions drops, allowing weak van der Waals forces to dominate thermal forces and allow molecular clusters which are formed to

stabilize. Here is where the velocity distribution narrows, and the bulk exceeds the local supersonic speed (hence the name). This is also the region of inspection by optical methods to obtain the infrared spectra of the created clusters.

The supersonic jet expansion is approached as an adiabatic process as the molecular complexation occurs on such a fast timescale that heat transfer outside of the jet is assumed to be zero. The dynamics of the jet expansion can be explored using conservation of energy of the bulk gas before and after the expansion. The total energy of the bulk is comprised of its internal energy (U), which is the sum of translational (U_{trans}), rotational (U_{rot}) and vibrational energy (U_{vib}), as well as its potential energy (which for an ideal gas is approximated as PV where P and V are the pressure and volume of the gas) and its kinetic energy, $1/2mv^2$, where m is the mass and v is the average velocity of the bulk. Then, by the conservation of energy we can write (where the subscript zero signifies initial conditions prior to expansion) [40]:

$$U_0 + P_0V_0 + \frac{1}{2}m{v_0}^2 = U + PV + \frac{1}{2}mv^2 \tag{3.1}$$

Prior to commencement of the expansion (pulsed nozzles closed) one can expect that bulk travel through the slit is small and that the velocity distribution of the bulk is Maxwellian with zero mean. As a result, the initial kinetic energy of the bulk can be approximated as zero. As well, after expansion, since the pressure in the low-pressure chamber is brought to (near) vacuum, *P* is also approximated as 0. This simplifies the conservation of energy equation to:

$$U_0 + P_0V_0 = U + \frac{1}{2}mv^2 \tag{3.2}$$

From here, if most of the initial energy of the bulk is transferred into kinetic energy, we can assume that the total internal energy of the bulk after expansion is very small (eg. *U* is decreased). This condition is known as a “cold” molecular beam and is proportional to the square of the resulting

bulk velocity after expansion. As the bulk reaches higher velocities after expansion more energy is transferred from the internal degrees of freedom of the gas (rotational, and vibrational) into the linear motion of the bulk (translation). This effectively "cools" the rotational and vibrational energies of the molecules in the gas to their lowest possible energy states.

Before the expansion the high-pressure gas is in thermodynamical equilibrium, that is, its internal temperature (T_0) is the same for all degrees of freedom:

$$T_0 = T_{rotation} = T_{translation} = T_{vibration} \tag{3.3}$$

After the expansion, however, there is no equilibrium between degrees of freedom of the gas owing to their difference in collisional cross section. The translational cross section is the largest and is proportional to the width of the velocity distribution. Thus, most of the translational energy is transferred to kinetic energy of the bulk during the expansion, and the translational degrees of freedom are cooled rapidly. Rotational and vibrational collision cross sections are much smaller, and as such not all of this energy can be transferred to kinetic energy. This is because spacing between vibrational energy levels (100-4000 cm^{-1}) is much larger than for rotational energy levels (0.05-20 cm^{-1}), while the translational energy levels essentially form a continuum [40]. So, after expansion:

$$T_{translation} < T_{rotation} < T_{vibration} \tag{3.4}$$

As a result of this process the population of molecular levels are concentrated in the lowest rotational states in the ground vibrational states. To further cool the internal degrees of freedom of the bulk a buffer or carrier gas is used alongside the molecules of interest to increase the rate of collisions during the expansion. By including a carrier gas, which is frequently an inert rare gas like Helium with no internal degrees of freedom, the expansion bulk can transfer even more of its

internal energy into translational energy of the carrier gas further narrowing its velocity distribution after expansion. In the "zone of silence", once collisions have dropped off, this method of cluster formation can achieve rotational temperatures down to 2-3K and vibrational temperatures near 100K.

Using the supersonic jet expansion to cool the internal degrees of freedom of the gas molecules under investigation greatly reduces spectral congestion which simplifies the resulting rotation-vibration spectrum (eg. reduction in number of absorption lines as populated energy states are minimized). Furthermore, in the laboratory when the gas is pulsed through the slit it is probed perpendicular to the bulk flow to minimize Doppler broadening of the resulting absorption lines. This methodology is used as the bulk has only a small velocity component perpendicular to the jet flow so probing in this manner minimizes this phenomenon. Probing the stabilized clusters in the "zone of silence" also ensures that there is nearly no collisional broadening, and by analogue, no pressure broadening in the resulting absorption lines as well.

The cooling of internal degrees of freedom of the jet expansion is not perfect however and under suitable jet conditions it has been shown that ~2% of the clusters formed in the jet expansion, for triatomic molecules such as CO_2-Rg (and likely others), occupy the degenerate intramolecular bend of the CO_2 unit [13-15]. This implies that the vibrational cooling of the jet is not as efficient as rotational cooling, which is not surprising given the difference in the size of the collision cross sections for these degrees of freedom (eg. vibrational energy levels are spaced at greater distances than rotational energy levels). This experimental outcome gives rise to conditions suitable to studying "hot bands" of these molecules, which are transitions originating from an excited vibrational state. Indeed, these types of bands have been well studied recently for the CO_2-Rg family of clusters from the doubly degenerate intramolecular bend of CO_2 to the degenerate bend

combined with the asymmetric stretch of the CO_2 unit. This transition is explored in this thesis for the CO_2-Kr complex.

3.2 Experimental Apparatus

The supersonic jet setup used in this experiment consists of a six-way cross vacuum chamber housing the slit nozzle arrangement atop a diffusion pump that is backed by a mechanical pump located away from the apparatus due to the noise and vibration present in its operation. Optical components including the mid-IR source are located on a vibration-isolation table attached to the cross inside of a custom-built polystyrene box which is used to encase the components in a nitrogen purge to reduce ambient CO_2 atmospheric absorptions (as the frequency of the radiation under study is near strong CO_2 fundamental absorptions). Figure 3.2 below shows a schematic of the entire experimental setup:

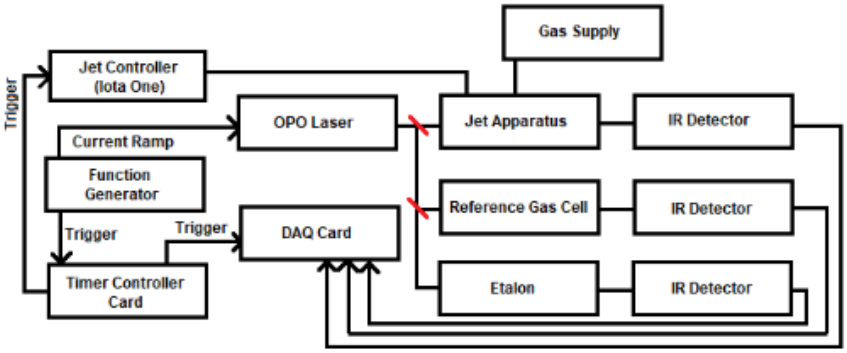

Figure 3.2: Schematic of the experimental setup

3.2.1 Supersonic Jet Chamber

Probing of the molecular clusters from the jet expansion is done inside of a six-way cross (ISO NW250) inside of which pressure is reduced to near vacuum by a water-cooled diffusion pump (Varian VHS-10, located directly beneath the cross) and a rotary pump (Edwards E2M275,

located in a mechanical room adjacent to the experiment to minimize ambient vibrations that could introduce mechanical noise into the optical signal). These pumps can effectively reduce the pressure in the cross chamber to as low as 10^{-7} Torr, going as high as 10^{-4} Torr during operation of the jet. The chamber setup is pictured below.

Figure 3.3: The jet chamber in the laboratory at the University of Calgary

3.2.2 Slit Nozzles

Injection of the high-pressure gas supply into the jet chamber is carried out by a set of Parker Hannifan Series 9 pulsed slit nozzles arranged in series. These nozzles are fed by a ¼ inch gas supply line which runs to a station where the gas mixture is measured and loaded. The high-pressure gas mixture fed to the nozzles is routinely run at backing pressures of 100-300 PSI, depending on the clusters under investigation. Pulsing of the nozzles is controlled by an Iota One Jet Controller which drives a solenoid in each nozzle that opens and closes each slit. Timing characteristics for opening of the slit are entered in a custom LabView environment and fed to the controller. The slit which the gas is expanded through is created by a pair of adjustable plates mounted to the bottom of a custom channel block on the nozzles that can be manually adjusted by

a set of positioning screws to help the expanding gas travel as a “sheet” in as linear a fashion as possible rather than fanning out past the optical beam path in the transverse direction. These plates can currently be adjusted to separations as small as 10 microns using special sheet metal shims. It is has been found experimentally that a smaller slit separation has some effect on the overall signal to noise of the experiment as it directly influences complex formation by means of routing the gas through a smaller area and increases the distribution of the expansion gas better into the path of the optical probe by reducing diffusiveness in the perpendicular direction of the expansion.

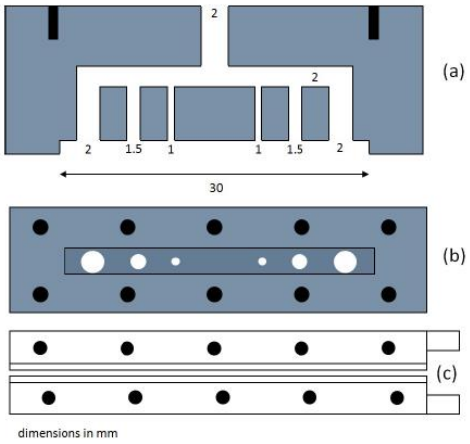

Figure 3.4: Schematic of a single pulsed nozzle used in the jet expansion. (a) the internal nozzle chambers, (b) bottom view of channel block, (c) bottom view of adjustable block plates

3.2.3 Multipass Cell

It is essential to increase the path length of the probe radiation with the clusters created in the jet expansion to increase the signal to noise of the spectra. Density of the clusters created in the expansion can vary depending on the mixture used, slit jet conditions, chamber and gas backing pressures, among other factors. Furthermore, depending on the clusters under investigation it is

likely that many transitions of interest will be weak and need to be probed over many averages to achieve high signal to noise. This can only be achieved when the incident radiation has enough interactions with the clusters. To address these considerations a multipass cell (New Focus 5612) is used inside of the jet chamber. This cell consists of two nickel-plated mirrors with 99.9%+ reflectivity placed ~70 cm apart. These mirrors are covered with glass tubes and mounted to heaters which are used to minimize oil deposition from the diffusion pump at the bottom of the chamber. When operated according to the manufacturer's specifications this cell can deliver over 180 reflections between the mirrors before the incident radiation exits the cell. By adjusting the incident angle of the beam these reflections can be confined to an area optimal to probe the descending jet expansion from the slit nozzles located directly above.

Figure 3.5: Graphical depiction of the multipass cell in the jet chamber

3.2.4 Mid-Infrared Radiation Source

The mid-infrared radiation source used in these experiments is an Aculight Argos 2400 Optical Parametric Oscillator (OPO) Module D capable of producing radiation in the wavelength range of 3.9-4.6 microns. A schematic of the entire optical system driving the OPO's radiation output is seen below

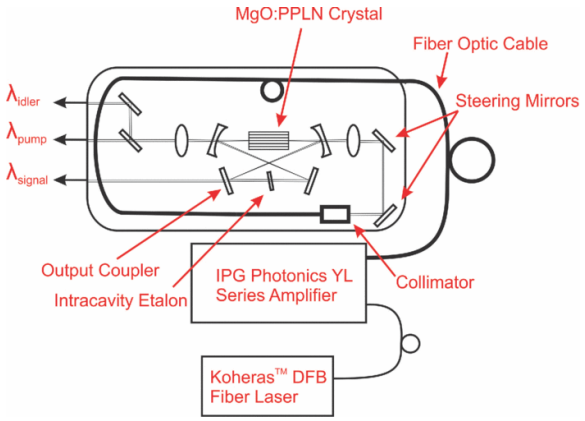

Figure 3.6: Optical components comprising the Aculight Argos OPO Module D [41]

The OPO module consists of three main components; a distributed feedback (DFB) fiber laser from Koheras which acts as a pump source providing radiation at 1064 nm and 14 mW; a fiber laser amplifier from IPG Photonics which amplifies the pump radiation up to 10 W; and the OPO module itself which is fed the amplified radiation by means of a fiber optic probe tipped with a collimator from the amplifier. The OPO module contains a magnesium-doped periodically poled lithium niobate (MgO:PPLN) crystal inside of a reflective cavity. Radiation is directed from the cable into the cavity by means of two adjustable mirrors which change the angle of incidence on the crystal (these mirrors allow for tuning of power output). The MgO:PPLN is a periodically structured non-linear crystal grating with a "fan-out" design. The incident light goes through parametric down conversion as it passes through the crystal resulting in two output photons for every input photon (called signal and idler). The law of conservation of energy determines the following relationship between the wavelength of the incident and resulting down-converted photons:

$$\frac{1}{\lambda_{Pump}} = \frac{1}{\lambda_{Idler}} + \frac{1}{\lambda_{Signal}} \tag{3.5}$$

Where λ is the wavelength of the corresponding photon.

The output from the OPO is radiation of a single wavelength dependent on the position of the down conversion crystal. To “sweep” the wavelength over a spectral range a Piezo driving element is introduced between the pump laser and the amplifier. This Piezo is fed a 100Hz sine wave from a function generator with a peak-to-peak voltage of ~2V. Driving the Piezo with the function generator puts a mechanical stress on the optical fiber carrying the pump radiation which oscillates the wavelength of the resulting radiation in the fiber. For a 100Hz sine wave this creates a spectral range or “mode” of radiation which is approximately 0.7 cm^{-1} in width.

Coarse wavelength tuning is accomplished by means of a set screw which is connected to the housing of the MgO:PPLN crystal. Turning the screw adjusts the physical position of the crystal changing the point of incidence of radiation with respect to its periodic “fan” design. This provides relatively coarse tuning of the wavelength. Smaller adjustments can be made by moving the intercavity etalon housed in the OPO casing and tuning the Piezo driving element between the pump laser and the amplifier.

The resultant radiation from the OPO is output in the three beam elements from Equation 3.5. The OPO system does not have a digital readout to determine accurately the wavelength of the radiation so another method must be used. Idler radiation, which is the output channel used for spectroscopic purposes in the experiment, is divided among three paths; the first directed into the jet to probe the clusters, the second and third to an etalon and reference gas cell respectively, which are later used for frequency calibration. Spacing between etalon fringes coupled with CO_2 (or other reference gas) monomer absorption data from HITRAN allow for determination of the wavelength of the OPO radiation. The reference gas used in this experiment was CO_2 as it has well studied transitions that can be identified in the final data set. Finally, the radiation from the signal port is

passed through a photocell whose electrical signal is used to subtract the laser noise and power fluctuations from the trace of the jet probe.

3.2.5 Data Collection

The three split idler beams are ultimately collected with either LN_2 cooled indium-antimonide (InSb) or LN_2 cooled mercury-cadmium-telluride (HgCdTe or MCT) detectors. InSb detectors generate a current over a p (positive)-n (negative) junction when incident photons of sufficient energy strike the detector. MCT detectors contain semiconductor electrons which absorb infrared radiation which causes them to excite from a valence band to a conduction band producing a current. Current from the detectors is digitized on a 12-bit DAQ card in bin numbers at a rate of 4MHz as the output of the experiment.

From a data collection point of view timing of several elements must be considered to 1) probe the jet expansion at the optimal point of cluster formation and 2) minimize noise in the resulting signal due to background factors. As such a system of counters is implemented to ensure precise pulsing of the slit nozzles alongside digitization of the infrared radiation signal. Triggered off the 100Hz sine wave which is sent to the Piezo driver to sweep the radiation wavelength the counter system is initiated which ensures that the slit jet is pulsed for a short period (<2ms) before detector signals are digitized at the DAQ card. Theoretically this allows for the inspection of the molecular clusters at a point when they have reached peak formation. Data acquisition is carried out over a period of 2ms near the zero crossing of the sine wave. Timing of this acquisition reduces high frequency noise from vibrations due to the Piezo mechanical oscillations as the slope of the voltage function driving the Piezo strain is at its largest value (rather than sampling the sine wave around its peaks where the slope is small and therefore likely to produce a noisy signal). Below is a graphical representation of the timing sequence used for data acquisition

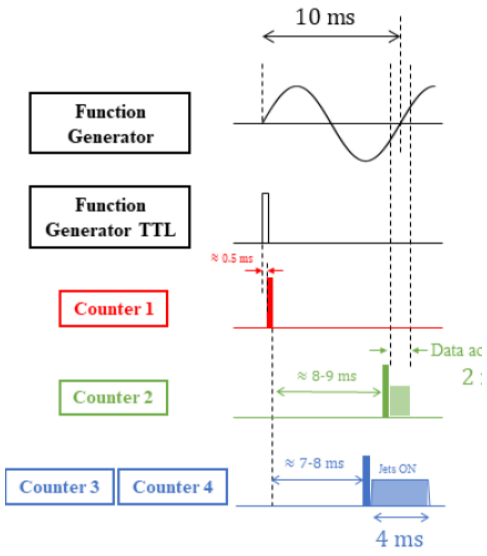

Figure 3.7: Data collection architecture used in the pulsed slit jet supersonic expansion [42]

This timing sequence is carried out over many scans (sometimes hundreds) which are then averaged for the spectral range of the laser. This allows for the detection of weaker transitions by improving signal to noise. Furthermore, as the width of a single mode provided by the OPO is roughly 0.7cm^{-1}, the laser is frequently tuned up/down in frequency to record the entire spectrum for a given rovibrational band (which can extend past a few cm^{-1} in width). A custom LabVIEW program is used to manage the various aspects of timing/delay for the data acquisition process. These delays can be adjusted manually to best suit the nature of the clusters under investigation (eg. to adjust for changes in complexation times). LabVIEW also has custom programmed background subtraction templates which consider the noise and power fluctuations as a result of the rapid scan of the signal beam (as it is correlated by down conversion to the idler) as well as several processes to deal with "jitter" in the optical setup (which consider the position of etalon fringes on a scan-by-scan basis). By subtracting these elements (as collected by a photodetector on the signal beam output) we can improve the overall signal to noise of the experiment as much

as possible. As previously mentioned, this program records data in terms of bin numbers rather than frequencies, so a custom program using GRAMS software as a platform is then used for frequency interpolation using the etalon absolute calibration employing the reference gas scans. This is shown in Figure 3.3 below:

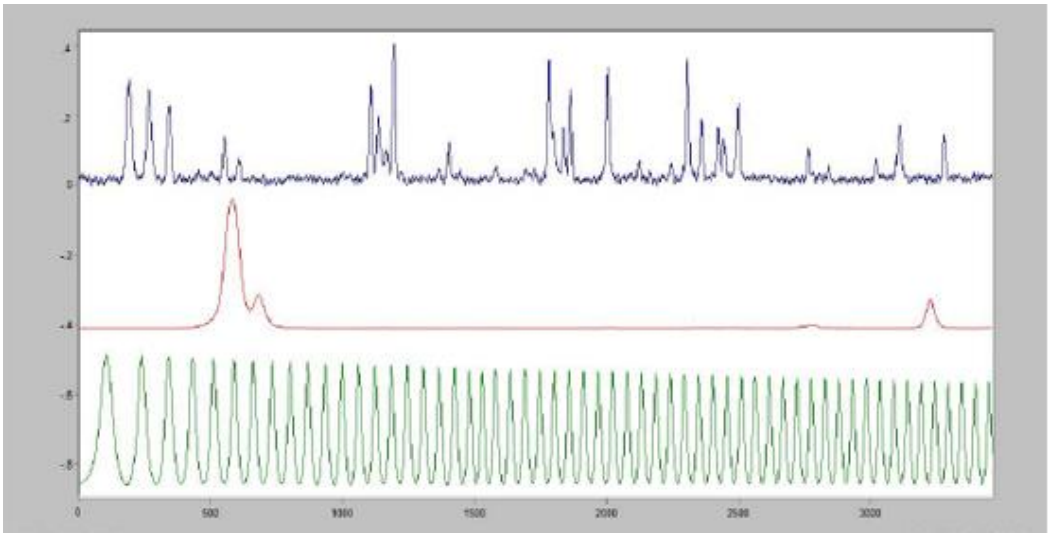

Figure 3.8: Collected data traces from GRAMS software (Top to bottom: Jet, reference gas, etalon)

Lastly, the data output from GRAMS is used in the final analysis of the spectrum which is carried out using the PGOPHER software program [43]. The PGOPHER software package is used to simulate the rovibrational spectra of molecules and uses several inputs (rotational constants, symmetry, interaction parameters) which solve for the energy eigenvalues of the rotational/vibrational Hamiltonian of a molecule and allows for the simulation and assignment of optical transitions based on these values. A screenshot of the PGOPHER program being used to simulate the spectrum of CO_2-H_2O is shown below:

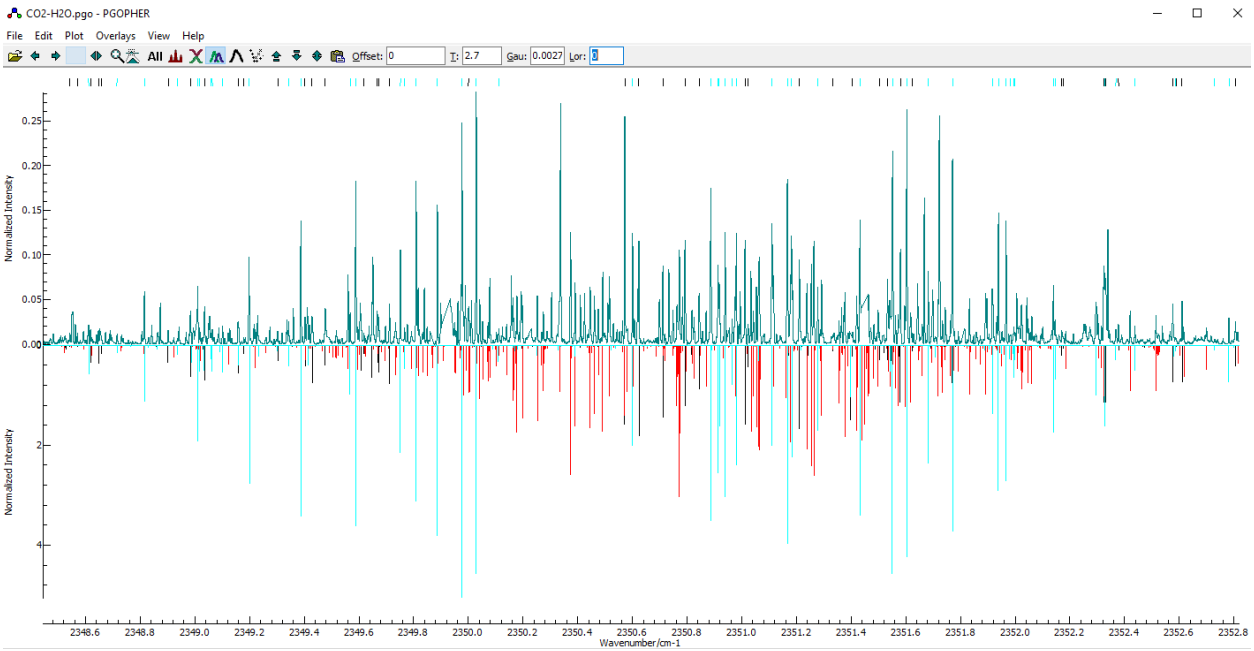

Figure 3.9: Observed (dark blue) and simulated (inverted black/light blue/red) spectrum of CO_2-H_2O in PGOPHER

4. Results

4.1 Spectra of CO_2-Kr in the 4.3um region: Intermolecular Bend and Symmetry Breaking of the Intramolecular CO_2 Bend

Presented here is the high-resolution infrared spectra of CO_2-Kr with consideration for a parametrized dependency on the isotopic mass of the Kr atom. This dependency scales the rotational constants and associated band origins of the complex by a methodology previously implemented for CO_2-Xe [15]. Presented is an analysis of the CO_2 ν_3 fundamental band, the infrared combination band involving the intermolecular bend, and the CO_2 $(01^11)\leftarrow(01^10)$ (labelled $(\nu_1, \nu_2, \nu_3) \leftarrow (\nu_1, \nu_2, \nu_3)$) hot band. Clusters were created in a supersonic jet expansion as detailed in Section 3.1. A gas mixture of 5 Torr CO_2/200 Torr Kr in a Helium buffer gas (450 PSI) was used in the expansion. Backing pressure for the experiment was set to 200 PSI. A rotational temperature of 2 K was assumed in the fit of the CO_2-Kr bands listed below.

4.1.1 Parametrization of Kr Isotopic Effects

Krypton has five main isotopes with ^{84}Kr possessing the highest natural abundance by a large degree; these five isotopes represent 99.7% of the natural abundance of the Kr element. Replacing ^{84}Kr with any of the other isotopes can have a direct effect on the rotational and vibrational transitions of the CO_2-Kr molecule as the associated change in mass of the Kr atom directly effects its moment of inertia through a change in the reduced mass of the complex. This change in moment of inertia about one (or more) of the inertial axes of the complex will in turn change its rotational constants and thus its energy levels. This will appear as splitting or broadening in the resulting infrared spectrum of the complex. Such phenomena have previously been studied

by our group at the University of Calgary for the CO_2-Xe [15] complex for which a parametrization of the rotational constants and band origins was devised. This parametrization is reproduced here.

As an entry point to modelling the effects of the change in isotopic mass of the Kr atom in the CO_2-Kr complex a parametrization of the rotational constants was developed that allowed for changes in the mass. This parametrization of the B and C rotational constants is as follows:

$$B(N) = B(N_0) * \left[F_B(N) + B_{adj} * (N - N_0)\right] \tag{4.1}$$

$$C(N) = C(N_0) * \left[F_C(N) + C_{adj} * (N - N_0)\right] \tag{4.2}$$

Where N is the atomic mass number of the Krypton isotope, N_0 is the atomic mass number of the most abundant Kr isotope ^{84}Kr, F_B and F_C are rigid model scaling factors relative to ^{84}Kr (which are calculated as the ratio of the reduced masses of ^{84}Kr to the isotope under study), and B_{adj} and C_{adj} are empirical parameters which are slight corrections to the scaling factors necessary to accurately reproduce the microwave data from [18, 19]. The A rotational constant was determined to be free from the effects of isotopic shifts in the Kr atom as the Kr atom effectively sits on the a-inertial axis so a change in its mass will not affect its moment of inertia about this axis. Table 4.1 below lists the scaling factors for the five most abundant isotopes of CO_2-Kr.

Table 4.1: Krypton isotope atomic mass, abundance, and rigid model scaling factors

Atomic Mass Number	Atomic Mass	Abundance	F_B	F_C
80	79.916	0.023	1.017194	1.015408
82	81.913	0.116	1.008389	1.007524
83	82.914	0.115	1.004137	1.003712
84	83.912	0.57	1.000000	1.000000
86	85.911	0.173	0.991997	0.99281

Isotopic dependence of the shift in the band origin ν_0 is also parametrized as:

$$\nu_0(N) = \nu_0(N_0) + Offset * (N - N_0) \tag{4.3}$$

Here the term *Offset* is another empirical parameter that describes the band origin shift for a change of one in the Kr atomic mass number, thus this term has units of cm^{-1}/Dalton.

4.1.2 The CO_2 ν_3 fundamental band

The experimental spectrum for the asymmetric stretch of the CO_2 unit in CO_2-Kr is shown in Figure 4.1 below. This band exhibits b-type transitions (see Appendix D) ($\Delta k_a = \pm 1$) as the vibration occurs parallel to the inertial *b*-axis of the molecule. As such the isotopic dependence of the Kr atom in the molecule has little effect on splitting of the energy levels as it lies on the *a*-axis. As a result of this it was not possible to resolve any splittings in the spectrum for the ν_3 fundamental band (except at higher *J* values).

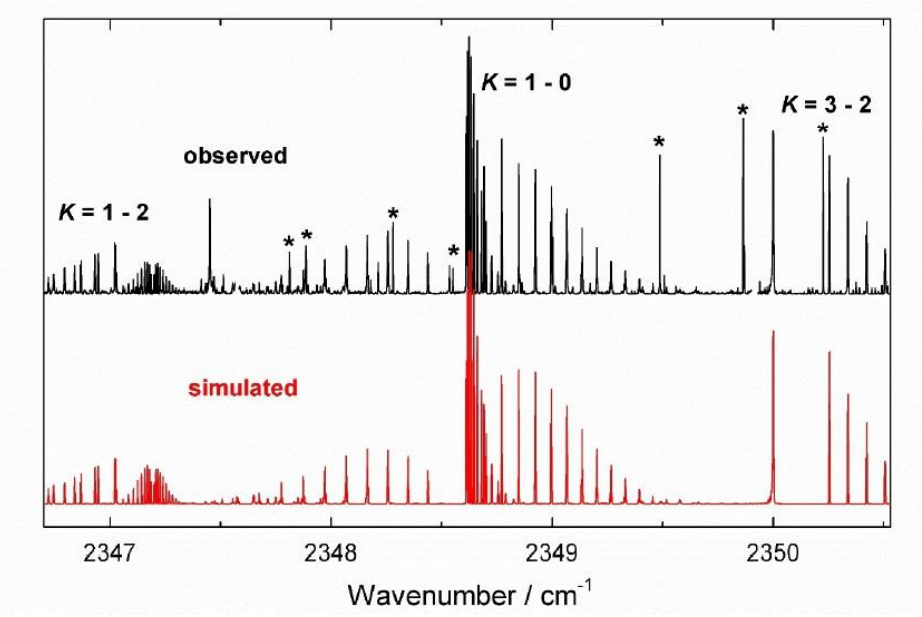

Figure 4.1: Observed and simulated spectra of CO_2-Kr in the CO_2 ν_3 fundamental region. Asterisks mark known transitions of the CO_2-He complex. The peak at 2347.45cm^{-1} is due to CO_2-Kr_2 [17].

Overall, 121 separate infrared transitions were assigned in the simulation with the majority of them being a blend of two or more isotopes of Kr. PGOPHER includes a feature called "*MergeBlends*" [43] which allows the user to weight overlapping lines to an intensity average of their components, in this case the various abundances of Kr isotopes. This feature was used to assign most of the lines in the spectrum. In addition to the infrared absorptions assigned in the above spectrum we included 18 microwave transitions from Fraser *et al.* (for ^{82}Kr, ^{84}Kr, ^{86}Kr) [18] and Iida *et al.* (^{84}Kr) [19] which were more heavily weighted (by a factor of 1000) to account for their higher precision. Ground and excited state rotational constants, scaling factors, and distortion parameters were varied to determine an optimal fit for the line positions, however, it was determined that the excited isotopic scaling factors and distortion parameters provided the best fit when constrained to match their ground state values. Fit parameters from the simulation are listed in table 4.2 below

Table 4.2: Molecular parameters for CO_2-Kr

	CO_2-Kr^{84}		
	Ground State		**Bend State**
ν_0		2348.2585(1)	2377.6875(1)
A	0.396347(17)	0.393209(18)	0.408780(40)
B	0.0446828(22)	0.0446832(22)	0.043155(19)
C	0.0399224(21)	0.0398858(25)	0.038304(16)
$10^6 \times \Delta_K$	-5.3(11)	[-5.3]	[0.0]
$10^6 \times \Delta_{JK}$	5.184(20)	5.84(33)	46.3(11)
$10^6 \times \Delta_J$	2.473(18)	[2.473]	2.57(46)
$10^6 \times \delta_k$	3.32(56)	[3.32]	
$10^6 \times \delta_J$	2.56(62)	[2.56]	
Offset		-0.000026(34)	-0.002187(28)
$10^5 \times B_{adj}$	3.2(18)		
$10^5 \times C_{adj}$	4.1(17)		

Units are in cm^{-1} except for B_{adj} and C_{adj} which are dimensionless. Quantities in parentheses are 1σ from the least squares fit, in units of the last quoted digit of the quantity itself. Quantities in square brackets were fixed at the indicated values.

While the values reported in Table 4.2 are for the ^{84}Kr isotope, this can be thought of as isotopic averages as the mass of the ^{84}Kr atom is very close to the average mass of the five most abundant isotopes. The 121 transitions fit in this spectrum produced an average rms (root mean square) deviation of 0.00022 cm^{-1} for the infrared transitions and 9 kHz for the microwave transitions. The infrared deviation is about an order of magnitude smaller than the experimental line width which indicates a satisfactory simulation of the spectrum. Furthermore, the rotational parameters listed in Table 4.2 agree well with those reported by Fraser *et al.* [18] and Randall *et al.* [10] but also include the 18 microwave transitions mentioned above, thus they should be considered more reliable given the accuracy of the microwave data.

The rigid model scaling factors B_{adj} and C_{ajd} were determined to be 3.2×10^{-5} cm^{-1} and 4.1×10^{-5} cm^{-1} respectively. This is slightly larger than those previously reported for the CO_2-Xe complex [15]. This result makes sense as Kr possesses smaller mass than Xe and the mass difference between isotopes is also larger for Kr. The empirical term *Offset*, signifying the isotopic band origin shift was determined to be -0.0002 cm^{-1}, with the negative sign implying a downward shift in wavenumber with increasing mass of the Kr isotope. This trend matches that reported for CO_2-Xe. Lastly, in comparison to the free CO_2 monomer, we see a band origin shift of 0.885 cm^{-1} downward for the CO_2-^{84}Kr complex. This value is in good agreement with the value of 0.884 cm^{-1} reported by Randall [10].

4.1.3 The Bend Combination Band

The spectrum of the bend combination band (intermolecular bend plus the CO_2 asymmetric stretch) for CO_2-Kr is shown in Figure 4.2 in terms of the splitting's resulting from the five most abundant Kr isotopes. As stated in Appendix D the band exhibits *a*-type transitions ($\Delta k_a = 0$) with noticeable splitting due to the mass of the Kr atom. As the bending vibration directly involves the

Kr atom in the complex any change in isotopic mass of this atom will affect the reduced mass of the molecule and thus its moment of inertia about the *a*-axis. This splitting is evident in Figure 4.2 in both the Q- and R-branches. Splitting's are less evident in the P-branch as, serendipitously, isotopic vibrational shifts seem to cancel.

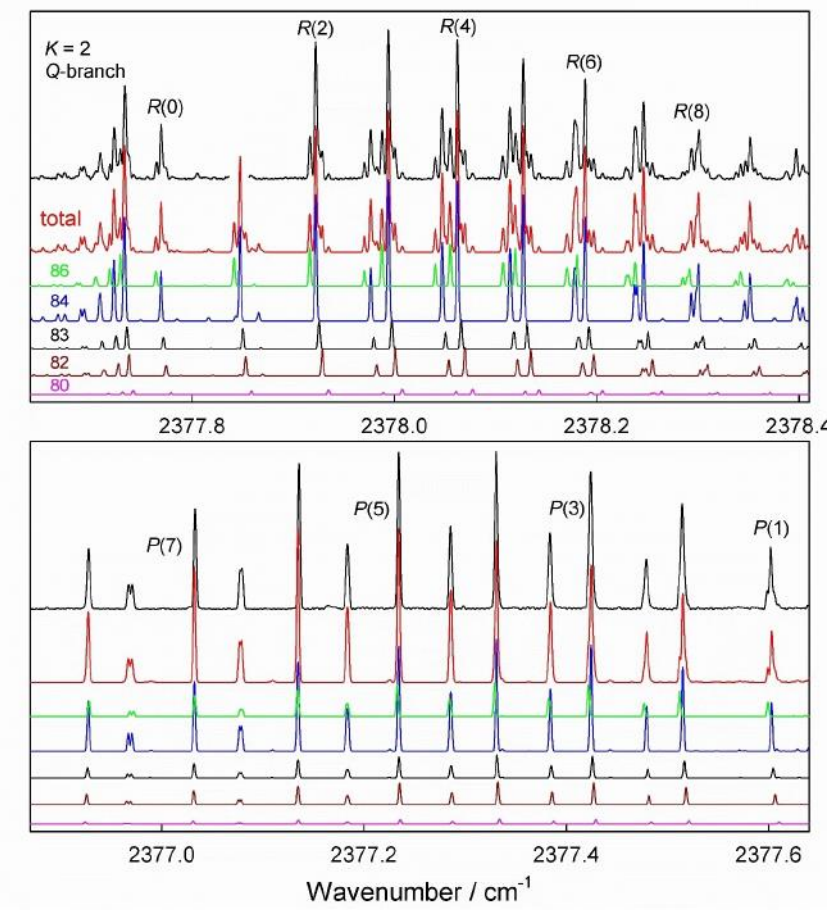

Figure 4.2: Observed (black) and simulated spectra of CO_2-Kr in the region of the intermolecular bend combination. Kr isotopes are broken out by their atomic number.

A total of 90 transitions were fit for the combination band yielding an average rms error of 0.00038 cm^{-1}. As can be seen from the figure above splitting could be partially or fully resolved for many of the assigned transitions. Splitting's that could not be resolved were again assigned

using the MergeBlends feature in PGOPHER as in the fundamental. To minimize the rms error of the fit ground state rotational parameters were constrained to those determined in the fundamental band. The rotational constants *B* and *C* as well as the band origin were scaled as per section 4.1.1. Excited state higher order distortion parameters were not constrained and were free to "float" in the fit as the excited state vibrational environment is close in energy to the intermolecular stretch of the complex which should influence these parameters (as opposed to the ground state which is located energetically far from this vibration).

The intermolecular bending frequency of the complex can be determined by subtracting the fundamental band origin from the combination band origin as the combination band is simply the simultaneous excitation of these two vibrational modes. Using the values in Table 4.2 we see this equates to a bend frequency of 29.429 cm^{-1}. This value is in good agreement with the calculated value reported by Chen *et al.* [45] (30.019 cm^{-1}) and with that calculated from an empirical forcefield estimate by Iida *et al.* [19] (31.6 cm^{-1}). Experimental characterization of the van der Waals stretch is possible via a Coriolis mixing between the bending frequency and the stretch. This was demonstrated previously for the CO_2-Xe complex as the stretch here was determined to be only 1.2 cm^{-1} above the bend frequency [15]. Incorporation of the Coriolis Hamiltonian element here did not yield meaningful improvement to the overall fit of the combination band so ultimately it was not included in the fit. This demonstrates that the separation of the van der Waals stretch and the intermolecular bend for CO_2-Kr should be larger than for CO_2-Xe. Indeed, the predicted separation for CO_2-Kr has been posited to be 2.287 cm^{-1} from an ab initio calculation from Chen *et al.* [45] and 2.8 cm^{-1} from an empirical force field calculation by Iida *et al.* [19].

4.1.4 The CO_2 (01^11) ← (01^10) hot band

As described in Section 3.1, under suitable jet conditions the expansion of the high-pressure gas mixture of CO_2-Kr can leave ~2% of the population of clusters in the excited degenerate intramolecular bend of the CO_2 unit. The presence of the Kr atom in the complex causes the doubly degenerate symmetry of this vibration to break and split into in-plane (ip) and out-of-plane (op) components. This excited vibrational state is then probed to a further excitation of bending plus the asymmetric stretch of the CO_2 unit. As determined in Appendix D, these are *b*-type transitions from a symmetry state of A_1 (ip) and B_1 (op) for the degenerate bend to states of B_2 (ip) and A_2 (op) for the bend plus the stretch. This hot band transition has previously been studied for several other Rg complexes in our laboratory [13-15]. Kr isotopic splittings were not evident in the experimental data and were ignored for the same reasons as posited in the description of the fundamental band (the hot band vibration is on the axis perpendicular to the Kr atom). Figure 4.3 below shows the hot band spectrum as the summation of the ip and op bend modes.

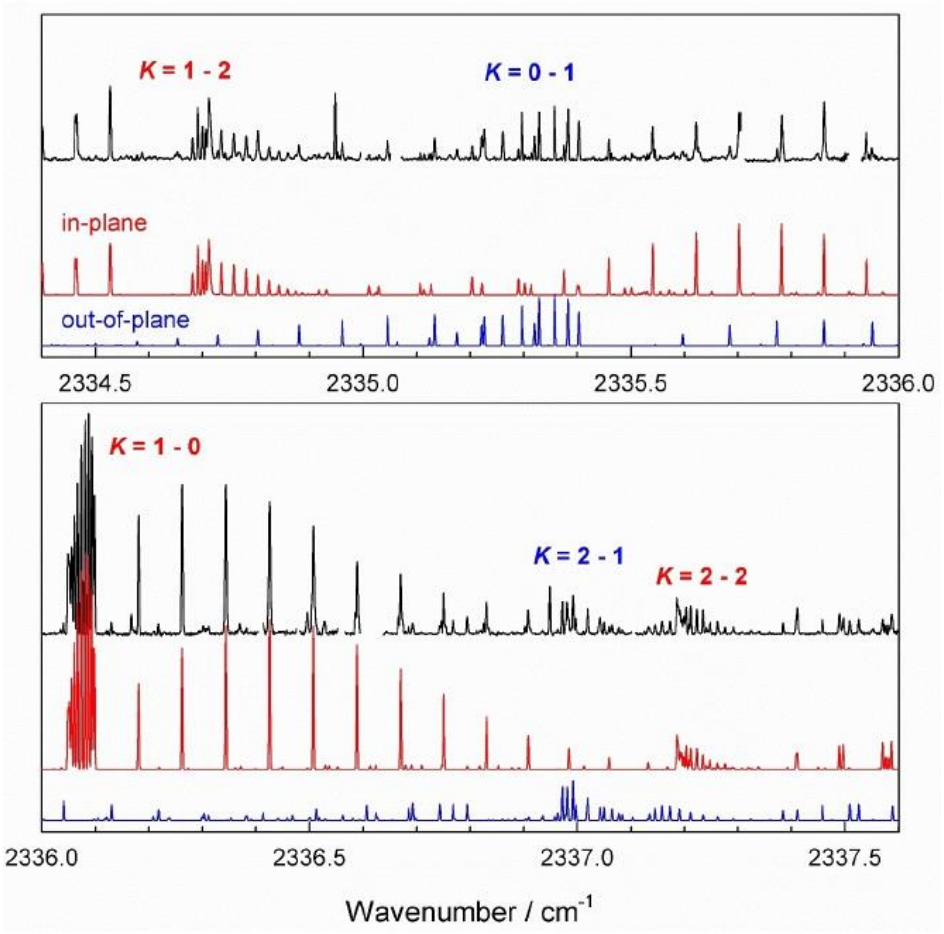

Figure 4.3: Observed (black) and simulated spectra of CO_2-Kr in the CO_2 (01^11)-(01^10) hot band region

To model the hot band transitions a strong Coriolis mixing (ζ_b =1) was assumed and then varied as transitions were fit to the experimental data. Its near unity value is a reflection that the CO_2 bend is only slightly perturbed by the presence of the Kr atom. One of the important values that allows for the assignment of this spectra is the splitting between the ip and ip bend modes in the CO_2 unit. This splitting was determined to be 1.41cm^{-1} in the ground state and 1.42cm^{-1} in the excited state. Determination of this value is aided by the fact that cross transitions (ip-op, op-ip) are perturbation allowed for this complex (shown in Figure 4.3 as the K_a 2-2 subband). These transitions are possible due to the strong Coriolis mixing between states. The parameter X in Table 4.3 represents

the unknown frequency of the CO_2-Kr intramolecular bend. It is equal to the CO_2 monomer value of 667.38 cm^{-1} plus or minus some small vibrational shift (due to the presence of Kr, likely a few cm^{-1}). From Table 4.3 we can see the band origin shift from the CO_2 monomer (2336.633 cm^{-1}) is determined as -0.886 cm^{-1} and -0.876 cm^{-1} for the ip and op mode respectively. This is very similar to the band shift of -0.885 cm^{-1} for the ν_3 fundamental determined above. Of note is that the higher order distortion parameters for the hot band assignment were fixed at the ground state values from Table 4.2 as varying them did not meaningfully reduce the rms error of the fit

Table 4.3: Molecular parameters for the CO_2-Kr (01^11)-(01^10) hot band

	(010) i-p	(010) o-p	(011) i-p	(011) o-p
σ_0	X	1.41839(23) + X	2335.7497(1) + X	2337.1751(2) + X
A	0.397031(31)	0.396394(59)	0.393839(19)	0.393254(31)
B	0.044592(44)	0.044814(17)	0.0446357(82)	0.044827(56)
C	0.040023(40)	0.0399785(88)	0.0399431(46)	0.039906(52)
ξ_b	0.090232(50)		0.090326(49)	

Units are in cm^{-1}. X is equal to the free CO_2 ν_2 frequency (678.380 cm^{-1}) plus or minus an unknown vibrational shift which is likely to be a few cm^{-1}

A total of 82 infrared transitions were assigned for the hot band resulting in an average rms error of 0.00023 cm^{-1}. As can be seen from Figure 4.3, the dominant features in the spectrum are the K_a 1-0 *Q*-branch of the ip mode as well as the K_a 1-2 (ip), 0-1 (op), and 2-1 (op) subbands.

4.2 Spectroscopic Investigation of the CO_2-H_2O/D_2O/HDO Complexes in the 3.5-4.3 um region

Presented here is the high-resolution infrared spectra of the CO_2-H_2O/D_2O/HDO complexes explored for the first time in the 3.5-4.3μm region. CO_2-H_2O/D_2O are analyzed in the region of the CO_2 ν_3 fundamental band while CO_2-D_2O is also explored in the region of the D_2O ν_3 fundamental (~2785cm^{-1}). CO_2-HDO is then analyzed in the region of the O-D stretching vibration (~2720cm^{-1}). Clusters were created in a supersonic jet expansion as detailed in Section 3.1. A gas mixture of 5 Torr CO_2/15 Torr H_2O/D_2O with a backing pressure of 150 PSI was used to obtain the CO_2 ν_3 bands. The D_2O ν_3 band was obtained with a mixture of 30 Torr CO_2/15 Torr D_2O at a backing pressure of 160 PSI. The CO_2-HDO OD stretching band was obtained via a gas mixture of 90 Torr CO_2/15 Torr HDO with a backing pressure of 160 PSI. All mixtures were set in a 400PSI He buffer gas. The following bands were fit to an asymmetric top Hamiltonian in PGOPHER with a rotational temperature of 2.2K.

4.2.1 The CO_2 ν_3 Fundamental Band of CO_2-H_2O

The experimental spectrum for the asymmetric stretch of the CO_2 unit in CO_2-H_2O is shown in the top panel of Figure 4.4 below. This molecule, along with CO_2-D_2O, belongs to the G_8 isometric group (Section 2.5). PGOPHER uses the molecular symmetry group of a molecule to simulate rovibrational transitions and does not include G_8 as an allowable symmetry input. As such, the asymmetric top Hamiltonian of the molecule is modelled with C_{2v} symmetry (which is isomorphic to the G_4 isometric group) with the correspondence between irreducible representations between G_8 and G_4 listed below. From the correlations in Table 4.4 we see that the CO_2 asymmetric stretching vibration, determined to be of symmetry B_2' in Section 2.9, reduces to B_2 in the G_4 group.

Table 4.4: Irreducible representation correspondence between symmetry groups G_8 and G_4

G_8	G_4
A_1', B_2''	A_1
A_2', B_1''	A_2
A_1', B_1'	B_1
A_2'', B_2'	B_2

As per Section 2.9 this band exhibits *b*-type transitions ($\Delta k_a = \pm 1$) as the vibration occurs parallel to the inertial *b*-axis of the molecule. Internal rotation of the CO_2 and H_2O monomers around the van der Waals bond causes a tunnelling splitting of the rotational energy levels in the vibrational states. Due to this internal rotation only k_a=*even* rotational states are populated in the ground vibrational state for the lower tunnelling state (with spin weight 1 labelled as "para") and k_a=*odd* rotational states are populated for the upper tunnelling state (with spin weight 3 labelled as "ortho"). It is worth nothing that these "para" and "ortho" labels represent two different complexes that do not interconvert. These even/odd values are reversed for the tunnelling states in the excited CO_2 ν_3 vibrational state.

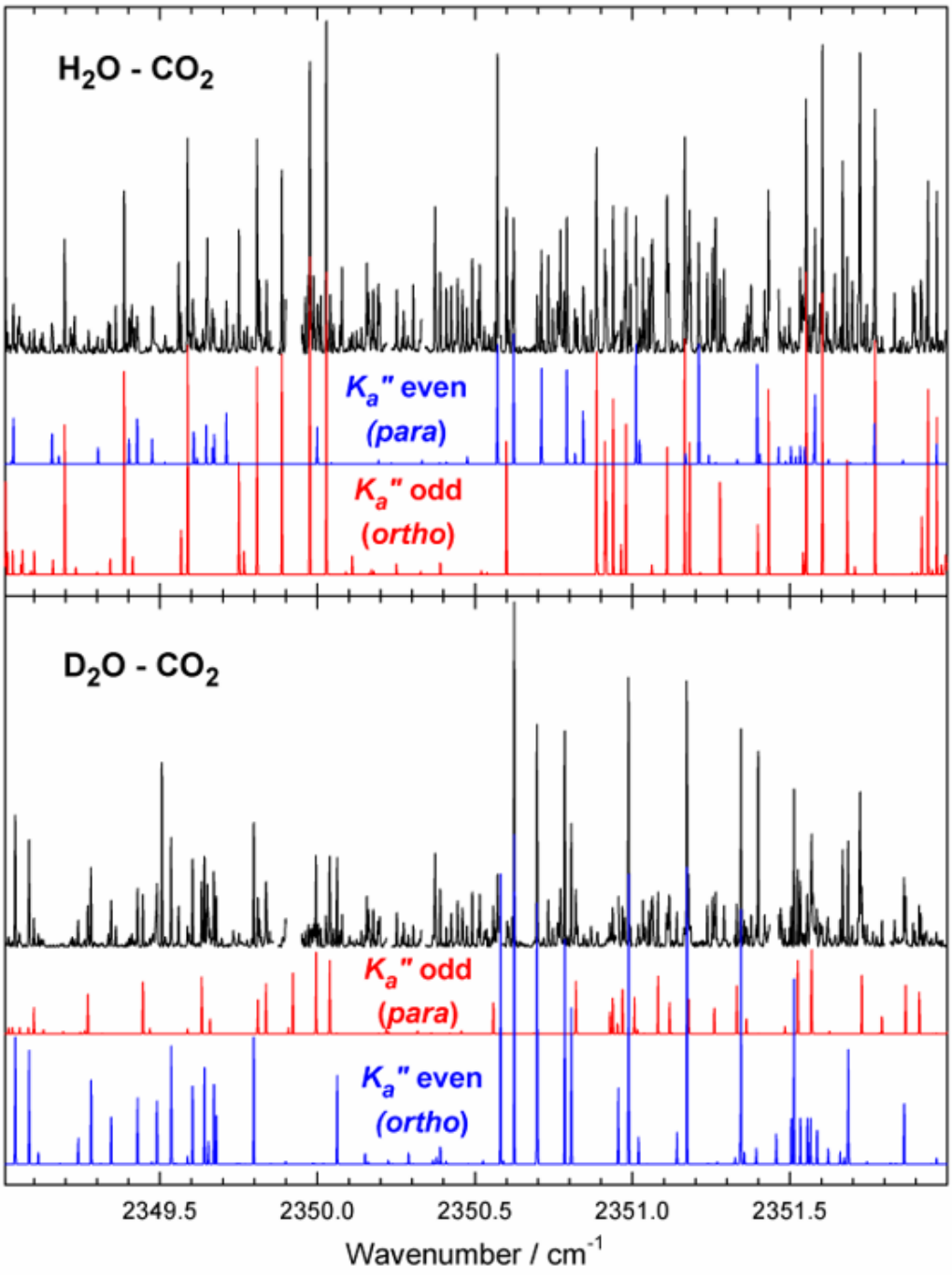

Figure 4.4. Observed (black) and simulated spectra of H_2O- and D_2O-CO_2 in the region of the CO_2 ν_3 fundamental. Small gaps in the observed spectra correspond to regions of absorption by CO_2 and CO_2-He. Para and ortho labels indicate the smaller and larger spin weight components respectively.

The simulated spectrum includes 93 infrared transitions with values for k_a ranging from 0 to 5 and J values ranging from 0 to 9 as well as 33 microwave transitions as measured by Columberg *et al.* [23] which have been weighted by a factor of 1200 to reflect their higher precision. Ground state parameters for the rotational constants and higher order distortion terms were fixed at the values reported by Columberg *et al.* [23] as varying them did not result in noticeable improvement in the fit. The distortion parameters were also fixed at these values for the excited vibrational state for the same reason. Fit parameters for the CO_2 ν_3 fundamental are listed in Table 4.5.

Table 4.5: Molecular parameters for the CO_2 ν_3 band of CO_2-H_2O

	k_a' odd k_a'' even	k_a' even k_a'' odd
ν_0	2350.30095(7)	2350.30255(5)
A'	0.3811376(61)	0.3806881(57)
B'	0.1559383(69)	0.1559413(33)
C'	0.1099601(59)	0.1099791(26)
A''	[0.3840898]	[0.3836397]
B''	[0.155921644]	[0.155943835]
C''	[0.110221172]	[0.110230183]
Δ_K''	[-1.067 e-5]	
Δ_{JK}''	[1.11490 e-5]	
Δ_J''	[9.4682 e-7]	
δ_k''	[7.778 e-6]	
δ_J''	[2.821 e-7]	

Units are in cm^{-1}. Quantities in parentheses are 1σ from the least squares fit, in units of the last quoted digit of the quantity itself. Quantities in square brackets were fixed at the indicated values.

Average rms errors in the simulation were 0.00021 cm^{-1} for the infrared transitions and 4 kHz for the microwave. As predicted by the statistical weight calculations for this band we see that there is a 3:1 intensity alteration between the two simulated bands with the stronger transitions connecting the upper tunnelling states of the ground and excited vibrational states.

It is not possible to determine a value of the tunnelling splittings in the CO_2 ν_3 region. This is due to the symmetry of the CO_2 ν_3 vibrational mode and its effect on the overall symmetry of the total internal wavefunction of the molecule. The difference in band origins of the two simulated *b*-type bands yields a value of the difference in tunnelling splittings in the ground and excited states; here this is determined as 0.0016 cm^{-1}. This signifies a small difference in the magnitude of splitting's of the ground and excited vibrational states due to internal rotation of the monomers with the tunnelling splitting in the excited vibrational mode being slightly smaller.

4.2.2 The CO_2 ν_3 and D_2O ν_3 Fundamental Bands of CO_2-D_2O

The symmetry of CO_2-D_2O molecular vibrations are equivalent for those described for the CO_2-H_2O molecule except for the change in the statistical weights of the complex. From Section 2.8 we see that the H_2O containing complex has a 3:1 nuclear spin weight for k_a odd:even subbands while the D_2O containing molecule shows a 6:3 spin weight with the k_a even subband possessing stronger intensity. This reversal of subband intensities does not affect the spectral fitting process, it is simply a by-product of the symmetry species of the total internal wavefunction of the molecule. The experimental spectrum for the asymmetric stretch of the CO_2 unit in CO_2-D_2O is shown in the bottom panel of Figure 4.4. This is again a *b*-type ($\Delta k_a = \pm 1$) band and exhibits a similar overall shape to the H_2O containing complex in the same region. The D_2O containing complex was also studied in the region of the D_2O ν_3 asymmetric stretch with the resulting experimental spectrum and simulation shown in Figure 4.5. This is also a *b*-type band as shown from calculations in Appendix D.

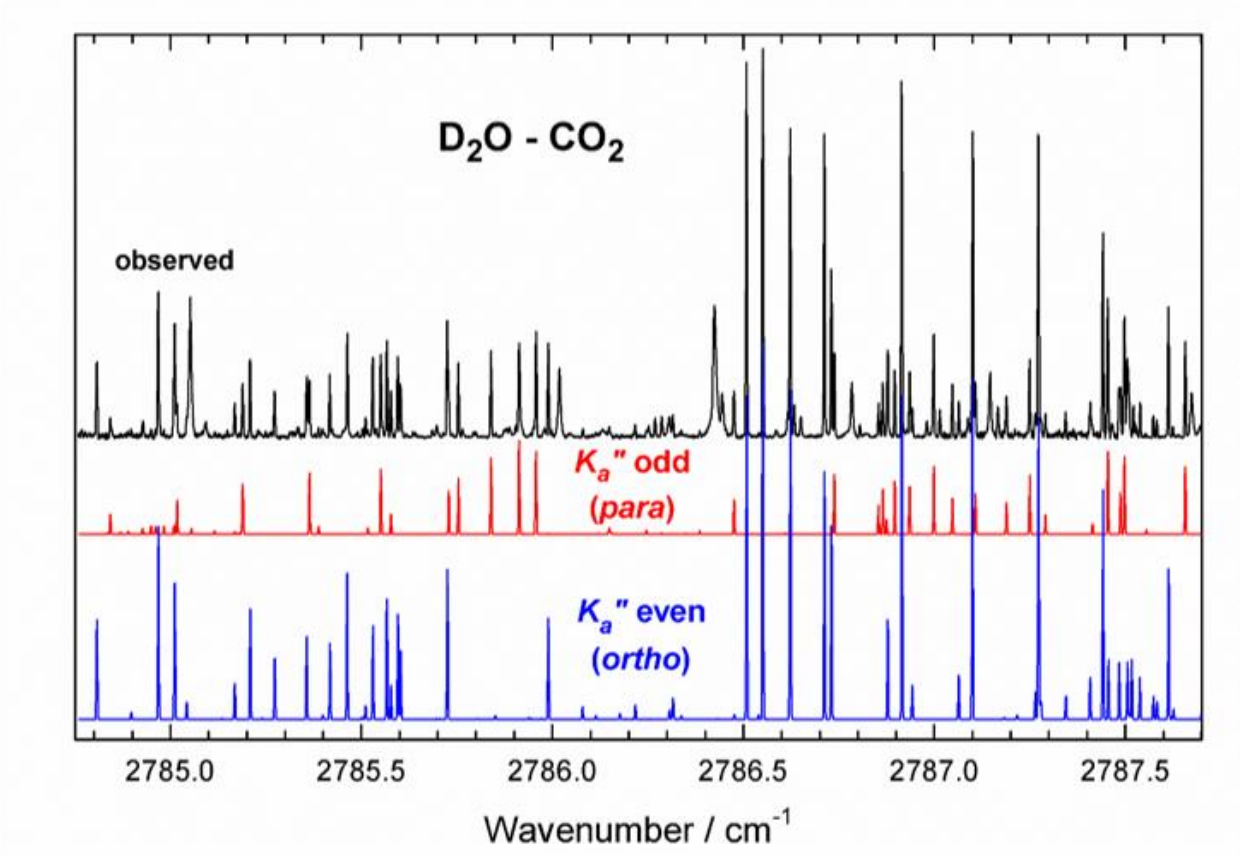

Figure 4.5. Observed and simulated spectra of D_2O-CO_2 in the region of the D_2O ν_3 fundamental.

The simulated CO_2 ν_3 spectrum includes 117 infrared transitions with k_a values ranging from 0 to 5 and J values ranging from 0 to 9. The simulated D_2O ν_3 spectrum includes 98 infrared transitions with k_a values ranging from 0 to 4 and J values ranging from 0 to 8. Both bands were also fit with 20 microwave transitions as measured by Columberg *et al.* [23] which have been weighted by a factor of 1200 to reflect their higher precision. The rms errors for the two bands are 0.00015 cm^{-1} and 0.00040 cm^{-1} in the CO_2 and D_2O regions respectively. The larger residual error for the deuterium band is a result of a handful of small upper state perturbations (for example, the levels J_{KaKc} = 3_{13} and 5_{33} were each observed to be about 0.001 cm^{-1} higher than calculated). Molecular parameters for the D_2O bands are listed in Table 4.6.

Table 4.6: Molecular parameters for the CO_2 ν_3 and D_2O ν_3 bands of CO_2-D_2O

	k_a' odd k_a'' even		k_a' even k_a'' odd	
ν_0	2350.31240(7)	2786.2364(1)	2350.31259(8)	2786.2306(1)
A'	0.3714975(70)	0.374404(39)	0.3714506(88)	0.374265(44)
B'	0.1406504(43)	0.1404079(87)	0.1406555(84)	0.140367(16)
C'	0.1015046(29)	0.101603(10)	0.1014894(54)	0.101585(10)
Δ_K'	[-0.965 e-5]	1.50(30) e-5	[-0.965 e-5]	[1.50 e-5]
Δ_{JK}'	[1.03530 e-5]	-1.44(10) e-5	[1.03530 e-5]	[-1.44 e-5]
Δ_J'	[7.356 e-7]	1.36(14) e-6	[7.356 e-7]	[1.36 e-6]
A''	0.3742939(12)		0.3742670(82)	
B''	0.14064516(29)		0.14064591(15)	
C''	0.10171025(27)		0.10171023(15)	
Δ_K''	-0.965(29) e-5			
Δ_{JK}''	1.03530(95) e-5			
Δ_J''	7.356(24) e-7			
δ_k''	7.062(67) e-6			
δ_J''	2.1118(58) e-7			

Units are in cm^{-1}. Quantities in parentheses are 1σ from the least squares fit, in units of the last quoted digit of the quantity itself. Ground state parameters are from our fit to previous microwave data [23] plus slected ground state combination differences from the present spectra. Excited state centrifugal distortion parameters for the 2350 cm^{-1} band were fixed at ground state values, and those for the 2786 cm^{-1} band were constrained equal for the two tunneling components as indicated. Quantities in square brackets were fixed at the indicated values.

For the CO_2 region the difference in band origins for the excited and ground states yields the difference in tunnelling splittings for the lower and upper tunnelling states as it did in the H_2O case; here we determine this value to be 1.9 x 10^{-4} cm^{-1}, even smaller than for the water containing complex signifying that the energy shift due to tunnelling is even less dependent on the vibrational mode.

The B_2'' symmetry of the D_2O ν_3 vibrational mode leads to transitions connecting lower to upper and upper to lower tunnelling states in the ground and excited states (see Figure D2, Appendix D). This allows for the direct determination of the tunnelling splittings for the lowest tunnelling states of the complex (A_1' *and* A_1'') by means of the difference in band origin shifts for

the k_a even and k_a odd subbands. Here the difference in subband origins is the summation of the ground and excited vibrational tunnelling splittings. The value for the summation of the ground and excited tunnelling splittings is thus determined here to be 0.0058 cm^{-1}. Assuming that the magnitude of the tunnelling splitting is negligibly affected by the vibrational mode in the excited state one can divide this number by two to approximate the magnitude of the individual tunnelling splittings[1]. From this analysis we determine a splitting of 0.0029 cm^{-1} for the A_1' and A_1'' tunneling states, which is in good agreement with the value reported by Felker *et al.* [27] of 0.0039 cm^{-1} by means of a 5D quantum mechanical calculation.

4.2.3 The O-D Stretching Band of CO_2-HDO

The experimental spectrum for the OD stretch in CO_2-HDO is shown in Figure 4.6. This was determined in Appendix D to be a hybrid *a*-, *b*-type band which has four possible pathways connecting the tunnelling states. The *a*-type bands are noticeably weaker (by a factor of ~5) than their *b*-type counterparts as the angle of the OD bond in the HDO monomer has a much larger projection along the inertial b-axis of the molecule (but not completely parallel to this axis), so the component of the transition moment is greater along this axis. While calculation of the symmetry of these transitions was done using the G_4 isometric group, in PGOPHER the only choice of symmetry analogous to this is the C_{2v} (MS) group, thus this symmetry was used in the simulation. Noting that hybrid transitions are not possible under C_{2v} symmetry (in this symmetry only one component of the transition moment can contribute), a feature in PGOPHER called "*FakeSym*" was used to allow for the inclusion of the *a*-type bands by means of disabling the exclusion of forbidden transitions along the other principal axes (in this case the *a* inertial axis as the OD bond

[1] Note that this is a "back of the envelope" calculation. The vibrational mode may have a noticeable effect on the magnitude of the tunneling splitting value with tunneling motions most likely hindered in excited vibrational states.

forms an angle with both the *a*- and *b*-axes). From Figure D3 in Appendix D we can see that the *a*-type transitions measure the different in the tunnelling splittings in the ground and excited vibrational states, and the *b*-type transitions measure the sum of the tunnelling splittings and should thus allow for the direct determination of the tunnelling splitting of the ground vibrational state.

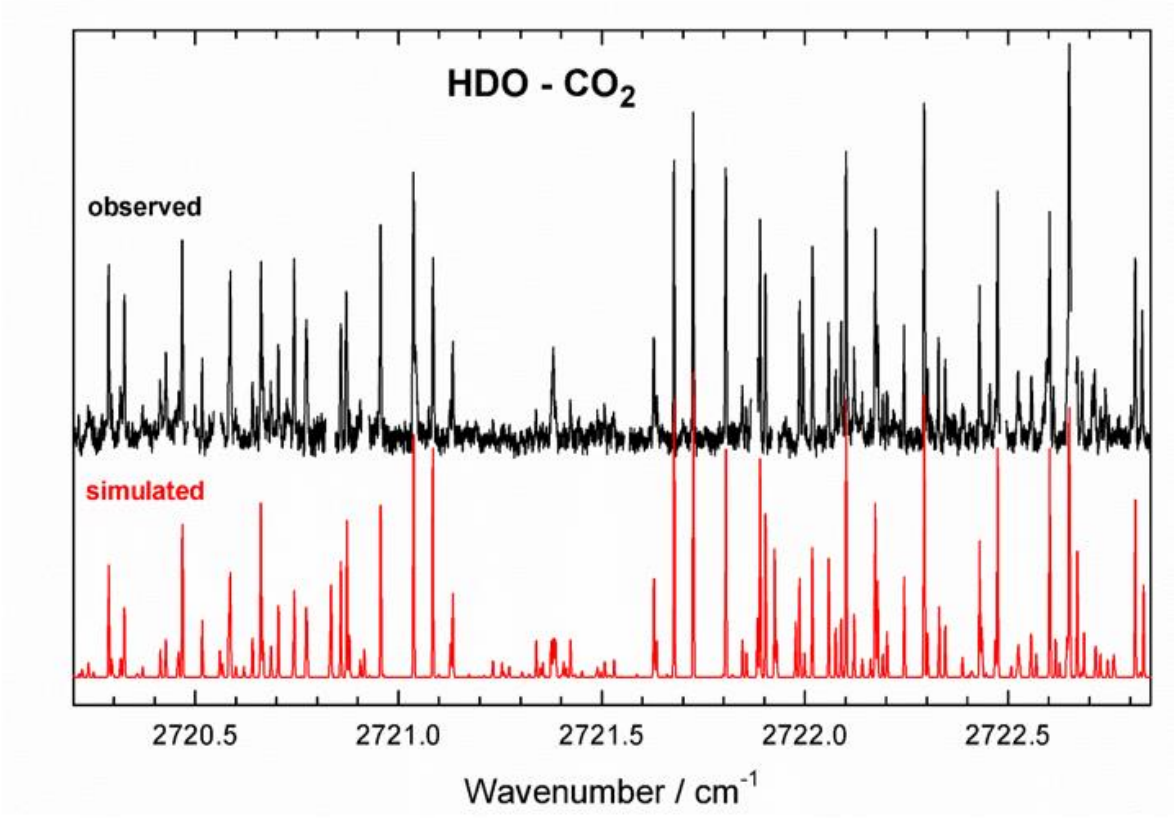

Figure 4.6. Observed and simulated spectra of HDO-CO_2 in the region of the O-D stretch fundamental of HDO.

The simulated spectrum included 83 infrared transitions with k_a values ranging from 0 to 3 and *J* values ranging from 0 to 8. The majority of these, 61, were *b*-type bands with the remainder *a*-type. 25 microwave transitions from Columberg *et al*. [23] were also fit in the simulation, weighted in a similar manner as discussed for the previously analyzed bands. Ground and excited state rotational parameters and higher order distortion parameters were varied in the fit with some

notable constraints (Table 4.7). The value for the excited state *A* rotational constant was not reliably determined for the upper tunnelling state and was fixed at a reasonable value as shown in Table 4.7. Distortion parameter Δ_k could also not be meaningfully determined and was set to zero for all states. As was the case with CO_2-D_2O some states were noticeably perturbed and were thus given reduced weights in the fit (these states include $J_{KaKc} = 4_{23}$, with a residual -0.0013 cm^{-1}, 6_{16} (-0.0038 cm^{-1}), and 5_{24} (+0.0205 cm^{-1})). Larger perturbations are likely present but are not resolvable as they may cause certain transitions to shift too far from their calculated positions.

Table 4.7: Molecular parameters for the O-D stretching band of CO_2-HDO

	k_a' odd k_a'' even	k_a' even k_a'' odd
σ_0'	2721.4051(1)	2721.3820(2)
A'	[0.379]	0.379464(68)
B'	0.147591(76)	0.14689(40)
C'	0.105968(93)	0.10670(38)
Δ_{JK}'	-1.82(40) e-5	[1.0610 e-5]
Δ_J'	-4.3(14) e-6	4.5(20) e-6
δ_k'	-1.30(46) e-4	-2.5(11) e-4
δ_J'	[2.6596 e-7]	[2.227 e-7]
σ_0''	0.00	0.023443(67)
A''	0.379584(19)	0.379396(36)
B''	0.14787473(87)	0.14787264(108)
C''	0.10581199(83)	0.10580041(93)
Δ_{JK}''	1.0610(13) e-5	8.15(70) e-6
Δ_J''	0.8847(27) e-7	8.263(87) e-7
δ_k''	8.705(51) e-6	7.54(38) e-6
δ_J''	2.227(36) e-7	2.6596(93) e-7

Units are in cm^{-1}. Quantities in parentheses are 1σ from the least squares fit, in units of the last quoted digit of the quantity itself. Ground state parameters are from our fit to previous microwave data [23] plus slected ground state combination differences from the present spectra. Note that σ_0 represents vibrational term value energy, not band origin. Distortion parameter Δ_k could not be determined and was fixed to zero for all states. Excited state distortion parameters in square brackets were fixed at their ground state values for the appropriate (lower or upper) tunneling component. Excited state distortion parameters which were varied may not be meaningful (see text).

Part II

Finite Difference Time Domain (FDTD) Analysis of Grating Coupled Silicon-on-Sapphire Microring Resonators

5. Introduction

The rapid growth in the study and manufacture of silicon based photonic components since the 1990's rivals that of the first silicon-based transistors which now form the basis for modern electrical circuitry. Built upon a silicon-on-insulator technology platform that is compatible with large scale existing complimentary metal-oxide-semiconductor (CMOS) fabrication techniques modern silicon photonics show extreme promise for the implementation of a broad range of chip-scale optical processes which include frequency comb generation [50], bio-sensing [51], atmospheric sensing [52], and high-capacity optical data transmission [53] among many others. Silicon-on-insulator integrated optical circuits have largely been studied in the telecommunications band (~1550nm) due to the wide availability of high-quality silicon and silicon oxide substrate materials historically used in transistor development. The high refractive index contrast between layers on a silicon and silicon dioxide wafer allows for the strong optical confinement necessary for the development of low loss optical circuitry on a nanometer scale. By using existing fabrication methodologies on modern silicon-on-insulator based wafers one can develop compact circuitry capable of housing millions of individual optical components into chip-scale footprints; this allows for the development of complex optical systems driven by minimal power inputs in the smallest volume possible [54].

While the traditional wafer material of silicon-on-silicon-dioxide has driven exponential advancement of photonic development in the telecom region its usefulness at longer wavelengths is severely limited due to the absorptive nature of silicon-dioxide past the 3 μm mark. Pure crystalline silicon itself is optically transparent past 8μm (as measured by a 2 dB cm^{-1} loss) and is thus still a preferred waveguiding material due to its wide availability and high refractive index contrast to most other substrate materials [55]. As such, a large effort has been put forth by the

research community over the past two decades to develop other low loss substrate materials suitable for use past the 3 μm range, moving into the near-, mid-, and long-range infrared region. Quality development of these substrate materials is crucial for the efficacy of photonics at other wavelength regions.

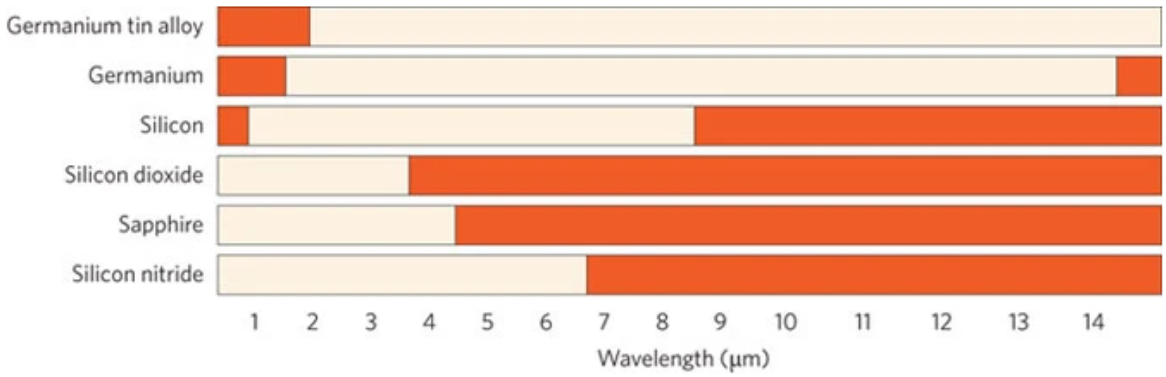

Figure 5.1: Materials transparency in the infrared wavelength region. White areas denote optical loss less than 2 dB cm^{-1} [55]

The movement to advance silicon photonics materials science to the mid and long wave infrared regions is driven, in part, by location of the "molecular fingerprint region", a wavelength region in which many common atmospheric molecules show strong, unique absorption signatures that are orders of magnitude stronger than their near-infrared counterparts [56]. Below is a snapshot of some of the important complexes that comprise the fingerprint region. The use-case for silicon photonics in this region is mainly comprised of the development of chip-based sensors capable of temperature and refractive index sensing. The development of on-chip diode based infrared optical sources [57] and detectors [58] is also of extreme interest in the quest for a functional, totally enclosed "lab-on-a-chip" sensing solution.

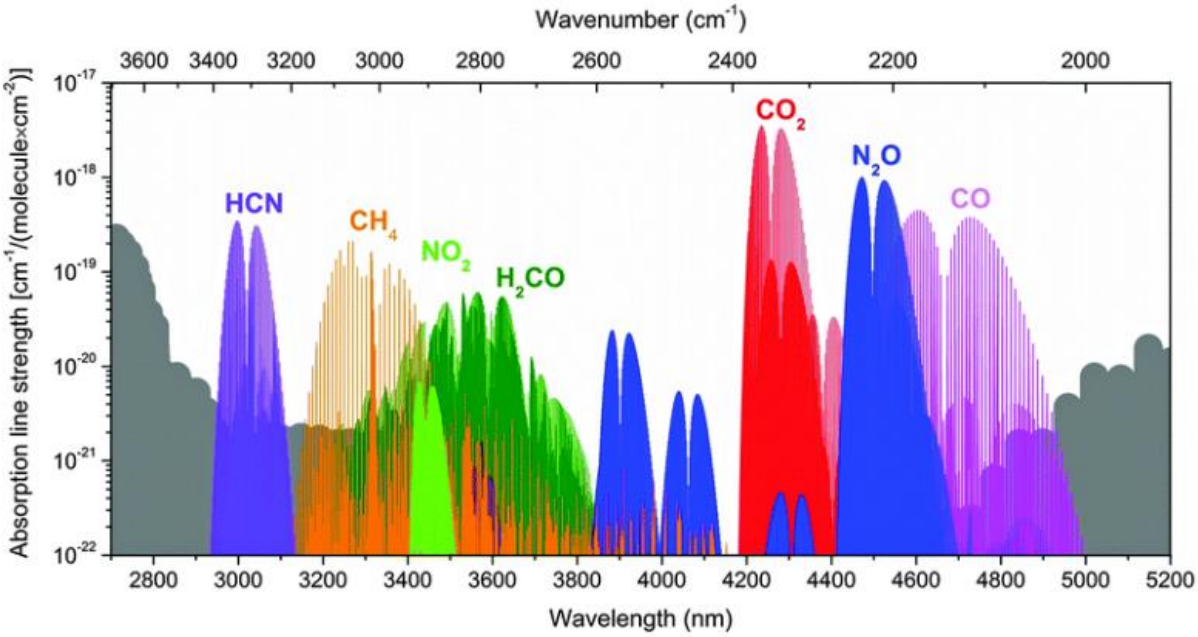

Figure 5.2: Molecular absorption signatures of common complexes in the mid-infrared region [56]

Numerous forays into the study of alternative substrate materials suitable for use in photonic circuits in the mid and long wave infrared region have been demonstrated which use sapphire, germanium, silicon nitride, aluminum nitride, gallium arsenide, chalco-genide glass, and calcium fluoride, among many others [59]. The challenge in the development of these materials is to produce low loss optical substrates while reducing manufacturing and patterning complexity and maintaining CMOS compatibility for use in integrated circuitry. While the research base of mid-infrared photonics is large and widely varied, I will briefly discuss some of the interesting and cutting-edge publications which demonstrate the efficacy of mid-infrared photonics as they pertain to the development of low loss waveguides, high quality factor optical cavities and atmospheric sensing,

5.1 Previous Work in Mid-Infrared Photonics

Some of the first studies on silicon photonics in the mid-infrared involved waveguide analysis of silicon-on-sapphire (SoS) wafer-based systems. Single mode waveguides of varying dimensions operating near 4.5 μm achieving losses in the range of 4.3 dB cm^{-1} were reported by Beahr-Jones *et al.* [60] via butt coupling of a nD:YAG optical parametric generator/difference frequency generator to the patterned chip. This was the first study that showed relatively low loss waveguiding systems could operate in the mid-infrared wavelength region. Li *et al.* [61] showed waveguiding was possible with losses <2 dB cm^{-1} near 5.2 μm with a SiO_2 clad SoS wafer material. This study used a butt-fiber coupled quantum cascade laser source to characterize the waveguides. Huang *et al.* [62] conducted a FDTD based numerical analysis of various SoS waveguide geometries (rib, strip, slot) and their suitability to act as evanescent field absorption sensors for trace gas emissions. They concluded that a 1 cm air clad SoS strip waveguiding system can detect trace gases to as low as two parts per million (ppm) with an evanescent field ratio greater than 25% using cooled InSb mid-IR detectors. Liu *et el.* [63] reported single mode SoS ring resonators operating near the 5.5 μm mark which demonstrated a waveguide loss of 4.1 dB cm^{-1} and a quality factor (Q-factor) of 1400. Shankar *et al.* [64] developed some of the highest quality factor ring resonators on the SoS platform achieving Q-factors of ~50,000 for untreated wafers and upwards of ~200,000 for wafers treated with a post processing chemical bath and thermal baking operating near 4.5 μm. These resonators were designed for use with focused free space light incident upon the first reported SoS on-chip grating couplers which achieved an experimental coupling efficiency of ~4%. The untreated SoS ring resonators were later used in a study to sense trace nitrous oxide in a controlled gas environment. This experiment showed that a SoS resonator with a 10^5 quality factor could sense analytes with absorption coefficients as low as 0.5 cm^{-1} [65].

While not the obvious choice as a wafer material due to the material absorption of the buried oxide layer, traditional silicon-on-insulator wafers have also been used in the mid-infrared region with a few studies exploring their suitability for waveguiding at longer wavelengths. The most notable of these studies is from Miller *et al.* [66] which showed a relatively large waveguide of dimensions 2300 nm x 4000 nm would result in extremely strong confinement of the optical mode in the core material out to 3.8 μm. They demonstrated that ring resonators based on this waveguide geometry could achieve Q-factors as high as 10^6, some of the highest reported in the mid-infrared. They also showed that waveguides of this size on the silicon-on-insulator platform meet modal confinement requirements necessary for frequency comb generation.

Germanium is another popular choice for wafer material in the mid-infrared wavelength region, although not as readily available as sapphire and requiring a more complicated process to pattern in traditional lithography machines. Regardless, numerous studies have shown germanium's efficacy as a wave guiding material with studies from Xiao *et al.* [67] demonstrating high Q (~57,000) ring resonators near 5 μm with 5.4 dB cm^{-1} loss and Osman *et al.* [68] demonstrating suspended germanium waveguides operating neat 7.6 μm capable of losses less than 3 dB cm^{-1}.

Numerous absorption studies on varying wafer platforms have been carried out which demonstrate the ability of mid-IR photonics to sense atmospheric constituents down to meaningful levels. Ranacher *et al.* [69] developed a suspended silicon-on-silicon nitride straight waveguide sensor that made use of grating couplers to couple a fiber based QCL source at 4.25μm. The sensor demonstrated CO_2 detection down to 5000 ppm which is a workplace maximum in many north American jurisdictions. Methane absorption sensing has been demonstrated in [65] on the SoS platform as well as in chalcogenide glass waveguides as demonstrated by Su *et al.* [70] which

showed a 5mm long spiral waveguide operating near ~3.2 μm was capable of sensing methane concentrations as low as 330 ppm complete with on-chip detection. Zhang *et al.* [71] have also demonstrated a fully integrated on-chip sensing platform for methane which uses a spiral waveguide, on-chip reference gas cell, thermal tuning, and an on-chip cavity laser source and detector. This is the first demonstration of a truly integrated sensing solution which miniaturizes most of the necessary components to resolve the absorption spectrum of a molecular species such as methane. This system has an overall detection limit of ~90 ppm and the overall size of the assembled components is roughly 5 cm^2, weighing 0.2kg [71].

5.2 Optical Input/Output

The above studies use various methodologies to couple free space light (whether via optical fiber or lens) to the nano/micro sized features on the silicon wafers. The large majority use a technique called butt coupling which involves cleaving the wafer material at a 90-degree angle to create a smooth edge in the silicon waveguide. Light can then be focused onto the cleaved facet end of the waveguide for optical coupling into the waveguiding structure (achieving total internal reflection at the material boundary). This methodology limits the flexibility in chip design afforded by other means like grating couplers as the cleaved facets require that all waveguides terminate at the edge of the chip. The traditional method of coupling into a grating structure is via an optical fiber as the mode mismatch between the fiber and the waveguide of the grating is smaller than that of the mode of a free space optical beam. Scant availability and reliability of optical fiber in the mid-infrared has thus far limited the available studies pertaining to the development of gratings in the mid-IR region. The only study mentioned so far to use a grating coupler for optical input is [65] which developed a 50μm wide grating region for coupling lens focused fee space QCL light into the ring resonator structure. Due to manufacturing tolerances these couplers demonstrated a

theoretical efficiency of ~40% but an experimental efficiency of only ~4%. Cheng *et al.* [71] have demonstrated fiber coupling with a ZBLAN mid-IR fiber to/from shallow etched SoS grating couplers with a reported theoretical efficiency of 80% and an experimental efficiency of 32%. As a comparison, in the telecom band, where optic fiber is common and produced with extremely high manufacturing tolerance, studies show experimental coupling efficiencies as high as 70% using telecom optical fibre with lensed tips and a BOX stacking design methodology [89] and ultra-high efficiency subwavelength grating couplers have also been numerically demonstrated using telecom fiber coupling with theoretical efficiency near unity [72] designed by gradient based algorithms.

6. Theoretical Background

6.1 Waveguide Modes

A dielectric waveguide is a structure that uses a high refractive index contrast between the waveguide material and the surrounding cladding to confine optical power for the purposes of transmission down a propagation axis. The behavior of an electromagnetic wave inside of a waveguiding medium is best understood in terms of Maxwell's equations for the curl of the electric (*E)* and magnetic fields (*H)* and their related electric (*D)* and magnetic (*B)* flux through a membrane.

$$\nabla \times \boldsymbol{E} = -\frac{\partial \mathbf{B}}{\partial \mathrm{t}} \tag{6.1}$$

$$\nabla \times \boldsymbol{H} = -\frac{\partial \mathbf{D}}{\partial \mathrm{t}} \tag{6.2}$$

$$\nabla \cdot \boldsymbol{D} = 0 \tag{6.3}$$

$$\nabla \cdot \boldsymbol{B} = 0 \tag{6.4}$$

From Maxwell's equations one can derive the second order partial differential wave equations that describe the propagation of an electromagnetic wave in a medium (for both the **E** and **H** fields where $\boldsymbol{\mu}$ *and* $\boldsymbol{\varepsilon}$ are the magnetic and electric permittivity's of the propagation medium respectively) [79]

$$\nabla^2 \boldsymbol{E} - \boldsymbol{\mu\varepsilon}\frac{\partial^2 \mathbf{E}}{\partial t^2} = 0 \tag{6.5}$$

$$\nabla^2 \boldsymbol{H} - \boldsymbol{\mu\varepsilon}\frac{\partial^2 \mathbf{H}}{\partial t^2} = 0 \tag{6.6}$$

Solutions to the electric and magnetic wave equations constitute what are known as "modes", which are electromagnetic waves that propagate inside of a waveguiding medium in a discrete set of transverse intensity profiles. These modes have distinct propagation constants and velocities and exists in orthogonal polarizations (with **E** $\perp$ **H**). Modes are solutions to the electric and magnetic wave equations which take the form (for the **E** and **H** fields respectively) [79]

$$E_m(r,t) = E_m(x,y)e^{i(\beta_m z - i\omega t)} \tag{6.7}$$

$$H_m(r,t) = H_m(x,y)e^{i(\beta_m z - i\omega t)} \tag{6.8}$$

Where *m* is the integer mode index, β_m is the wave propagation constant, ω is the mode frequency, and *z* is the propagation axis of the waveguide.

As mentioned, a mode propagates in a waveguiding medium with an invariant transverse intensity profile, meaning that the shape of the **E** and **H** field distribution is constant down the "face" of the waveguide. Modes are commonly defined by their effective index, n_{eff}, which is defined as

$$n_{eff} = \frac{\beta\lambda_0}{2\pi} \tag{6.9}$$

Where λ_0 is the wavelength of light propagating in the waveguide. The effective index is a measure of the strength of optical confinement inside the waveguide, with a higher effective index signifying less optical loss to the surrounding substrate. Modes are routinely referred to as either guided or radiative based on the level of confinement of optical power which is a function of the geometry of the waveguide and the wavelength of light. This can be understood in terms of the coupling angles of the light upon entry into a waveguide as shown in Figure 6.1.

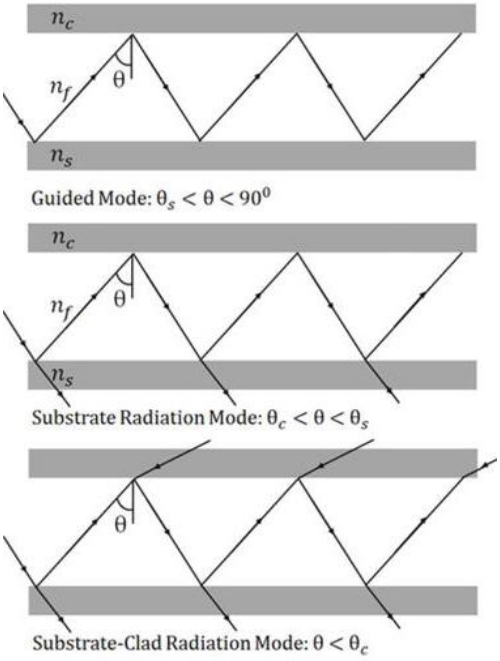

Figure 6.1: Guided vs. Radiative Mode Schematic [79]

In Figure 6.1 the optical confinement is determined by the critical angle of the reflecting light as it reaches a refractive index boundary of the waveguide (*c* for cladding, *s* for substrate). Modes with a refractive index larger than the cladding material are said to be guided and energy due to substrate loss is decayed in the transverse directions. This can be written as the guided mode condition [78]

$$n_{wavguide} > n_{eff} > n_{cladding} \tag{6.10}$$

Modes that do not satisfy the above condition are deemed radiative and lose power to the surrounding cladding materials as the wave propagates at a high rate; this causes the electromagnetic wave to decay exponentially along the waveguide propagation axis.

Modes exists not only in a discrete set of intensity profiles but are polarization dependent as well due to the orthogonality between the **E** and **H** fields. Based on the appropriate field orientation modes can be labelled as either transverse electric (TE) or transverse magnetic (TM)

Table 6.1: TE and TM mode propagation vector components

	E_z	H_z
TE	0	≠0
TM	≠0	0

It is worth noting that dielectric waveguides do not support hybrid-TEM modes as they do not satisfy the boundary conditions imposed upon the electromagnetic wave in the electric and magnetic wave equation. As such dielectric waveguide modes are discrete in both field intensity profile and polarization.

6.2 Grating Coupler

A grating coupler is a structure with a periodically varying effective index area (gratings) used to diffract a free space optical source into or out of a waveguide. Figure 6.2 depicts a cross section of a generalized output grating coupler with important parameters.

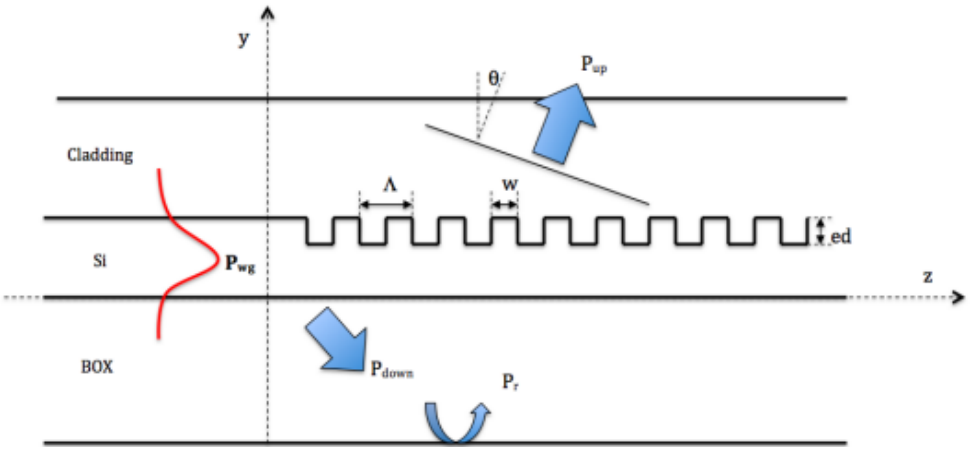

Figure 6.2: Generalized output grating coupler schematic [73]

As can be seen from Figure 6.2 the grating coupler in question consists of a silicon waveguide core sandwiched by a substrate material (BOX) on the bottom and a cladding material on top. Depending on the application the upper cladding may be removed so that the silicon core is exposed directly to the environment and the BOX layer may consist of multiple sublayers of varying refractive indices. The grating "teeth" form a periodic etched structure which performs the task of diffracting power from an optical source to/from a waveguide. The periodicity of the gratings is given by the parameter Λ with the width of a grating "tooth" labelled *w*. Etch depth of the grating (in the silicon layer) is labelled *ed.* As can be seen from Figure 6.2, for the output grating, power propagating in the waveguide mode is diffracted both up and down into the cladding and BOX layer respectively. Depending on the exact geometry of the gratings and the mode propagating in the silicon waveguide power will be diffracted at different angles upon input/output from the device.

The operation of the grating coupler is described by the Bragg condition which relates the propagation constant of the waveguide to the periodicity of the grating teeth for light scattering on

a crystalline surface. The propagation constant, as a function of the waveguide effective index, is given as [73]

$$\beta = \frac{2\pi n_{eff}}{\lambda_0} \tag{6.11}$$

Where n_{eff} is the effective index of the waveguide and λ_0 is the wavelength of light in vacuum.

The Bragg condition is then written as

$$\beta - k_x = m * K \tag{6.12}$$

Where k_x is the directional component of the diffracted wave, m is the diffraction order (integer), and $K = \frac{2\pi}{\Lambda}$ (which is known as the grating constant).

Upon diffraction due to the grating structure the travelling wavevector becomes

$$k = \frac{2\pi n_c}{\lambda} \tag{6.13}$$

Where $n_c$is the refractive index of the cladding on top of the grating teeth, and λ is the wavelength, which allows for the determination of the diffraction angle as

$$sin\theta_c = \frac{k_x}{K} = n_{eff}\frac{\lambda}{\Lambda} \tag{6.14}$$

Using Equation 6.14 above the Bragg condition can be simplified to

$$n_{eff} - n_c * sin\theta_c = \frac{\lambda}{\Lambda} \tag{6.15}$$

For the purposes of developing a zeroth order design for a grating structure one can use the Bragg condition, along with the following approximation of the total effective index of the grating region

(tooth and etch), denoted n_{eff_grat} to determine the appropriate periodicity of the gratings. The total effective index of the grating region can be approximated as

$$n_{eff\_grat} = ff * n_{eff1} + (1 - ff) * n_{eff2} \tag{6.16}$$

Where $ff = w/\Lambda$ is the fill factor of the grating region and n_{eff1} and n_{eff2} are the effective indexes of the grating teeth and etched sections respectively. n_{eff_grat} can then be inserted into Equation 6.15 to solve for the grating period for a structure operating in a known wavelength region; this period can then be refined by means of an optimization analysis to arrive at the appropriate design parameters for the case under study

The design of the grating couplers in this thesis uses the above theoretical starting point to arrive at a baseline value for the period of the gratings for use near 4280nm wavelength light. This theory can be expanded to vary both the filling factor and period of the gratings spatially to increase the performance of the gratings (eg. increase coupling efficiency from the free space source). To do this a design methodology developed by Marchetti *et al.* [74] is implemented which apodizes both parameters to effectively parametrize the position of each individual grating tooth wall to increase device efficiency; these wall positions are then optimized in a finite difference time domain (FDTD) solver. By this methodology the filling factor is spatially varied as follows

$$ff(x) = ff_0 - R * x \tag{6.17}$$

Where R is the apodization factor applied to vary the filling factor as a function of position and ff_0 is the initial filling factor [74, 75].

The total effective index of the grating area can thus be written as

$$n_{eff_{grat}}(x) = ff(x) * n_{eff1} + \big(1 - ff(x)\big) * n_{eff2} = n_{eff2} + ff(x)\Delta n \tag{6.18}$$

where $\Delta n = n_{eff1} - n_{eff2}$.

Two further variables are defined as

$$a = n_{eff2} - n_{eff1} sin\theta_c \tag{6.19}$$

$$b = \Delta n \tag{6.20}$$

In total four parameters are needed to implement the design methodology from [74] as inputs into FDTD optimization software, these are $\{x_0, R, a, B\}$, where x_0 is location of the first grating wall of a grating/etch pair. Approximations of these values are easily calculable from the refractive indices of the layers of the grating coupler. By the definitions above the Bragg condition can be written as [74, 75]

$$\Lambda_i = \frac{\lambda}{a + ff_i b} \tag{6.21}$$

Where

$$ff_i = ff_0 - R(x_{i-1} - x_0) \tag{6.22}$$

Here the filling factor and grating wall position is discretized (denoted index *i*) based on the period of each grating section which essentially treats each tooth/etch pair as an individual parameter that can be optimized based on the inputs mentioned above.

Further discussion of how this design methodology is implemented in FDTD software is discussed in Section 7.4.

6.3 Microring Resonator

In its simplest form an optical microrring resonator consists of a straight optical waveguide placed near a ring waveguide. A propagating waveguide mode in the straight (also known as a bus)

waveguide couples its optical power into the ring waveguide via the evanescent field of the propagating mode (the evanescent field describes the radiative portion of the mode which resides outside of the waveguide core). After undergoing a round trip in the ring the optical mode couples back into the bus waveguide by the same evanescent field. When the optical mode propagating in the ring waveguide accumulates a phase shift of 2π the wave couples back into the bus wavguide constructively and the resonator is said to be in resonance. A schematic of a simple all-pass ring resonator can be seen in Figure 6.3.

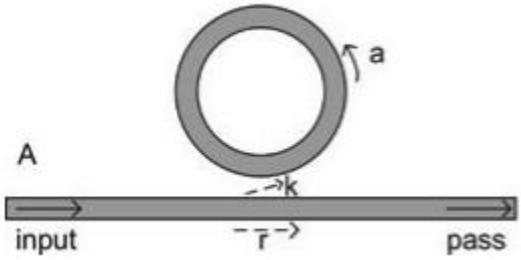

Figure 6.3: Schematic of microring resonator [76]

The ratio of the input power to the throughput of the ring waveguide can be written as [76]

$$\frac{E_{pass}}{E_{input}} = e^{i(\pi+\phi)} \frac{a-re^{-i\phi}}{1-rae^{i\phi}} \tag{6.23}$$

Where a is the single pass amplitude transmission of the ring, r is the self-coupling coefficient of the bus waveguide, and $\phi = \beta L$ is the single pass phase shift of the travelling light wave over a round trip distance L with wave propagation constant β.

Squaring the above equation leads to the determination of the transmitted power intensity of the input wave from the bus waveguide

$$T_n = \frac{I_{pass}}{I_{input}} = \frac{a^2 - 2r\,\mathrm{acos}(\phi) + r^2}{1 + 2arcos(\phi) + (ra)^2} \tag{6.24}$$

The cross-coupling coefficient, k, is also now defined such that $r^2 + k^2 = 1$, which operates on the assumption that the coupling section between the waveguides is lossless (although in practice there is radiative loss in this section).

The resonance condition for the ring resonator occurs when the wavelength of the input light fits an integer number of times into the optical length of the ring, this is given by resonance wavelength

$$\lambda_{res} = \frac{n_{eff}L}{m}, \qquad m = 1, 2, 3 \ldots \tag{6.25}$$

Under perfect, critical coupling between the bus and ring waveguide the single pass transmission of the ring is exactly equal to the coupling coefficient, that is $r = a$, and transmission to the pass end of the bus waveguide drops to zero. This creates the resonance, or notch, profile of power throughput of the ring resonator. A graphical depiction of this transmission profile is shown in Figure 6.4.

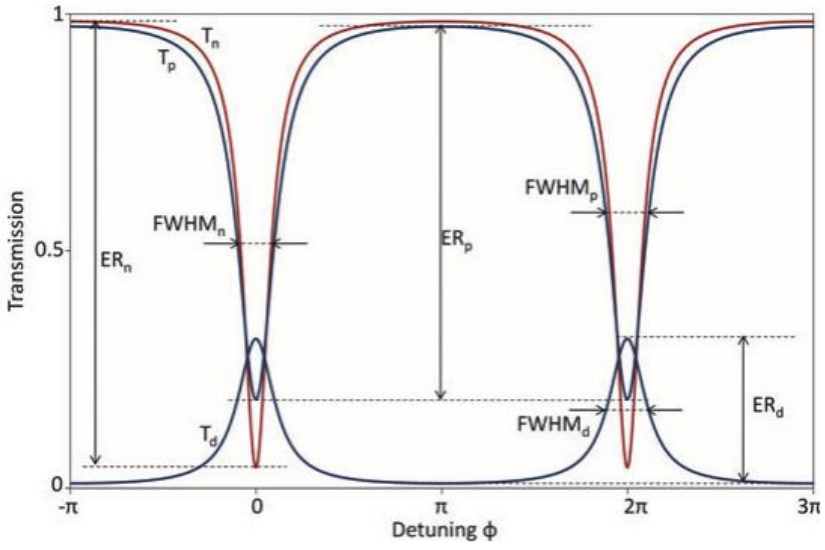

Figure 6.4: Transmission profile of a microring resonator [76]

From the above equations important spectral characteristics attributable to the ring resonator can be determined. These include the full width half maximum (FWHM) of the resonance peaks, the free spectral range (FSR) which is the spacing between resonances, and the quality factor (Q) of the resonator; these are all directly determined from Equation 6.25 above as well as the group index (n_g) of the waveguide,

$$n_g = n_{eff} - \lambda_0 \frac{\partial n_{eff}}{\partial \lambda_0} \tag{6.26}$$

$$FWHM = \frac{(1-ra)\lambda_{res}^2}{\pi n_g L \sqrt{ra}} \tag{6.27}$$

$$FSR = \frac{\lambda^2}{n_g L} \tag{6.28}$$

$$Q - factor = \frac{\lambda_{res}}{FWHM} \tag{6.29}$$

The quality factor of the microring resonator is a loose measure of the number of round trips made by the optical power in the ring waveguide before its energy is reduced to $1/e$ of its initial power; this can also be thought of as a measure of the "sharpness" of the resonance peaks with higher Q-factor resonances possessing a smaller FWHM [76].

When operated in an air clad geometry in the environment of an absorbing analyte any losses which occur due to power absorption of the evanescent field of the waveguide mode by the analyte molecules can be deduced directly from changes in the Q-factor of the microring. Using a Taylor expansion on the cosine term in Equation 6.24 allows the transmission power of the ring waveguide to be expressed in terms of directly measurable parameters. This is shown as follows [78]

$$\cos(\phi) = \cos\left(\frac{2\pi L n_{eff}}{\lambda}\right) = 1 - \frac{2\pi^2 L^2 {n_g}^2}{\lambda_0^4}(\lambda - \lambda_0)^2 \tag{6.30}$$

The total absorption coefficient, α_{total}, for the ring immersed in an analyte can also be written as

$$\alpha_{total} = \alpha_{waveguide} + \Gamma\alpha_{analyte} \tag{6.31}$$

Where $\alpha_{waveguide}$ is the intrinsic waveguide loss and $\alpha_{analyte}$ is the loss due to the analyte. Note that α_{total} can be related to the single pass amplitude of the ring, a, by $a = e^{-\alpha_{total}L/2}$ [77]. Γ is known as the interaction parameter of the waveguide and is a measure of how much optical power is propagating outside of the waveguide core and interacting with the analyte. It is given as

$$\Gamma = \frac{n_A \int_A |\boldsymbol{E}|^2 dA}{Z_o \int_\infty \mathrm{Re}\{\boldsymbol{E} \times \boldsymbol{H}^*\} \cdot \hat{z}\, dA} \tag{6.32}$$

Where **E** and **H** are the electric field and magnetic field of the waveguide mode and Z_0 is the impedance of free space.

The total quality factor of the ring resonator can be written in terms of the cavity quality factor, which is dependent on the intrinsic and coupling components of the cavity waveguides as well as the absolute quality factor which relates to the effective index of the waveguide as well as its interaction parameter and attenuation component. This can be written as follows [78].

$$\frac{1}{Q_{total}} = \frac{1}{Q_{cavity}} + \frac{1}{Q_{absolute}} \tag{6.33}$$

where,

$$\frac{1}{Q_{cavity}} = \frac{1}{Q_{intrinsic}} + \frac{1}{Q_{coupling}} \tag{6.34}$$

$$\frac{1}{Q_{absolute}} = \frac{\Gamma\alpha_{analyte}\lambda_0}{2\pi n_{eff}} \tag{6.35}$$

From Equation 6.35 the two most important metrics for ring resonators acting as a sensor are the interaction parameter and the quality factor. Naturally, these parameters are inverse to each other as a more tightly confined waveguide mode results in a higher quality factor cavity with less of its power residing in the evanescent portion of the mode.

7. Software Design and Optimization

7.1 Finite Difference Time Domain (FDTD) Solvers

A FDTD solver is an algorithmic software that solves Maxwell's equations for electric and magnetic field profiles both spatially and in the time domain. The solver algorithm breaks an otherwise complex geometric structure (such as a ring resonator) into smaller "cells" and solves these equations in a stepwise fashion. An optical source is modelled at a grid point (or plane) in the software which signifies the initial position and direction of the travelling electromagnetic wave (this could be a guided mode source in a waveguide or a free space beam, among others). The software then solves Maxwell's equations for the first grid cell which the source plane wave is incident upon in the geometry, stores the solutions in the space/time domain, and then "steps" to the next cell and repeats the process over the entire geometry of the system. The **E** and **H** fields are solved in a fully vectorial manner at different points in the cell and then interpolated to the origin of the cell [79]. This is shown in Figure 7.1.

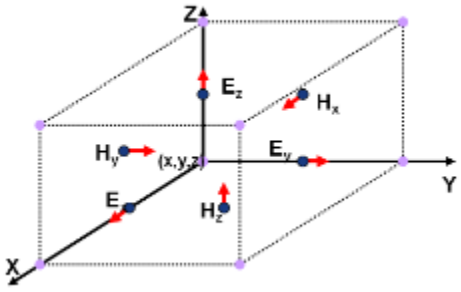

Figure 7.1 Single FDTD solver cell schematic [79]

The software incorporates numerous inputs from the user to accurately solve for the field profile inside of the cell, these include (but are not limited to): the refractive index of the material, dispersion coefficients, source power/position/frequency, external fields, boundary conditions).

The user can control the extent to which the geometry is discretized by setting the overall size of the cell (or a distribution of sizes based on geometric considerations); this is known as "meshing" the geometry. Setting a smaller mesh size results in a more accurate solution to Maxwell's equations, however this comes at a large computational cost in terms of the memory needed to carry out the computation and the associated time to converge on a solution. Most FDTD solvers have a library of meshing algorithms the user can implement to achieve an accurate solution based on the specific application, these include things such as varying geometric mesh types (rectangular, tetrahedral), mesh gradients (swept mesh, conformal mesh), and fully manual meshing modes. The user should choose the type of mesh based on the specifics of the system and conduct convergence testing (reducing mesh size until a stable solution is found) to ensure an accurate solution is achieved.

The software programs (COMSOL, Lumerical) used in this thesis to model waveguide modes, ring resonator spectra, and grating coupler efficiency use FDTD based solvers as described above.

7.2 Waveguide Mode Analysis

The COMSOL Multiphysics software suite was used to conduct a mode analysis for varying geometries of silicon-on-sapphire (SoS) waveguides and to calculate the resulting effective mode index of the waveguides in the 4280nm wavelength region. This analysis was carried out in the electromagnetic waves, frequency domain (ewfd) library in the wave optics module in the software. It solves for the effective mode of a 2-dimensional waveguide structure in the frequency domain.

The geometry of the SoS waveguide in COMSOL is shown below. This is modelled as a three-layer refractive structure with a silicon (*n=~3.42)* waveguiding core on top of a sapphire (*n=~1.87)* substrate. The waveguide is clad above and to the sides by air (*n=~1).* Materials are selected with a dispersive profile from the COMSOL materials library. The substrate and cladding regions are modelled with sufficient dimension such that the mode in the core (and outside) is not truncated by the boundaries of the simulation (this would result in an inaccurate calculation of the mode index). A total simulation region of 10,000 x 10,000nm was found to be sufficient for this purpose.

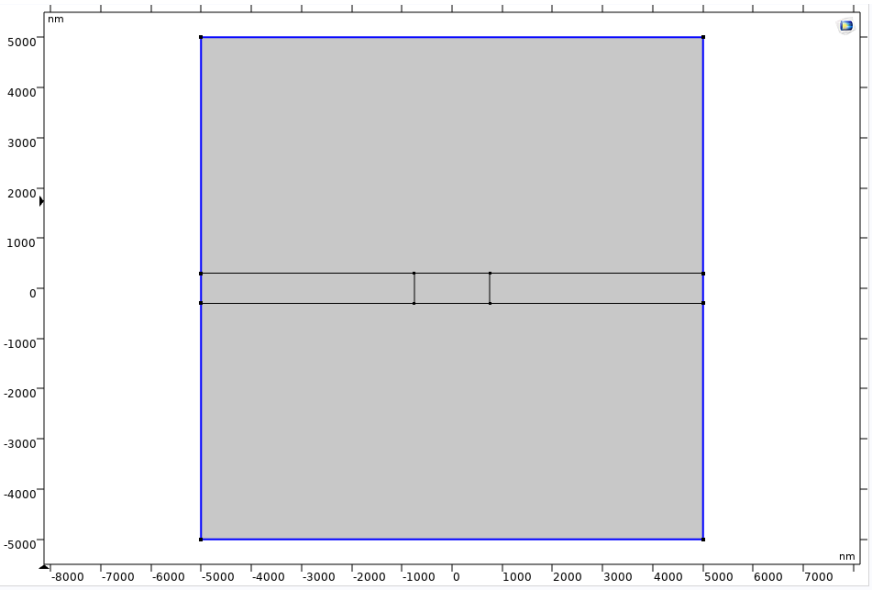

Figure 7.2: COMSOL Waveguide Simulation Geometry

As the waveguide mode is invariant in the axial direction of the waveguide (direction of propagation) the structure can be modelled in two-dimensions without loss of generality. This allows for a much finer meshing of the geometry due to the compression of the third dimension while maintaining low memory and time requirements for the resulting computation. While convergence testing was conducted for the 2D case here, it was quickly noticed that a sub-

nanometer mesh size was achievable which would result in a highly accurate solution for the fields over the grid (ultimately a minimum mesh size of 0.1 nm was used for the high refractive index core with a spatial growth rate of 1.01 moving away from the center). At this mesh size a single mode calculation takes approximately 37 seconds on an Intel i9 12-core workstation and requires ~2 gb of ram. The resulting mesh can be seen in the figure below.

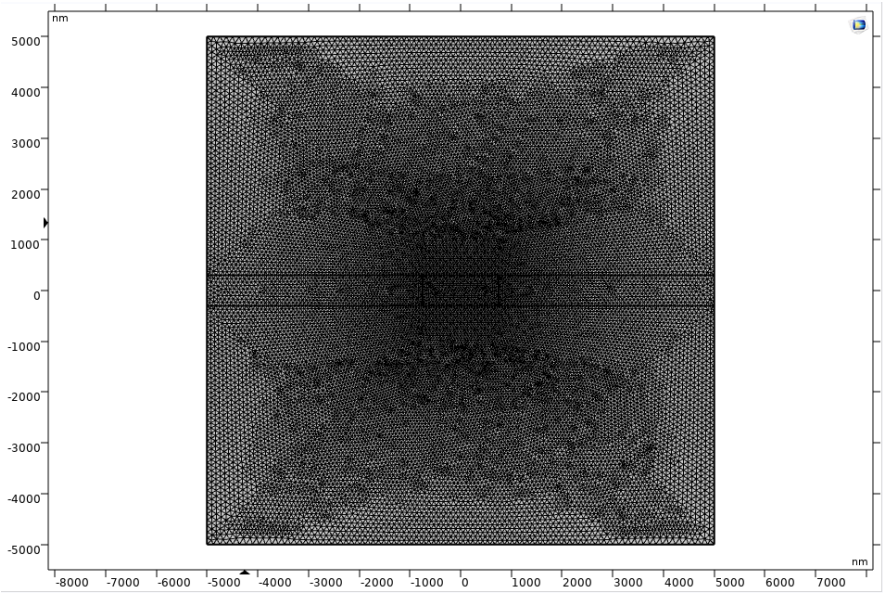

Figure 7.3: Fully Built Mesh of SoS Waveguide in COMSOL

For a 600 nm x 1500 nm waveguide geometry (h x w) one can simulate any number of desired modes and of any polarization. Below is a snapshot of the first TE mode for this chosen geometry. As can be seen below the fundamental mode has an effective mode index of 2.4058 which is well above the refractive index of both the air cladding and sapphire box, thus this mode is guided by Equation 6.10. Visually we see the bulk of the electric field distribution in the center of the waveguide with some power propagating at the sidewalls.

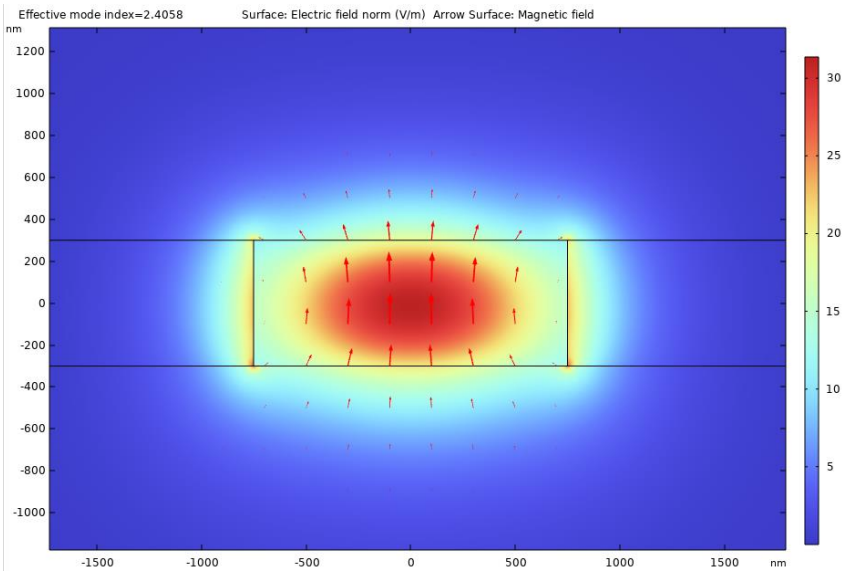

Figure 7.4: Mode profile of the fundamental TE mode of a 600nm x 1500nm SoS waveguide. Arrows indicate magnetic field direction.

COMSOL allows the user to perform parametric sweeps of any of the input parameters to calculate dispersive elements related to the waveguide. As the calculated modes of the waveguide depend on the geometry, wavelength, and material profile these can be varied to see how the effective mode index changes relative to these parameters. Figure 7.5 is a contour plot which shows the fundamental mode distribution for varying waveguide geometries at 4280 nm.

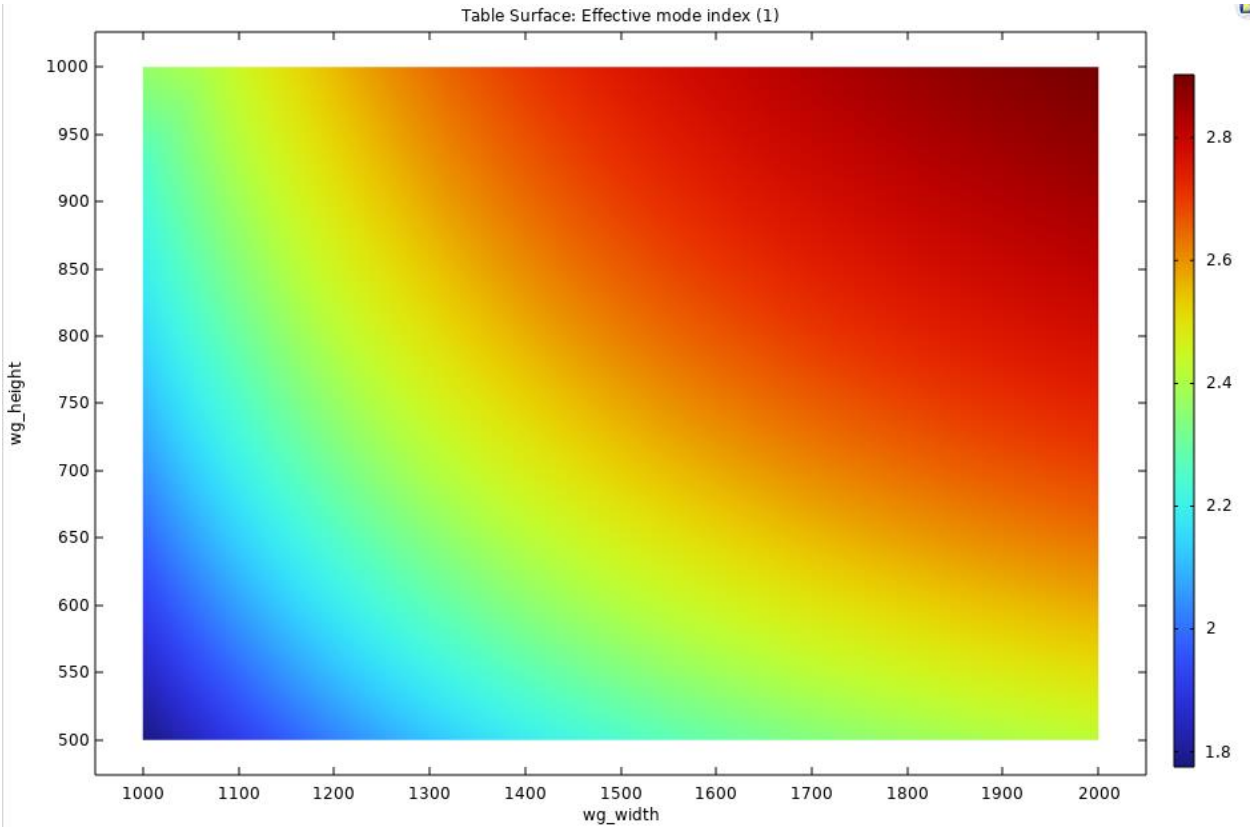

Figure 7.5: Effective mode index distribution for a SoS waveguide at 4280nm

From Figure 7.5 we can see that lower left region is the cutoff for the fundamental mode based on the guided mode condition of Equation 6.10. Effective indices below ~1.9 (that of sapphire) become lossy and radiative in the waveguide box and cladding. Increasing the waveguide height and width simultaneously results in a higher effective mode index for the waveguide which signifies greater containment of the mode in the silicon core.

For sensing purposes, one must explore the interaction parameter of the waveguide dimensions (the amount of electric field propagating in the top/side cladding analyte relative to the total power of the mode) as defined in Equation 6.32. COMSOL has spatial integration functionality built in which allows the user to assign domains of the geometry to an integration of calculated mode parameters, such as the electric field vector and Poynting vector. This surface

integration was carried out over varying waveguide geometries to determine which waveguide dimensions lead to the largest amount of waveguide power interacting with the surrounding waveguide cladding. Figure 7.6 is a contour plot of the interaction parameter as a function of waveguide dimension. As expected, larger waveguide dimensions result in a reduced interaction parameter as the mode is more tightly confined in the waveguide core. A similar measure of optical power interaction with the surrounding analyte cladding is that of the evanescent field ratio (EFR) which measures the total power (via the Poynting vector) in the cladding analyte rather than the norm of the elective field. A contour plot of the EFR for varying waveguide dimensions can be seen in Appendix E.

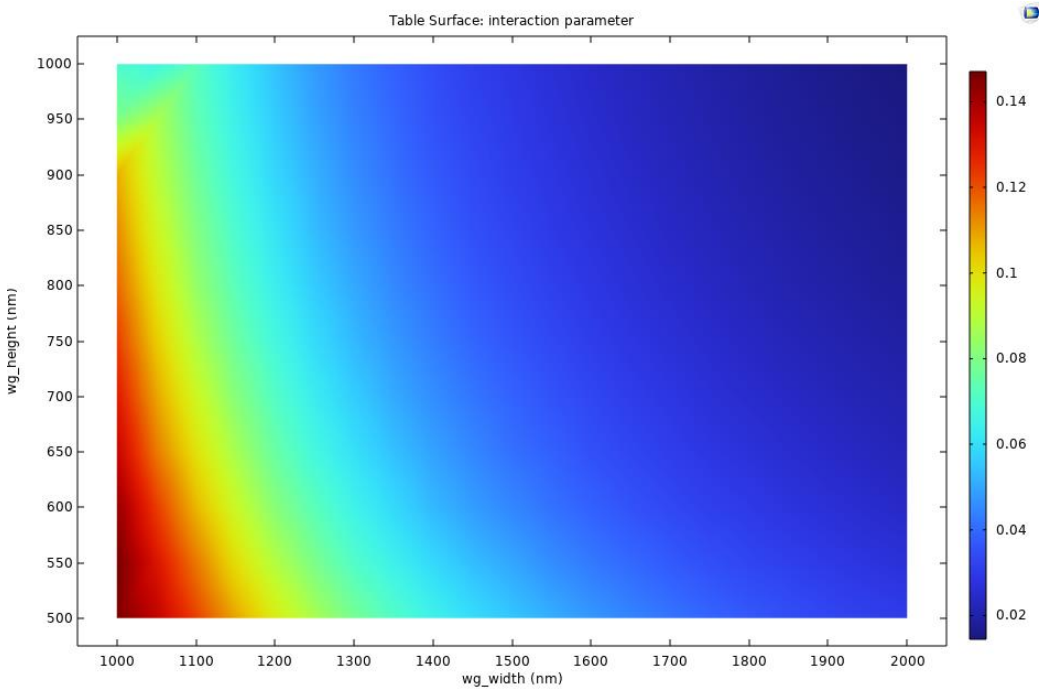

Figure 7.6: Interaction parameter (Γ) of SoS waveguide at 4280nm

It is also important to calculate the group index of the SoS waveguide as this parameter is directly used in the determination of the spectral profile generated by the ring resonator structure (Equations 6.27-6.29). COMSOL is not able to internally calculate this parameter as it lacks the

functionality to calculate the dispersion of the mode over a wavelength region. As such, a custom MATLAB script was written which takes the effective index output calculated by COMSOL over a wavelength region ($\Delta\lambda$) and fits it to a polynomial. The script then takes the derivative of this polynomial as per Equation 6.26 and calculates the group index. The effective index was fit to a 6^{th} order polynomial, but it's noted that there was no significant deviation in the group index from using a 2^{nd} order fit. Figure 7.7 shows the dispersive relation of the group index as a function of wavelength for a 600 nm x 1500 nm waveguide.

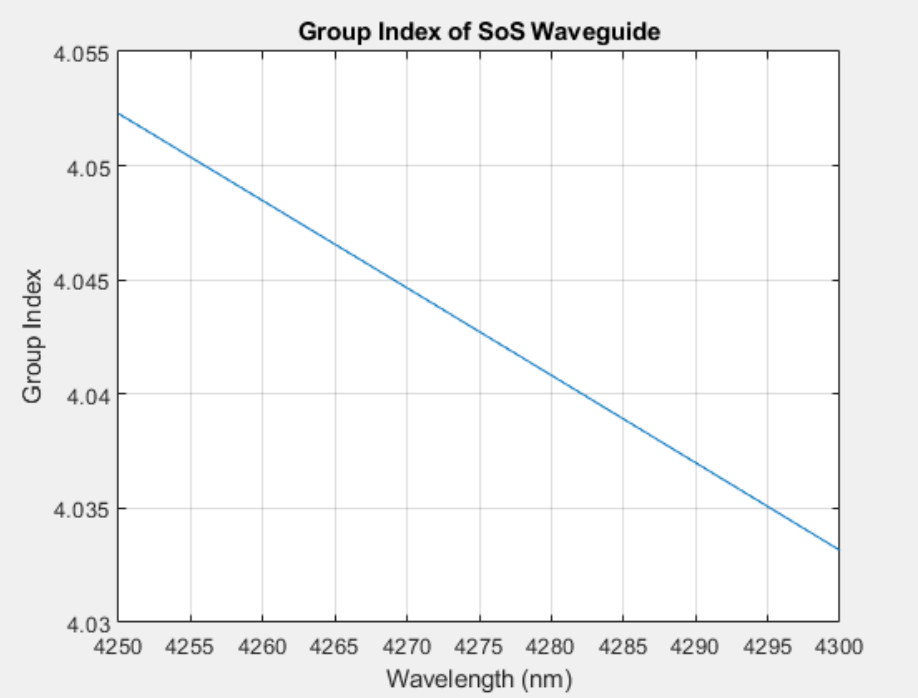

Figure 7.7: Group Index of 600 nm x 1500 nm SoS waveguide

7.3 Microring Resonator Analysis

COMSOL Multiphysics was also used to simulate the resonance spectrum for the ring resonator geometry described in Section 6.3. Due to geometric considerations of the three-layer waveguide system it is not possible to collapse the ring resonator design into a two-dimensional

structure as there is not a preferred spatial axis in which the cladding, core, and box layers reduce without loss of generality (eg. none of the three cartesian coordinate axes can be considered infinite). As such the structure was built using a three-dimensional layout in the software. Adding extra dimensions comes at a great cost in terms of computation time and memory resources, so efficient determination of proper mesh size to obtain a solution free of artifacts becomes a challenging exercise. For instance, by Equation 6.28, when combined with analysis done in Section 7.2, it can be determined that a ring with radius ~71 μm will result in a resonance profile with a FSR of ~10 nm. Increasing the ring radius to as high as ~300 μm will reduce the FSR further to nearly ~2 nm. These ring sizes constitute optically large structures in terms of the software used to model them as the entire geometry needs to be solved in terms of Maxwell's equations to obtain the resulting **E** and **H** fields both spatially and in time. COMSOL uses a solver called the *Electromagnetic Waves, Beam Envelopes (ewbe)* interface to handle such optically large systems. This interface separates the phase and field amplitude solutions for the varying electromagnetic fields over the domain to reduce computational resources. A complete explanation of the algorithms behind this interface can be found in [80].

Geometry of the modelled ring resonator structure is shown in Figure 7.8.

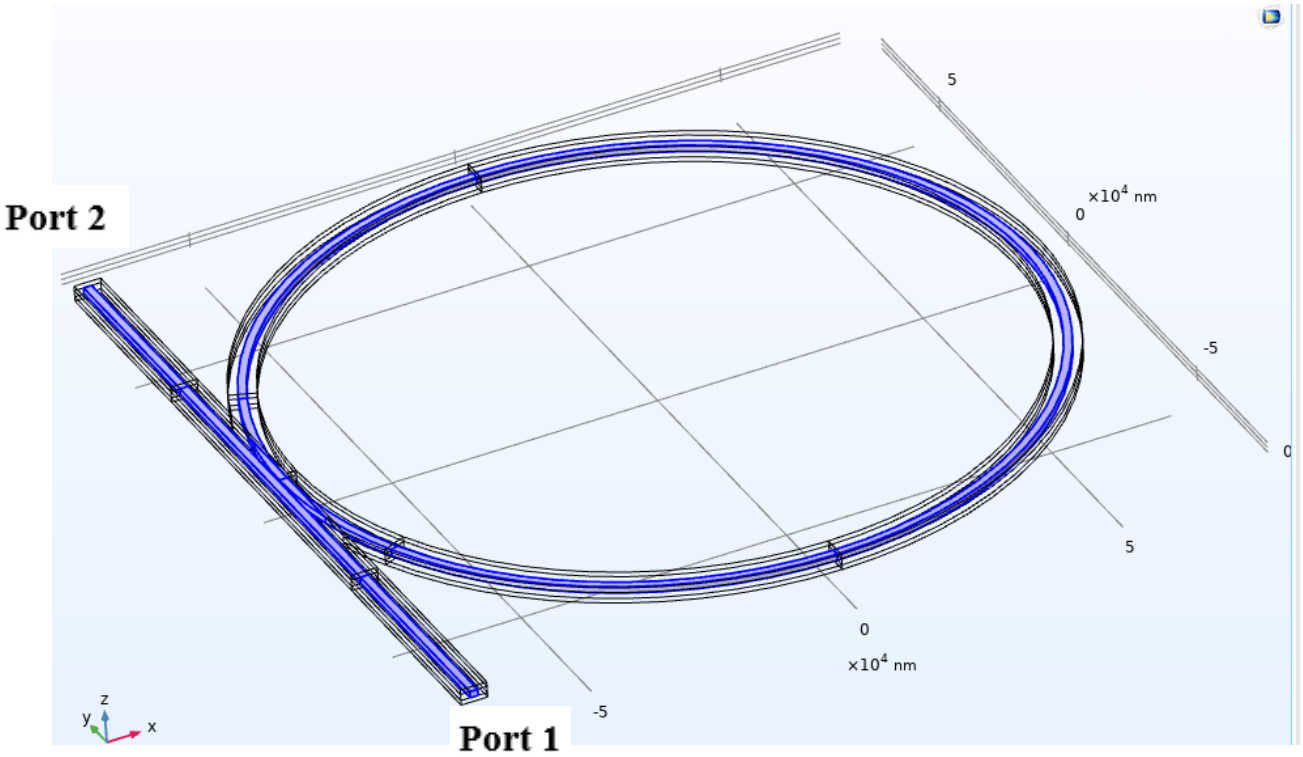

Figure 7.8: COMSOL layout of 3D ring resonator with 70 µm ring radius. Blue elements constitute the silicon core of the structure. Note to save on computational resources the simulation is restricted to a 10,000nm square cladding around the waveguide core

Materials for the ring resonator are assigned in the same manner as described for the waveguide mode analysis. Meshing requirements for the 3D resonator structure required much trial and error to land on a suitable solution given the size of the domain (approximately 80 µm x 80 µm). Given the large size of the geometry it was not feasible to complete true convergence testing in which mesh size was systematically reduced for each element of the geometry (evaluation of the ring transmission at a single wavelength takes ~37 minutes on the workstation previously mentioned). Rather a swept mesh algorithm from COMSOL was used in which smaller mesh elements were assigned to high refractive index sections of the geometry (eg. silicon core components). The mesh size was left as a free parameter which was then varied via a parametric

sweep. The fundamental mode of the straight waveguide in the 3D model was then calculated at different mesh sizes and compared against that calculated in Section 7.2. Results of this comparison showed that a minimum mesh element of ~180 nm in the silicon core allowed for an accurate calculation of the propagating fundamental TE mode. Cladding and box mesh sizes were assigned a growth rate of 1.01 as in the 2D waveguide mode analysis.

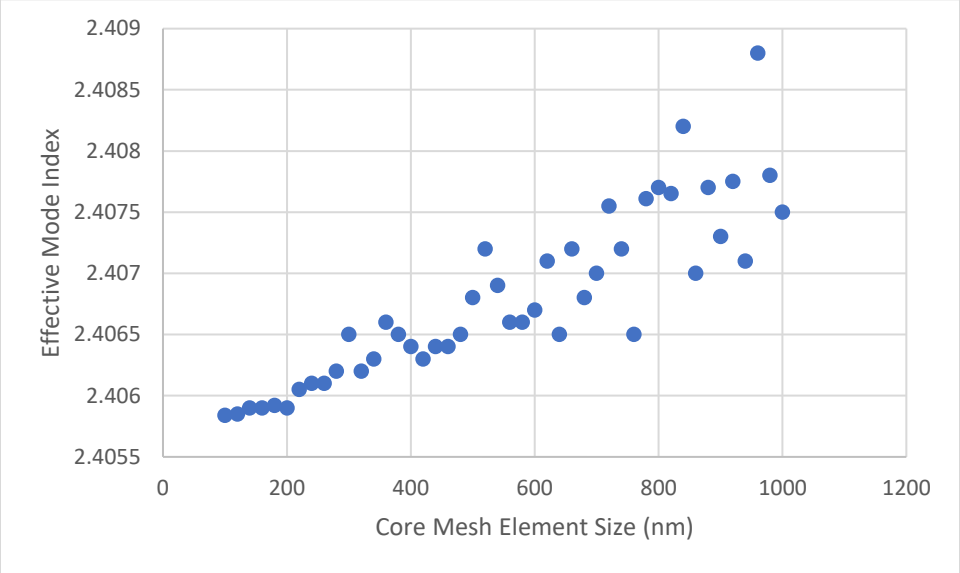

Figure 7.9: Effective index of fundamental mode of 600nm x 1500nm SoS waveguide as a function of core mesh size in three dimensions

To simulate the travelling wave inside of the straight waveguide and ring the ends of the straight waveguide are modelled as "ports" in COMSOL. One port (Port 1) launches the fundamental mode of the waveguide geometry, and the other port (Port 2) collects the information of the travelling wave after it has traversed the ring and coupled back into the straight waveguide. As the travelling electromagnetic wave moves through both the straight waveguide and the ring it accumulates a single pass phase shift induced by the optical length of the ring, which was previously discussed as $\phi = \beta L$. This phase must be modelled in COMSOL so that the software

properly calculates the interference of the waves in the straight waveguide and the ring waveguide in the coupling region (*k* in Figure 6.3). As per COMSOL documentation, for straight and bent waveguides this phase shift is modelled as follows

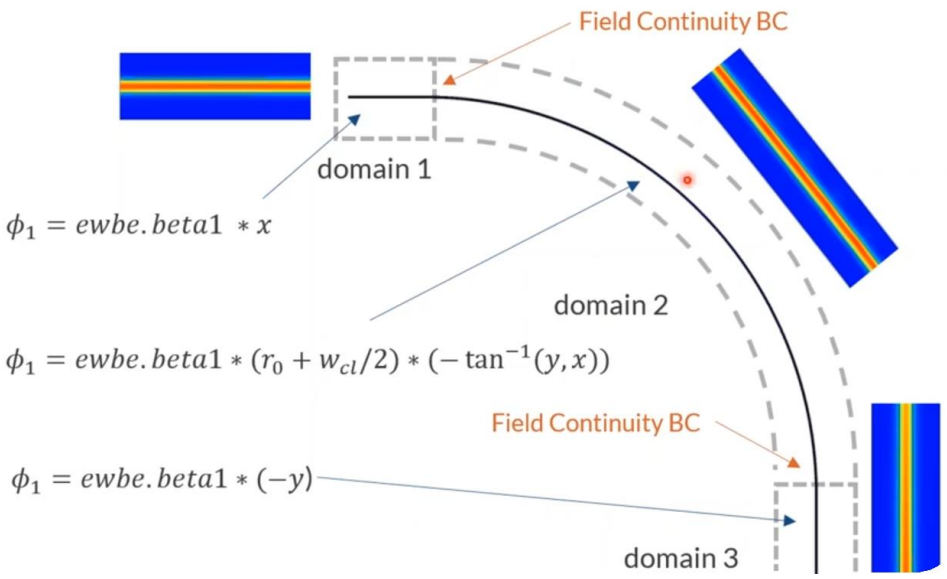

Figure 7.10: Phase elements for straight and bent waveguides in COMSOL [81]. W_{cl} signifies the width of the simulation region around the waveguide core

From Figure 7.10 we can see that for straight waveguide elements the propagation constant ($\beta = ewbe.beta\_1$) varies linearly in straight portions of the waveguide and via the inverse tangent of the carteisan coordinates in bent portions. Adjacent geometries are connected via a *Field Continuity* in the software which is a 2D plane in the geometry that separates the phase boundaries.

From the calculations of the waveguide modes at the two ports COMSOL generates a reflectance and transmittance plot which shows the resonance spectrum of the ring under study as a function of wavelength. Figure 7.11 shows the resonance spectrum for a 600 nm x 1500 nm SoS waveguide, 70 μm ring radius, and 200 nm coupling gap.

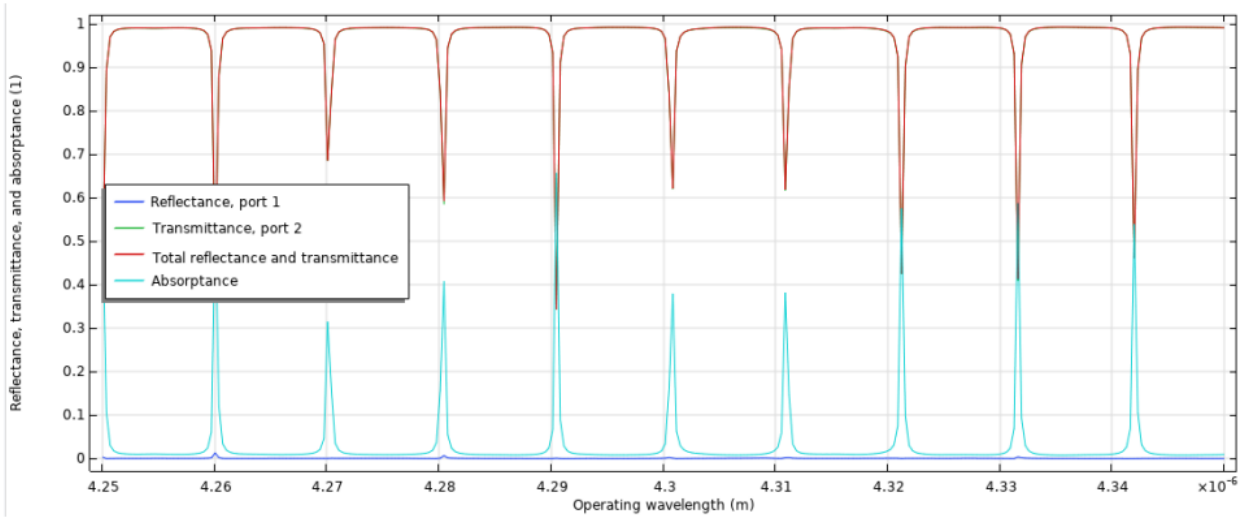

Figure 7.11: Resonance spectrum of 600 nm x 1500 nm SoS ring resonator with 70 µm radius and 200 nm coupling gap

The spectrum in Figure 7.11 above appropriately shows an FSR of approximately 10 nm and a Q-factor of ~51,000 for the sharpest resonances.

7.4 Grating Coupler Analysis

Grating coupler analysis and optimization was carried out in the Ansys Lumerical Software suite. This is another FDTD based solver like COMSOL but is specifically designed to model photonic optical systems. While grating couplers could be modelled in COMSOL much in the same fashion as they are described here, Lumerical offers some advantages in terms of ease of modelling optical sources such as its built in fully vectoral solvers for focusing lenses, which are discussed here.

Example files from Lumerical [84] were used as a base for the design and optimization of the grating couplers in this thesis. Gratings can initially be optimized in two dimensions as the axis parallel to the grating teeth can be considered infinite and collapsed without loss of generality to

the solution (which is the power coupled into a waveguide along the orthogonal axis to the gratings). A snapshot of the initial two-dimensional model in Lumerical can be seen in Figure 7.12.

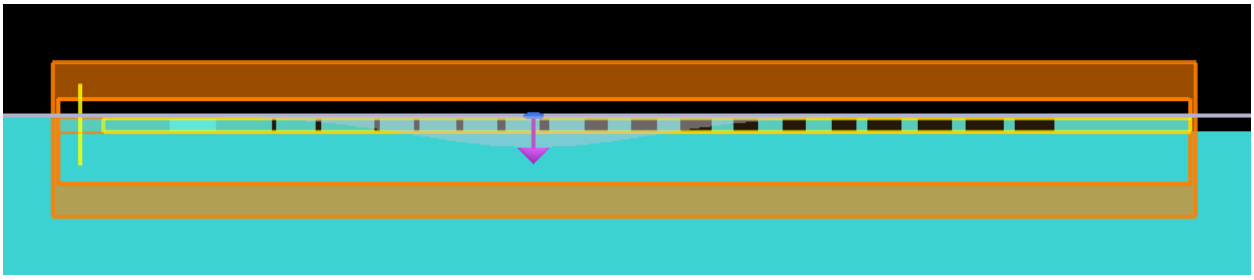

Figure 7.12: 2D grating coupler in Lumerical

In Figure 7.12 the grating teeth (alternating blue/black region) can be seen underneath a Gaussian source (purple arrow). The simulation region is encased in a perfectly match layers (PML) boundary which "absorbs" transient fields in the simulation, so propagation of the fields extends to an infinite distance rather than reflecting into the simulated domain (see Appendix F for a brief discussion on boundary conditions in FDTD solvers). On the left the vertical yellow line signifies a mode monitor which calculates the effective index of the attached waveguide as well as power transmission from the gratings. Material properties are individually assigned for the layers of the silicon slab waveguide (blue with yellow border), air cladding (black), and sapphire box (blue).

As previously mentioned, the methodology introduced by Marchetti *et al.* [74] was used in the optimization of the gratings here. This optimization is run through a Python interface in Lumerical's Design Toolbox (lumopt). Example files are provided by Lumerical [84] for both the two-dimensional and three-dimensional optimization and were extensively modified to incorporate the specifics of the SoS wafer material and the optical parameters of the OPO source.

The optical source was modelled to match the specifications of the Aculight Argos OPO Module D which operates in the 4.3 μm region. In Lumerical the optical source was modelled as

a *Gaussian Beam* of diameter ~3.3 mm (used with a 5x beam expander) incident upon a 25.4 mm 0.25 NA focusing lens (this was done using the *Thin Lens* approximation in Lumerical [82]). Output from the lens hits the gratings at normal incidence at the focal point of the lens.

As discussed in Section 6.3, the optimization requires four inputs, $\{x_0, R, a, B\}$, where x_0 is the starting location of the first grating tooth, R is the fill factor apodization, $a = n_{eff2} - n_{eff1} sin\theta_c$ and $b = \Delta n$. With a normally incident beam the a and b parameters take on the same value and are easily approximated using the waveguide mode analysis from Part II Section 3.1. The first grating tooth was chosen to start at an arbitrary x-position in the simulation domain such that 20 gratings could be fit into the simulation region comfortably (as it was easily estimated at least this many gratings would be needed to accommodate the spot size of the focused beam). The initial apodization factor was chosen to be 30 nm as per [74] with an initial fill factor of 0.95.

The lumpot toolbox in Lumerical runs a minimization algorithm to optimize the figure of merit (FOM) in the grating analysis. In this case the FOM is the coupling efficiency into and out of the gratings. For an input coupler the geometry in Figure 7.12 yields a negative directional value for the input power into the waveguide which is then minimized to obtain strong coupling (the negative sign is purely directional; coupling efficiency is given as the absolute value of this parameter). The software uses the Broyden-Fletcher-Goldfarb-Shanno (L-BFGS) algorithm to vary the grating parameters over a series of iterations until the FOM is optimized by means of steering the gradient evolution of the parameters towards a minimal value. Specifics of the L-BFGS algorithm can be found in [83]. Output from the optimization for an input grating is shown in Figure 7.13.

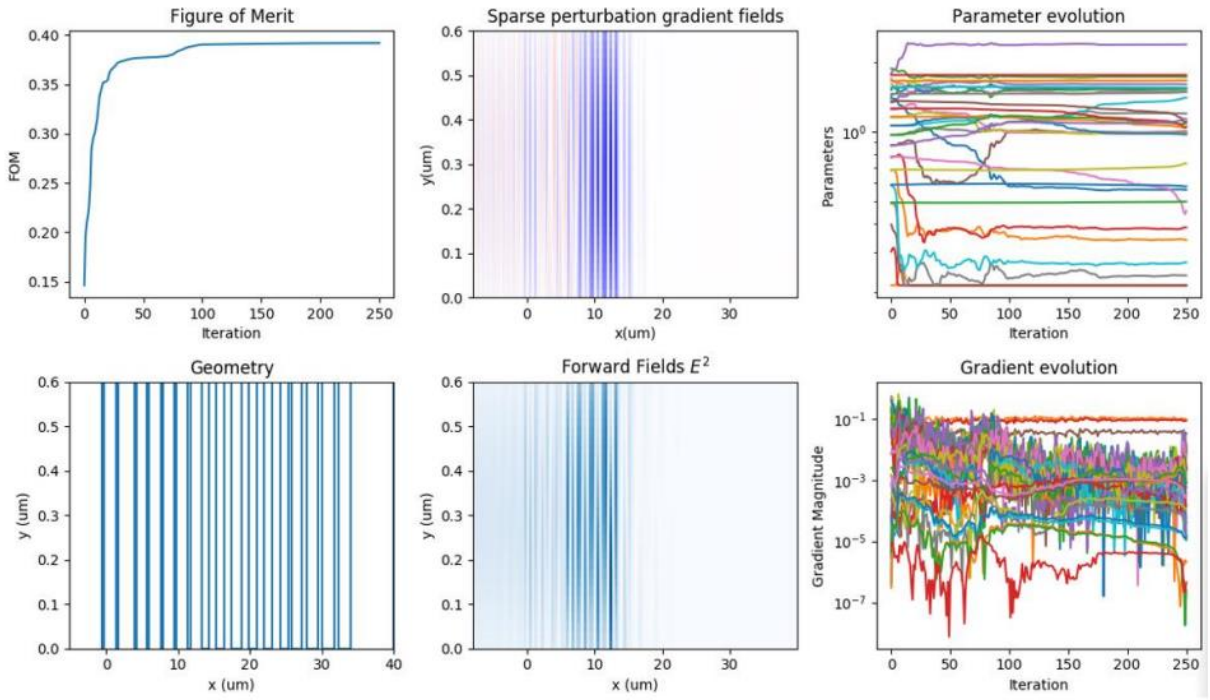

Figure 7.13: 2D grating optimization parameter evolution for a 600nm thick SoS waveguide and vertically incident OPO source

As can be seen from Figure 7.13 after roughly 50 iterations of parameter evolution the optimization achieves an input coupling efficiency of nearly 40%. Field profiles (**E**) as well as the resulting geometry and gradient of the input parameters are also tracked over the simulation.

The grating positions from the optimized two-dimensional model are used as inputs for a three-dimensional model based on example files from Lumerical [84]. The three-dimensional model uses a focusing grating design to reduce the footprint of the gratings. This design curves the gratings by an opening angle given by the formula [85]

$$n_{eff} - \frac{m\lambda}{\rho_m} = \cos(\Upsilon)\sin(\theta) \tag{7.1}$$

Where n_{eff} is the effective grating index, m is the integer number of individual gratings, λ is the wavelength of light incident on the gratin, ρ_m is the distance coordinate of the mth grating and ϒ and θ are the opening angle of the curved grating and input light coupling angle respectively. Figure 7.14 shows these parameters

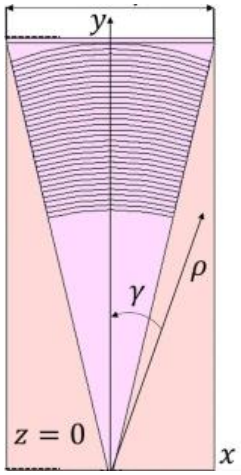

Figure 7.14: Curved grating schematic [85]

The curved grating design is then optimized further to determine the optimal starting position of the first grating relative to the optical source position as well as the optimal opening angle for the curved grating. For the geometry demonstrated here the optimal opening angle is determined to be 31.3° resulting an input transmission for the grating of 39%, nearly identical to the two-dimensional case. Figure 7.15 shows the optimized 3D structure and coupling efficiency.

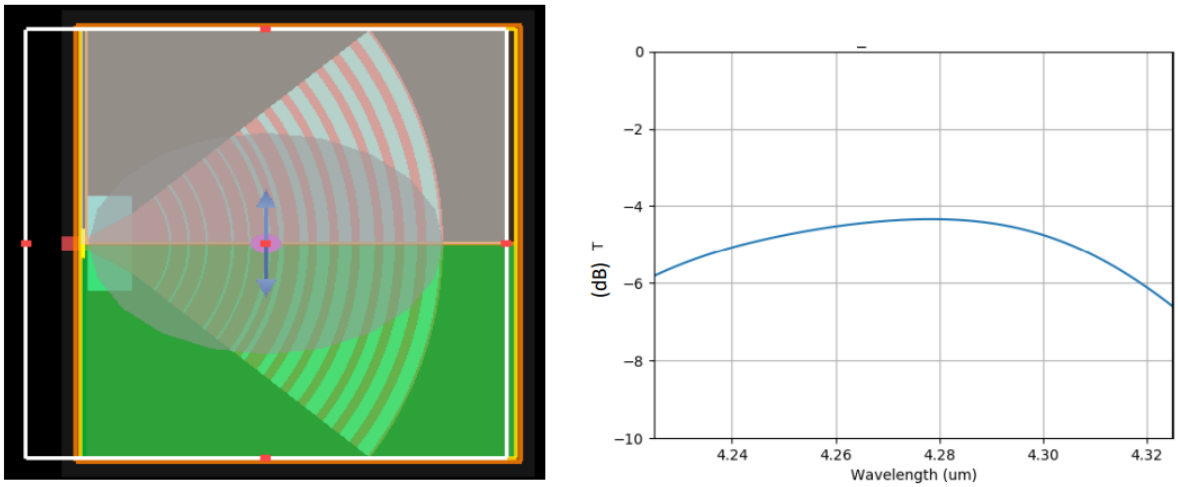

Figure 7.15: Optimized 3D SoS grating coupler and source position for a 600nm thick Si layer connecting to a 1500nm wide waveguide. Input transmission efficiency of the grating coupler is ~39%.

A similar optimization is also run in reverse to assess the out-coupling transmission of the gratings in which the fundamental mode of the SoS waveguide is diffracted into free space for collection. The optimization is run in the same manner with only two minor differences. Firstly, the optical source is now modelled as the fundamental mode of the 600 nm x 1500 nm waveguide, this is done by setting a *mode source* in the Lumerical software. A *power monitor* is used above the gratings to calculate the diffracted power from the gratings. This is shown in Figure 7.16 below.

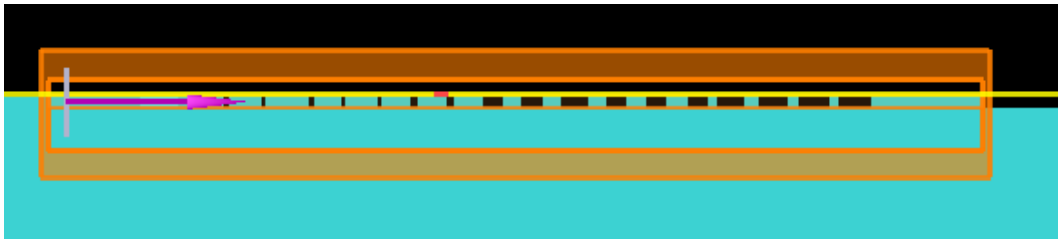

Figure 7.16: Output grating schematic from Lumerical. Purple arrow signifies the mode source, bright yellow line above gratings indicates power monitor

The optimization results for the output grating are shown below achieving a similar coupling efficiency for light diffracted at perfectly normal incidence.

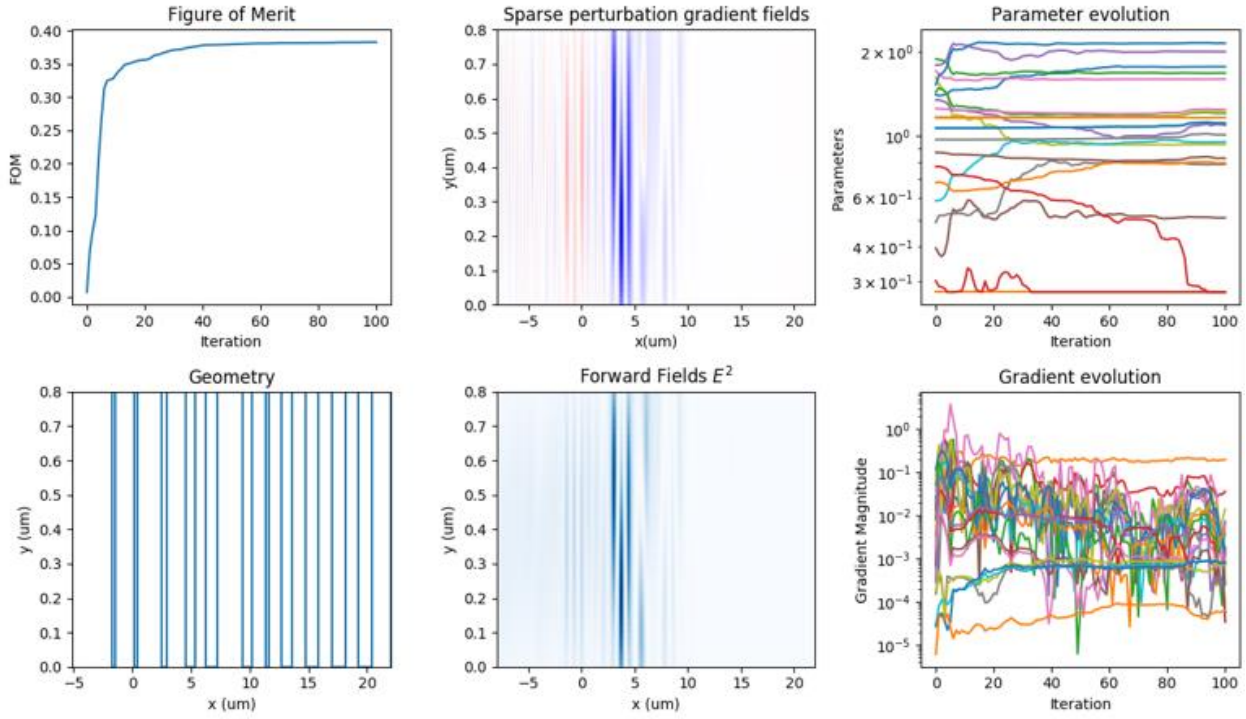

Figure 7.17: 2D grating optimization parameter evolution for a 600nm thick SoS waveguide and vertical out-coupling to free space

7.5 Mask Layout Creation

Once the optical structures have been optimized the resulting geometries must be bought to a file type suitable for patterning by means of an Electron Beam Lithography machine. These machines used a CAD based design environment to pattern photonic structures into wafer material. The file type used for standardized CAD design is GDSII. While Lumerical can directly export structures from the FDTD solver to GDSII unfortunately COMSOL does not have this functionality built in. To work around this limitation a custom Python script was written which draws the straight and bent waveguide structures to a grid and grabs and pastes the optimized

grating structures from Lumerical accordingly. This was done with the help of the GDSHelpers Python library add-on [86] which is a design environment for lithography patterning. A total of 100 grating coupled ring resonator structures of varying dimensions (ring radii, coupling gaps, waveguide widths) were written to a 9mm x 9mm chip grid suitable for patterning; this is known as a mask layout. A section of the chip grid is shown in Figure 7.18. KLayout software is an open source GDSII viewer/editor which was also used in this process to view the output of the Python script.

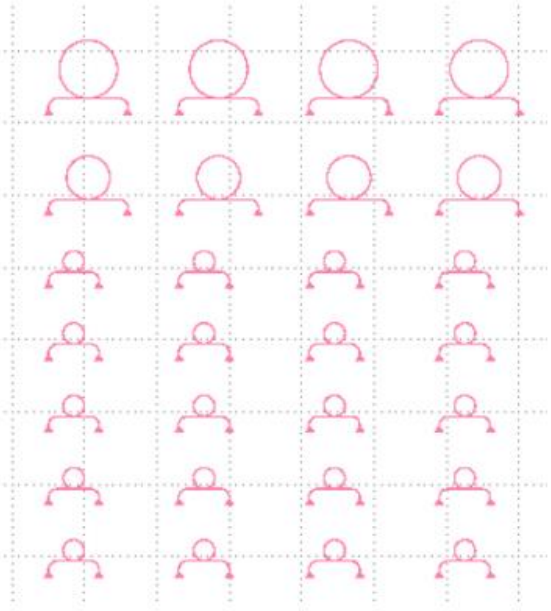

Figure 7.18: Section of a 9 mm x 9 mm mask layout for the optimized ring resonator structures shown in KLayout

8. Manufacture

The mask layout was patterned by a company called Applied Nanotools (ANT) located at the University of Alberta. A SoS wafer comprising a 600 nm thick Si layer atop a 460 μm sapphire layer was sourced from University Wafer. A 600 nm Si layer wafer was ultimately chosen due to

patterning considerations provided by ANT. These considerations placed limitations on the minimum size of design features and the etch depth which would ultimately be possible by the lithography machine the company uses. A full list of design limitations is as follows for the 600 nm thick Si wafer

- 200 nm minimum feature size
- ±25 nm feature bias (eg. location of any feature, such as a grating wall, may vary by 25 nm)
- Only fully etched geometries possible due to electron beam marker limitations in the sapphire substrate

The above design limitations were included in the optimized structures to ensure they would meet patterning requirements from the lithography machine. After a lengthy process to calibrate the lithography machine to accommodate the SoS wafer, the resulting 9 mm x 9 mm chip was patterned with good resolution. Figure 8.1 shows scanning electron microscope (SEM) images of the patterned devices.

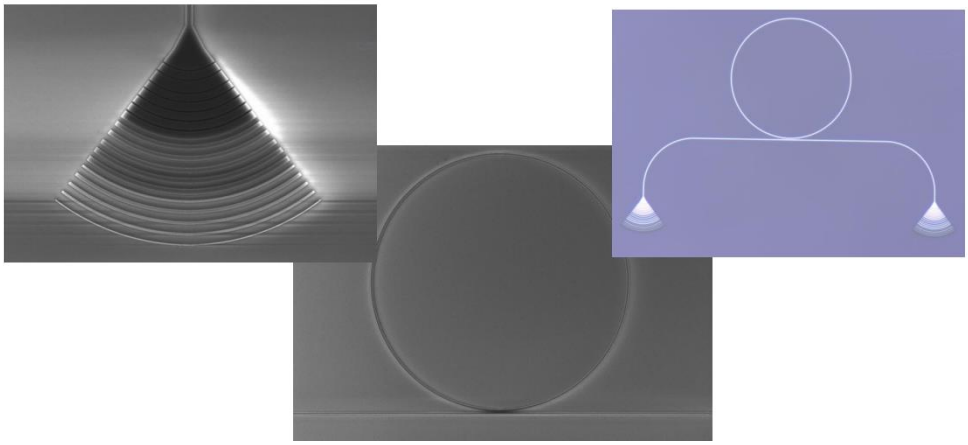

Figure 8.1: SEM imaging of patterned SoS ring resonator and grating structures from Applied Nanotools

9. Experimental Design

An experimental optical table setup has been built to ultimately characterize the performance of the patterned SoS ring resonator and grating devices. A schematic of the experimental setup is shown below.

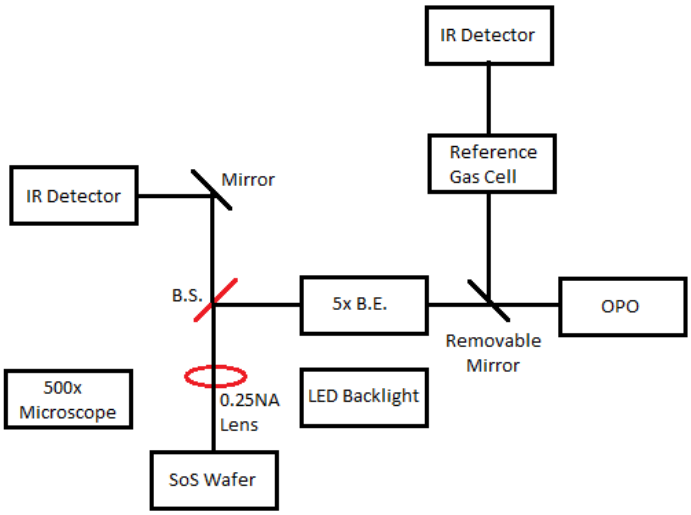

Figure 9.1: Experimental Setup for Wafer Characterization

Mid infrared light from the OPO source is passed through a 5x beam expander (B.E.) and a 50:50 beam splitter (B.S.) before being focused onto the SoS wafer by a 0.25NA calcium fluoride lens with a back focal length of ~5 cm at 4000 nm operating wavelength. Output from the wafer is collimated by the same lens and passed through the same beam splitter towards an LN_2 cooled mid-IR detector. A removable mirror can be placed in front of the OPO source to pass the signal through a reference CO_2 gas cell and into another IR detector for wavelength measurement. Coarse imaging of the input beam on the wafer is provided by a 500x digital microscope which is backlit by a flexible LED. Beam placement on the input grating of the nanodevices is aided by a visible,

500-700 nm, portion of the input beam which is a by-product of the down conversion process in the OPO. All optical components are mounted individually on manually adjustable x,y,z-translation stages for fine alignment. The entire setup is mounted on a vibration isolation table and encased in a custom-built polycarbonate box attached to a MERV 13 air filtration system to minimize dust accumulation on the nanometer sized features of the wafer. The box will also ultimately serve as a controlled gas environment for testing the nanodevices as trace gas sensors for CO_2 and was manufactured with ¼" gas line fittings. For explanation of the individual experimental instruments refer to Part I, Section 3 of this thesis.

10. Discussion and Conclusion

10.1 CO_2-Kr Isotopic analysis

The observed vibrational shift of the CO_2-^{84}Kr band origin relative to the free CO_2 monomer is -0.885 cm^{-1}, indicating a red shift in frequency relative to the free monomer for the CO_2 ν_3 fundamental vibration. This indicates an overall increase in strength of the intermolecular interaction (the strength of the van der Waals force) upon excitation of the vibrational mode. Likewise, the band origin shift for the i-p and o-p bending modes were very similar to the fundamental with values of -0.886 cm^{-1} and -0.876 cm^{-1} respectively indicating the same increase in interaction strength. The determination of the intermolecular bend frequency of 29.429 cm^{-1} falls in-line with previously determined values for the bend frequencies of other CO_2-Rg complexes that is an increase in the bend frequency with increasing atomic mass of the Rg atom. As well, the determination of the splitting between the degenerate bending modes of the CO_2 ν_2 vibration, determined here as 1.418 cm^{-1}, follows the same trend. Table 10.1 shows a comparison of the intermolecular bending frequencies and CO_2 ν_2 splittings for the CO_2-Rg family of complexes.

Table 10.1: Intermolecular bending frequencies and CO_2 ν_3 splitting values for CO_2 containing dimers

	Intermolecular bend	CO_2 ν_2 splitting
CO_2-He [12]	~8.3 (theoretical)	
CO_2-Ne [13]	17.716	0.057
CO_2-Ar [14]	27.818	0.877
CO_2-Kr	29.429	1.418
CO_2-Xe [15]	30.574	2.14
CO_2-N_2 [46]	21.379	2.307
CO_2-CO [47]	24.51	4.566
CO_2-OC [47]	14.372	1.586
Units are in cm^{-1}.		

It is clear that the isotopic mass of the Kr atom in the complex plays a role in both line broadening and splitting, but this phenomenon is only distinguishable in the intermolecular bending region in this analysis. A similar splitting is occurring in both the fundamental and hot band regions (this can be seen in the blended lines simulated in PGOPHER), however, due to the placement of the Kr atom along the *a*-inertial axis of the molecule these splittings are within the resolution of the spectrometer. Regardless, the method of parametrization for the rotational constants and band origin shift used in this analysis result in rms errors an order of magnitude smaller than the experimental line width, which indicates a satisfactory simulation of the splittings in the intermolecular bending region and the blending of lines in the other regions studied in this work.

10.2 water-CO_2 Tunnelling Analysis

By virtue of the symmetry of the ground and excited vibrational states of the CO_2-water complexes (where water = H_2O, D_2O or HDO) only k_a = even energy levels are populated for the lower internal rotation tunneling states and only k_a = odd energy levels are populated for the upper tunnelling states. This allows for the simultaneous assignment of spectral transitions to separate subbands based on the value of the ground state k_a parameter and thus allows for the determination of the magnitude of the tunnelling component of energy level splitting. Direct determination of the tunnelling component is dependent on the upper state vibrational symmetry and thus can only be computed in certain cases as allowed by rovibronic transitions that connect differing tunnelling states; alternate symmetries yield values for either the sum or difference in ground and excited state tunnelling values. Figure 10.1 below illustrates the transition pathways for various excited state (ν_1, ν_2, ν_3) fundamental vibrations for either H_2O or CO_2 in the water-CO_2 complexes.

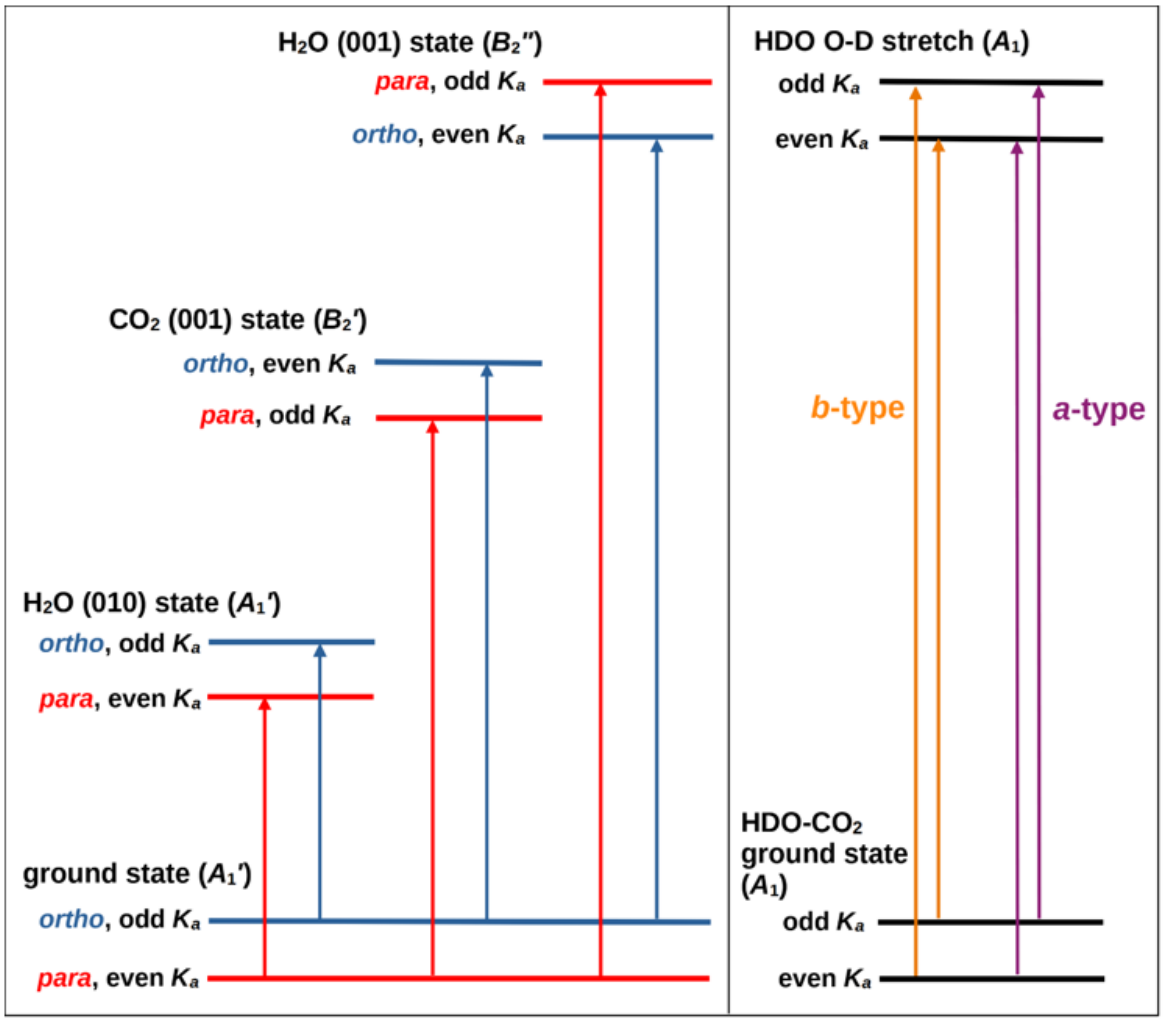

Figure 10.1: Illustration of allowed infrared transitions among tunneling components for different infrared bands of H_2O-CO_2 (left) and HDO-CO_2 (right). D_2O-CO_2 is just the same as H_2O-CO_2, except that the para and ortho labels are interchanged. Vibrational symmetry labels (A_1', etc.) refer to the G_8 (MS) group for H_2O-CO_2 or the G_4 (MS) group for HDO-CO_2.

As can be seen from the left panel in Figure 10.1, due to the symmetry of the excited state vibration, the difference in band origin from the ground vibrational state to the (010) bending vibration of H_2O and the (001) asymmetric stretch vibration of CO_2 are equal to the difference in

ground and excited state tunnelling splittings. The (001) asymmetric stretch vibration of water has an upper state symmetry such that the difference in band origins results in a value of the sum of ground and excited state splittings. These sums and differences (as calculated in this thesis) between ground (S'') and excited (S') state tunnelling splittings are shown in Table 10.2 along with relevant literature values.

Table 10.2: Observed band origin separations, $\Delta\nu_0$, for infrared bands of water-CO_2 complexes (in cm^{-1})

	upper state	$\Delta\nu_0$	splitting sum or difference	reference
CO_2-H_2O	H_2O (010)	0.007	S''-S'	[48]
	CO_2 (001)	-0.0016	S''-S'	present work
	H_2O (001)	0.2681	S''+S'	[22]
	H_2O (200)	0.0168	S''-S'	[25]
	H_2O (101)	0.1948	S''+S'	[25]
CO_2-D_2O	D_2O (010)	0.0004	S''-S'	[48]
	CO_2 (001)	0.0002	S''-S'	present work
	D_2O (011)	0.0058	S''+S'	present work
S'' and S' denote ground and excited state tunnelling splittings respectively				

For the HDO containing isotopomer the spin weight distinction no longer applies and there is no longer a possible interchange of the H or D molecules in the water unit of the complex. The result is a molecule of reduced symmetry (G_4) that can be simulated by means of four separate transitions with four independent band origins. Simulation of these four bands allows for the separate assignment of ground and excited tunneling splittings, rather than deriving them from the sum of the ground and excited states as is the case with D_2O. These upper and lower state splittings are shown in Table 10.3 along with literature values.

Table 10.3: Ground (S'') and excited (S') state tunnelling splittings for water-CO_2 complexes from the fundamental O-H or O-D stretching region (in cm^{-1})

	S''+S'	S''	S'	S'' calculated [27]
CO_2-H_2O [22]	0.2681	0.1356	0.1325	0.1447
CO_2-HDO [present work]	0.0465	0.02344	0.0231	
CO_2-D_2O [present work]	0.0058	0.0029	0.0029	0.0039
For CO_2-D_2O we assume S''= S'				

For the HDO containing complex the ground and excited state tunnelling splittings are determined independently thanks to the reduced symmetry of the molecule. For the D_2O complex in the O-D stretch region we operate under the assumption that the magnitude of the tunnelling splittings are relatively independent of the vibrational mode of the molecule, at least for the case of intramolecular fundamental vibrations. This allows us to split the band origin difference to arrive at values for the ground and excited state splittings. As can be seen from table 5.3 our calculated value of the ground state splitting for CO_2-D_2O agrees well with that calculated by Felker *et al*. [27]. To the best of our knowledge this is the first experimental determination of this splitting value. The same can be said for the HDO complex; this is the first time the splitting value for the ground and excited state has been directly determined and there is currently no theoretical work on HDO containing CO_2-water. It would be worthwhile to develop the theoretical calculations for this complex to see if they fall in line with the experimentally determined values produced here.

Lastly, we can consider the vibrational shifts of the water-CO_2 molecules relative to the vibrational frequencies of the free H_2O or CO_2 monomers in the regions under study. These shifts are given in Table 10.4 below.

Table 10.4. Vibrational shifts for water-CO_2 complexes (in cm^{-1})

	H_2O (010)	CO_2 (001)	H_2O (001)	H_2O (200)	H_2O (101)
CO_2-H_2O[a]	-2.2	3	-3.2		
CO_2-H_2O	0.739[b]	1.159[c]	-3.02[d]	-6.134[e]	-2.824[e]
CO_2-HDO			-2.282[c, f]		
CO_2-D_2O	0.083[b]	1.169[c]	-1.485[c]		

[a][49]; [b][48]; [c]present work; [d][22]; [e][25]; [f]this is the O-D stretch of HDO

From Table 10.4 we see that the H_2O bend and CO_2 asymmetric stretch vibrations are all blue shifted from the free monomers by small amounts while the O-H and O-D stretching vibrations are red shifted. An interesting observation is that the CO_2-HDO shift in the O-D stretch region is nearly midway between those of CO_2-H_2O and CO_2-D_2O in their asymmetric stretching regions even though the nature of the HDO vibration is, in a sense, a mixture of the H_2O and D_2O (100) and (001) modes. It is unknown why the theoretical predictions for the vibrational band shifts in the H_2O complex as reported by [49] are quite a bit higher than those experimentally determined, and in the case of the H_2O (010) vibration, differ in sign. Perhaps this is due to some sort of vibrational mixing of the various excited fundamental modes due to tunnelling, but this is yet to be determined.

10.3 FDTD Analysis of Grating Coupler SoS Ring Resonators

FDTD simulation of the various optical components of the grating coupled ring resonator structures yields coupling efficiencies for the input/output gratings of nearly 40% for vertically incident free space radiation and a cavity quality factor of ~51,000 for a 600 nm x 1500 nm SoS waveguide with 71μm ring radius and 200 nm coupling gap. One hundred separate sensor devices of varying configurations (waveguide widths, ring radii, gap dimensions) were patterned on a 9

mm x 9 mm SoS wafer with the hopes of experimentally characterizing the varying geometric effects of the device on Q-factor and interaction parameter performance as well as any manufacturing bias. Optimal device configurations, once experimentally determined, will be used to probe the free CO_2 monomer in the region of the ν_3 fundamental stretch (~2350 cm^{-1}) through an overlap in ring resonance placement and known CO_2 absorption peaks.

Attempts at device characterization in the laboratory are ongoing. Project delays related to wafer manufacturing, equipment procurement, and multiple failures of critical components of the mid-IR OPO source in the spectroscopy lab at the University of Calgary have thus far rendered device characterization incomplete. Initial attempts to obtain a signal from the patterned devices were met with experimental challenges including unwanted optical reflections of the OPO source from the wafer surface as well as input alignment imaging issues related to the off-axis orientation of the 500x digital microscope. Some of these issues have been rectified via iterative improvements to the experimental setup (eg. backlighting the digital microscope) but the challenge of obtaining signal throughput from the devices remains. Ongoing work will include patterning a second wafer in which the orientation of the output grating is orthogonal to the input thereby allowing a polarizer to be placed before the collection detector to eliminate unwanted reflections from the substrate boundaries (both reflected light from the substrate and diffracted light from the grating maintain their original polarization). Patterning devices with butt coupling output will also be carried out on the same wafer to further diversify the possible collection methodology and address any unwanted reflections. Figure 10.2 shows the additional device configurations that will be patterned and tested as next steps for the project.

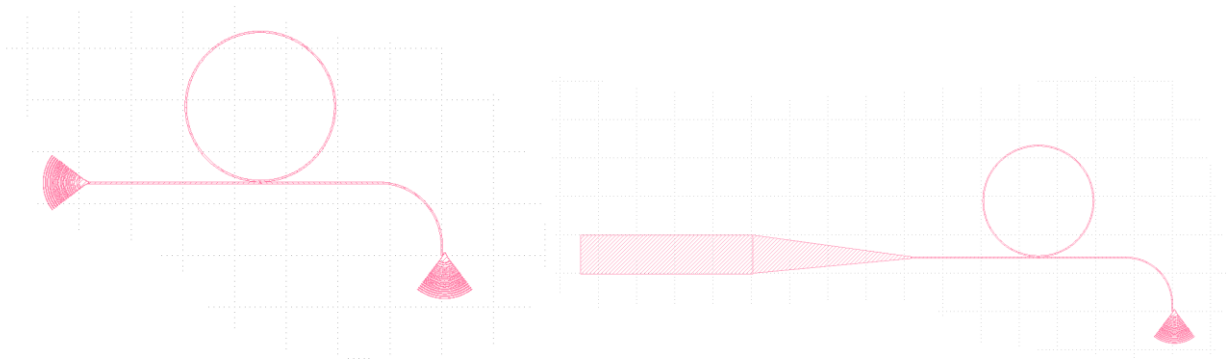

Figure 10.2: Additional resonator/grating device configurations. Left: device with output orthogonal to input. Right: device with tapered output butt coupling

10.4 Conclusions

This thesis has presented new and improved high resolution infrared spectra of CO_2 containing van der Waals complexes in the 3.5-4.3 μm region via a supersonic jet expansion. Spectra of the CO_2-Kr complex is reported in the region of the CO_2 ν_3 fundamental vibration with improved accuracy from previously reported literature values. This complex is also studied in the region of the intermolecular combination band with the first experimentally determined value for the frequency of the intermolecular bend reported as 29.49 cm^{-1}. Lastly CO_2-Kr spectra is reported in the region of the hot band originating in the state of the degenerate intramolecular bend of the CO_2 monomer. Reported is the first experimentally determined value for the splitting between the in-plane and out-of-plane bend of CO_2 due to the Kr atom of 1.418 cm^{-1}; this is in line with the splittings determined for other CO_2-Rg complexes. Good simulation of the spectra is achieved by scaling the molecular rotational constants and band origins to reflect broadening and splitting of transitions due to changes in the isotopic mass of the Kr atom.

High resolution infrared spectra of water-CO_2 complexes are reported with a consideration for splitting of energy states due to internal rotation of the water and CO_2 monomers around the

van der Waals bond. Spectra is reported in the region of the CO_2 ν_3 fundamental vibration for the H_2O and D_2O containing complexes where the difference in tunnelling splittings of the ground and excited vibrational state are experimentally determined. The D_2O containing complex is further studied in the region of the D_2O ν_3 fundamental where symmetry considerations yield the first experimental determination of the ground state internal rotation tunnelling splittings of 0.003 cm^{-1}. Lastly spectra of the HDO containing complex is recorded in the region of the O-D stretching vibration which yields the first direct experimental determination for the ground state tunnelling spltting of 0.0234 cm^{-1}.

A finite difference time domain study is presented which optimizes a grating coupled silicon-on-sapphire microring resonator to probe the same CO_2 ν_3 fundamental vibration which is studied for the CO_2-Kr and water-CO_2 complexes in this thesis. This optimization determines the effective mode distribution of SoS wavguides capable of single mode propagation near 2350 cm^{-1}. Optimized structures include fully etched SoS grating couplers capable of ~40% input/output efficiency and microring cavities with Q-factors as high as ~51,000. These devices, when experimentally characterized and further optimized will present the first step in a drastic reduction in both the size and power requirement of the traditional laboratory spectrometer needed to record such spectra as presented in this thesis. Development of such micrometer sized sensors based on silicon photonics platforms represent the first step in mid-infrared “lab-on-a-chip” sensing solutions.

References

[1] Marlow, H., “Derivation of aerosol collision rates for singular attractive contact potentials”, *The Journal of Chemical Physics,* vol. 73 (12), 1980

[2] Roth, C., Neal, B., Lenhoff, A., “Van der Waals interactions involving proteins”, *Biophysical Journal,* vol. 70 (2), 1996

[3] Hult, E., Kiejna, A., “Trends in atom/molecule-surface van der Waals interactions”, *Surface Science,* vol. 383 (1), 1997

[4] van der Waals, J., “On the Continuity of the Gaseous and Liquid States”, *University Leiden (Doctoral Dissertation),* 1873

[5] Keesom, W., “The second virial coefficient for rigid spherical molecules whose mutual attraction is equivalent to that of a quadruplet placed at its center”, *Proceedings of the Royal Netherlands Academy of Arts and Sciences,* vol. 18, 1915

[6] Debye, P., “van der Waals Cohesive Forces”, *Physikalische Zeitschrift,* vol. 21, 1920

[7] London, F., “On the Theory and Systematics of Molecular Forces”, *Zeitschrift fur Physik A Hadrons Niclei,* vol. 63, 1930

[8] Jones, J., “On the determination of molecular fields I. From the variation of the viscosity of a gas with temperature”, *Proceedings of the Royal Society of London. Series A, Containing Papers of a Mathematical and Physical Character,* vol. 106, 1924

[9] Steed, J., Dixon, T., Klemperer, W., “Determination of the structure of $ArCO_2$ by radio frequency and microwave spectroscopy”, *Journal of Chemical Physics,* vol. 70 (4095), 1979

[10] Randall, R., Walsh, M., Howard, B., “Infrared absorption spectroscopy of rare-gas-CO_2 clusters produced in supersonic expansions”, *Faraday Discussions of the Chemical Society,* vol. 85, 1988

[11] Chen, M., Zhu, H., “Potential energy surface, microwave and infrared spectra of the Xe-CO_2 complex from ab initio calculations”, *Journal of Theoretical and Computational Chemistry,* vol. 11 (03), 2021

[12] Ran, H., Xie, D., “A new potential energy surface and predicted infrared spectra of He-CO_2: Dependence on the antisymmetric stretch of CO_2”, *Journal of Chemical Physics,* vol. 128 (12), 2008

[13] Barclay, A., McKellar, A., Moazzen-Ahmadi, N., “New infrared spectra of CO_2-Ne: Fundamental for CO_2-^{22}Ne isotopologue, intermolecular bend, and symmetry breaking of the intramolecular CO_2 bend”, *Chemical Physics Letters,* vol. 779, 2021

[14] Gartner, T., Barclay, A., McKellar, A., Moazzen-Ahmadi, N., “Symmetry breaking of the bending mode of CO_2 in the presence of Ar”, *Physical Chemistry Chemical Physics,* vol. 37, 2020

[15] Barclay, A., McKellar, A., Western, C., Moazzen-Ahmadi, N., “New infrared spectra of CO_2-Xe: modelling Xe isotope effects, intermolecular bend and stretch, and symmetry breaking of the CO_2 bend”, *Molecular Physics,* vol. 119 (11), 2021

[16] Barclay, A., McKellar, A., Moazzen-Ahmadi, N., “Infrared spectra of $(CO_2)_2$-Rg timers, Rg=Ne, Ar, Kr, and Xe”, *Journal of Molecular Spectroscopy,* vol. 387, 2022

[17] Barclay, A., McKellar, A., Moazzen-Ahmadi, N., "Spectra of CO_2-Rg_2 and CO_2-Rg-He trimers (Rg=Ne, Ar, Kr, and Xe): Intermolecular CO_2 rock, vibrational shifts and three-body effects", *Journal of Chemical Physics,* vol. 157 (20), 2022

[18] Fraser, G., Pine, A., Suenram, R., "Optothermal-infrared and pulsed-nozzle Fourier-transform microwave spectroscopy of rare gas-CO_2 complexes", *Journal of Chemical Physics,* vol. 88, 1988

[19] Iida, Y., Endo, Y., "Induced dipole moments and intermolecular force fields of rare gas-CO_2 complexes studied by fourier-transform microwave spectroscopy", *Journal of Chemical Physics,* vol. 97, 1993

[20] Konno, T., Fukuda, S., Ozaki, Y., "Infrared spectroscopy of Kr-$^{12}C^{18}O_2$: Change in the CO_2 intramolecular potential by complex formation and isotope effect on the vibrationally averaged intermolecular geometry", *Chemical Physics Letters,* vol. 414 (4:6), 2005

[21] Peterson, K., Klemperer, W., "Structure and internal rotation of H_2O-CO_2, HDO-CO_2, and D_2O-CO_2 van der Waals complexes", *Journal of Chemical Physics,* vol. 80, 1984

[22] Block, P., Marshall, M., Pedersen, L., Miller, R., "Wide amplitude motion in the water-carbon dioxide and water-acetylene complexes", *Journal of Chemical Physics,* vol. 96, 1992

[23] Columberg, G., Bauder, A., Heineking, N., Stahl, W., Makarewicz, J., "Internal rotation and hyperfine structure in the rotational spectrum of a water-carbon dioxide complex", *Molecular Physics,* vol. 93(2), 1998

[24] Lauzin, C., Imbreckx, A., Foldes, T., Vanfleteren, T., Moazzen-Ahmadi, N., Herman, M., "High-resolution spectroscopic study of the H_2O-CO_2 van der Waals complex in the 2OH overtone range", *Molecular Physics,* vol. 118(11), 2020

[25] Bogomolov, A., Roucou, A., Bejjani, R., Herman, M., Moazzen-Ahmadi, N., Lauzin, C., "The rotationally resolved symmetric 2OH excitation in H_2O-CO_2 observed using pulsed supersonic expansion and CW-CRDS", *Chemical Physics Letters,* vol. 774, 2021

[26] Andersen, J., Heimdal, J., Mahler, D., Nelander, B., Wugt Larsen, R., "Communication: THz absorption spectrum of the CO_2H_2O complex: Observation and assignment of intermolecular van der Waals vibrations", *Journal of Chemical Physics,* vol. 140, 2014

[27] Felker, P., Bacic, Z., "Intermolecular rovibrational states of the H_2O-CO_2 and D_2O-CO_2 van der Waals complexes, *Journal of Chemical Physics,* vol. 156, 2022

[28] Bunker, P., Jensen, P., *Molecular Symmetry and Spectroscopy Second Edition,* NRC Research Press, 2006

[29] Bernath, P., *Spectra of Atoms and Molecules,* Oxford, NY: Oxford University Press, 1995

[30] Baba, M., Kanaoka, A., Tohyama, H., Katori, T., Kunishige, S., Nishiyama, A., Misono, M., "Coriolis interaction of small and large aromatic hydrocarbons", *Journal of Molecular Spectroscopy,* vol. 360, 2019

[31] Teller, E., *Hand- und Jahrbuch der Chemischen Physik*, vol. 9, 1934

[32] J. Hougen, "Energies of, and Transition Intensities Associated with, the Rotational Levels of Nearly Degenerate A1A2 Pairs of Vibronic States in Molecules of Symmetry C3v", *Journal of Chemical Physics*, vol. 38, 1963

[33] Boyd, D., Longuet-Higgins, H., “Coriolis interaction between vibration and rotation in symmetric top molecules”, *Proceedings of the Royal Society of London. Series A, Mathematical and Physical Sciences,* vol. 213, 1952

[34] di Lauro, C., *Rotational Structure in Molecular Infrared Spectra*, Elsevier Inc, 2013

[35] Wang, S., “On the asymmetrical top in quantum mechanics”, *Physical Review,* vol. 34(243), 1929

[36] Bauder, A., Mathier, E., Meyer, R., Ribeaud, M., Gunthard, H., “Theory of rotation and torsion spectra for a semi-rigid model of molecules with an internal rotor of C_{2v} symmetry”, *Molecular Physics,* vol. 15(6), 1968

[37] Tinkham, M., *Group Theory and Quantum Mechanics*, McGraw-Hill/Dover Publications Inc., New York, 1964

[38] Kantrowitz, A., Grey, J., “A High Intensity Source for the Molecular Beam. Part I. Theoretical”, *Review of Scientific Instruments,* vol. 22(5), 1951

[39] Demtroder, W., *Laser Spectroscopy: Basic Concepts and Instrumentation”,* Springer, Germany, 2003

[40] Hagena, O., “Nucleation and growth of clusters in expanding nozzle flows”, *Surface Science,* vol. 106(1:3), 1981

[41] Morrison, A., Liang, T., Douberly, G., “Automation of an “Aculight” continuous-wave optical parametric oscillator”, *Review of Scientific Instruments*, vol. 84, 2013

[42] Hevenith, M., *The Molecular Beam: Infrared Spectroscopy of Molecular Clusters*, Springer-Verlag, Berlin, 2002

[43] Western, C., *PGOPHER version 10.1*, University of Bristol Research, 2018, http://pgopher.chm.bris.ac.uk/

[44] Gartner, T., Ghebretnsae, S., McKellar, A., Moazzen-Ahmadi, N., "Spectra of CO_2-Kr in the 4.3 μm region: Intermolecular Bend and Symmetry Breaking of the Intramolecular CO_2 Bend", *Chemistry Select*, vol. 7(36), 2022

[45] Chen, R., Zhu, H., "Intermolecular potential energy surface, microwave and infrared spectra of the Kr-CO_2 complex from ab initio calculations", *Chemical Physics Letters*, vol. 511(4:6), 2011

[46] Barclay, A., McKellar, A., Moazzen-Ahmadi, N., "Spectra of CO_2-N_2 dimer in the 4.2um region: Symmetry breaking of the intramolecular CO_2 bend, the intermolecular bend, and higher K-values for the fundamental", *Journal of Chemical Physics*, vol. 153, 2020

[47] Wakwella, P., McKellar, A., Moazzen-Ahmadi, N., "Infrared spectra of both isomers of CO_2CO in the CO_2 ν_3 region", *Molecular Physics*, vol. 119(12), 2021

[48] Zhu, Y., Li, S., Sun, P., Duan, C., "Infrared diode laser spectroscopy of H_2O-CO_2 and D_2O-CO_2 complexes in the ν_2 bend region of water", *Journal of Molecular Spectroscopy*, vol. 283, 2013

[49] Makarewicz, J., "Intermolecular potential energy surface of the water-carbon dioxide complex", *Journal of Chemical Physics*, vol. 132, (2010)

[50] Gaeta, A., Lipson, M., Kippenberg, T., "Photonic-chip-based frequency combs", *Nature Photonics*, vol. 13, 2019

[51] Ciminelli, C., Dell'Olio, F., Conteduca, D., Armenise, M., "Silicon photonic biosensors", *IET Optoelectronics,* vol. 13(2), 2019

[52] Tombez, L., Zhang, E., Orcutt, J., Kamlapurkar, S., Green, W., "Methane absorption spectroscopy on a silicon photonic chip", *Optica,* vol. 4(11), 2017

[53] Shi, Y., Zhang, Y., Wan, Y., Yu, Y., Zhang, Y., Hu, X., Xiao, X., Xu, H., Zhang, L., Pan, B., "Silicon photonics for high-capacity data communications", *Photonics Research,* vol. 10(9), 2022

[54] Strechinsky, M., Ding, R., Liu, Y., Novack, A., Galland, C., Lim, J., Lo, Q., Baehr-Jones, T., Hochberg, M., "The road to affordable, large-scale silicon photonics", *Optica Photonics,* vol. 24(9), 2013

[55] Soref, R., "Mid-infrared photonics in silicon and germanium", *Nature Photonics,* vol. 4, 2010

[56] Vainio, M., Halonen, L., "Mid-infrared optical parametric oscillators and frequency combs for molecular spectroscopy", *Physical Chemistry Chemical Physics,* vol. 6, 2016

[57] Chang, T., Chen, Y., Luo, D., Li, J., Chen, P., Lee, S., Fang, Z., Li, W., Zhang, Y., Li, M., Majumdar, A., Liu, C., "Black Phosphorous Mid-Infrared Light-Emitting Diodes Integrated with Silicon Photonic Waveguides", *Nano Letters,* vol. 20(9), 2020

[58] Lin, H., Luo, Z., Gu, T., Kimerling, L., Wada, K., Agarwal, A., Hu, J., "Mid-infraed integrated photonics on silicon: a perspective", *Nanophotonics,* vol. 7(2), 2017

[59] Baehr-Jones, T., Spott, A., Ilic, R., Penkov, B., Asher, W., Hochberg, M., "Silicon-on-sapphire integrated waveguides for the mid-infrared", *Optics Express,* vol. 18(12), 2010

[60] Li, F., Jackson, S., Grillet, C., Magi, E., “Low propagation loss silicon-on-sapphire waveguides for the mid-infrared”, *Optics Express,* vol. 19(16), 2011

[61] Huang, Y., Salih, K., Qiancheng, Z., Torun, R., Ozdal, B., “Silicon-on-sapphire waveguides design for mid-IR evanescent field absorption gas sensors”, *Optics Communications,* vol. 313, 2014

[62] Lui, Y., Spott, A., Beahr-Jones, T., Ilic, R., Hochberg, M., “Silicon waveguides and ring resonators at 5.5um”, *7th IEEE International Conference on Group IV Photonics,* 2010

[63] Shankar, R., Bulu, I., Loncar, M., “Integrated high-quality factor silicon-on-sapphire resonators for mid-infrared applications”, *Applied Physics Letters,* vol. 102, 2013

[64] Smith, C., Shankar, R., Laderer, M., Frisch, M., Loncar, M., Allen, M., “Sensing nitrous oxide with QCL-coupled silicon-on-sapphire ring resonators”, *Optics Express,* vol. 23(5), 2015

[65] Smith, C., Shankar, R., Laderer, M., Frisch, M., Loncar, M., Allen, M., “Sensing nitrous oxide with QCL-coupled silicon-on-sapphire ring resonators”, *Optics Express,* vol. 23(5), 2015

[66] Miller, S., Yu, M., Ji, X., Griffith, A., Cardenas, J., Gaeta, A., Lipson, M., “Low-loss silicon platform for broadband mid-infrared photonics”, *Optica,* vol. 4(7), 2017

[67] Xiao, T., Zhao, Z., Zhou, W., Chang, C., “Mid-infrared high-Q germanium microring resonator”, *Optics Letters,* vol. 43(12), 2018

[68] Osman, A., Nedeljkovic, M., Penades, S., “Suspended low-loss germanium waveguides for the longwave infrared”, *Optics Letters,* vol. 43,(24), 2018

[69] Ranacher, C., Consani, C., Tortschanoff, A., Jannesari, R., “Mid-infrared absorption gas sensing using a silicon strip waveguide”, *Sensors and Actuators A: Physical,* vol. 277, 2018

[70] Su, P., Kita, Z., Lin, P., Deckoff-Jones, S., “Monolithic on-chip mid-IR methane gas sensor with waveguide-integrated detector”, *Applied Physics Letters,* vol. 114, 2019

[71] Cheng, Z., Wong, C., Fung, C., Xu, K., Tsang, H., “Mid-infrared grating couplers for silicon-on-sapphire wavguides”, *IEEE Photonics Journal,* vol. 4(1), 2012

[72] Michaels, A., Yablonovitch, E., “Inverse design of near unity efficiency perfectly vertical grating couplers”, *Optics Express,* vol. 26(4), 2018

[73] Chrostowski, L., Hochberg, M., *Silicon Photonics Design: From Devices to Systems,* Cambridge University Press, 2015

[74] Marchetti, R., Lacava, C., Khokhar, A., Chen, X., Cristiani, I., Richardson, D., Reed, G., Petropoulos, P., Minzioni, P., “High-efficiency gratin-couplers: demonstration of a new design strategy”, *Scientific Reports,* vol. 7(16670), 2017

[75] Ansys Lumerical, *Inverse Design of Grating Coupler (2D)*, https://optics.ansys.com/hc/en-us/articles/360042800573-Inverse-Design-of-Grating-Coupler-2D-

[76] Heebner, J., Grover, R., Ibrahim, T., *Optical Microresonators: Theory, Fabrication and Applications,* Springer Series in Optical Sciences, 2008

[77] Gogaerts, W., De Heyn, P., Van Vaerenbergh, T., “Silicon microring resonators”, *Laser & Photonics Reviews,* vol. 6(1), 2012

[78] Nitkowski, A., Chen, L., Lipson, M., “Cavity-enhanced on-chip absorption spectroscopy using microring resonators”, *Optics Express,* vol. 16(16), 2008

[79] Selvaraja, S., Sethi, P., “Emerging Waveguide Technology”, IntechOpen, 2018

[80] “How to Use the Beam Envelopes Method for Wave Optics Simulations”, COMSOL, 2022, https://www.comsol.com/blogs/how-to-use-the-beam-envelopes-method-for-wave-optics-simulations/

[81] “Simulating Optical Waveguides with COMSOL Multiphysics”, COMSOL, 2022, https://www.comsol.com/video/waveguide-simulation-with-the-beam-envelope-method

[82] “Plane Wave and Beam Sources Simulation Object”, Ansys Lumerical, 2022, https://optics.ansys.com/hc/en-us/articles/360034382854-Plane-wave-and-beam-source-Simulation-object

[83] Liu, D., Nocedal, J., “On the Limited Memory Method for Large Scale Optimization”, *Mathematical Programming B*, vol. 45(3), 1989

[84] Ansys Lumerical, *Inverse Design of Grating Coupler (3D)*, https://optics.ansys.com/hc/en-us/articles/1500000306621-Inverse-design-of-grating-coupler-3D-

[85] Ura, S., Sunagawa, H., Suhara, T., Nishihara, H., “Focusing grating couplers for polarization detection”, *Journal of Lightwave Technology*, vol. 6(6), 1988

[86] GDSHelpers, QPIT Munster Revision, 2022, https://gdshelpers.readthedocs.io/en/latest/

[87] Huang, Y., Salih, K., Qiancheng, Z., Torun, R., Ozdal, B., “Silicon-on-sapphire waveguides design for mid-IR evanescent field absorption gas sensors”, *Optics Communications*, vol. 313, 2014

[88] Frei, W., “Using Perfectly Matched Layers and Scattering Boundary Conditions for Wave Electromagnetics Problems”, *COMSOL Blog*, 2015, https://www.comsol.com/blogs/using-

perfectly-matched-layers-and-scattering-boundary-conditions-for-wave-electromagnetics-problems/

[89] Hong, J., Spring, A., Qiu, F., Yokoyama, S., “A high efficiency silicon nitride waveguide grating coupler with a multilayer bottom reflector”, *Scientific Reports,* vol. 9 (12988), 2019

Appendix A: Properties and definitions of the total angular momentum operator

The operator for the total angular momentum of a rigid molecule is given by [29]

$$\hat{J}^2 = \hat{J}_x^2 + \hat{J}_y^2 + \hat{J}_z^2 = \hat{J}_X^2 + \hat{J}_Y^2 + \hat{J}_Z^2 \tag{A.1}$$

Where (x, y, z) are the coordinates in the molecule fixed frame and (X, Y, Z) are the coordinates in the space fixed frame.

Components of angular momentum commute between frames of reference, that is

$$\left[\hat{J}_i, \hat{J}_k\right] = 0, for\ i = x, y, z \quad k = X, Y, Z \tag{A.2}$$

As well, some important commutation relations are [7],

$$\left[\hat{J}^2, \hat{J}_x\right] = \left[\hat{J}^2, \hat{J}_X\right] = 0 \tag{A.3}$$

$$\left[\hat{J}^2, \hat{J}_y\right] = \left[\hat{J}^2, \hat{J}_Y\right] = 0 \tag{A.4}$$

$$\left[\hat{J}^2, \hat{J}_z\right] = \left[\hat{J}^2, \hat{J}_Z\right] = 0 \tag{A.5}$$

$$\left[\hat{H}_{rot}, \hat{J}^2\right] = 0 \tag{A.6}$$

$$\left[\hat{H}_{rot}, \hat{J}_Z\right] = 0 \tag{A.7}$$

$$\left[\hat{H}_{rot}, \hat{J}_z\right] = i\left(\frac{1}{2I_x} - \frac{1}{2I_y}\right)\left(\hat{J}_x \hat{J}_y + \hat{J}_y \hat{J}_x\right) \tag{A.8}$$

Appendix B: Coriolis Interactions in Symmetric Top Molecules

It is useful to identify the complete Hamiltonian ($\widehat{H}_c$) of a molecule by its vibronic ($\widehat{H}_v$) and rotational ($\widehat{H}_r$) components as follows:

$$\widehat{H}_c = \widehat{H}_v + \widehat{H}_r \tag{B.1}$$

In the case of a prolate symmetric top, the rotational portion of the Hamiltonian operator can be written as [12]:

$$\widehat{H}_r = B\hat{J}^2 + (A-B)\hat{J}_a^2 - 2A\hat{J}_a\hat{p}_a - 2B(\hat{J}_b\hat{p}_b + \hat{J}_c\hat{p}_c) \tag{B.2}$$

Where A and B are the molecular rotational constants, $\hat{J}_i$are the components of the total angular momentum in the molecular frame, and $\hat{p}_i$ are the components of the vibrational angular momentum in the molecular frame. The interaction of the rotational and vibrational angular momenta is given by the last two terms in the Hamiltonian, $\hat{J}_i\hat{p}_i$, these two terms can be considered as the Coriolis Hamiltonian $\widehat{H}_{corr}$. The basis set of wavefunctions under consideration will be of the form:

$$|r_i\ J\ K_a\rangle \tag{B.3}$$

Where r_i refer to the vibrational states subject to a Coriolis interaction due to the rotation of the molecule.

Ignoring the interaction terms in the rotational Hamiltonian results in the familiar outcome for the case of a prolate symmetric top, with non-vanishing matrix elements [32]:

$$\widehat{H}_{11} = \langle r_1\ J\ K_a|\widehat{H}_r|r_1\ J\ K_a\rangle = BJ(J+1) + (A-B)K_a^2 \tag{B.4}$$

$$\widehat{H}_{22} = \langle r_2\ J\ K_a|\widehat{H}_r|r_2\ J\ K_a\rangle = BJ(J+1) + (A-B)K_a^2 \tag{B.5}$$

The first interaction term in the rotational Hamiltonian has only one non-vanishing element given by [12, 13]:

$$\widehat{H}_{12} = \langle r_1\, J\, K_a | \widehat{H}_r | r_2\, J\, K_a \rangle = -2AK_a\xi \tag{B.6}$$

Where ξ is the Coriolis interaction parameter (in units of h/2π) defined as:

$$\xi = \langle r_1 | \hat{p}_a | r_2 \rangle \tag{B.7}$$

If the excitation of one component of a degenerate vibration results in states r_1 and r_2 interacting as in equation B.7, the coupling can be characterized by the principal vibrational quantum number $v = 1$ and angular momentum quantum number ℓ = ±1 such that

$$|r_1\rangle = \frac{1}{\sqrt{2}}[|v = 1\ \ \ell = 1\rangle + |v = 1\ \ell = -1\rangle] \tag{B.8}$$

$$|r_2\rangle = \frac{1}{\sqrt{2}}[|v = 1\ \ell = 1\rangle - |v = 1\ \ell = -1\rangle] \tag{B.9}$$

from which the matrix element for ξ (B.7) becomes $\xi\ \ell$

The second interaction term in the rotational Hamiltonian yields no matrix elements for the basis set of wavefunctions as the directional components of the vibrational angular momentum other than on the a-axis are zero [13]. The complete Hamiltonian can be factored into submatrices of the form,

$$\begin{bmatrix} \widehat{H}_{11} & \widehat{H}_{12} \\ \widehat{H}_{12} & \widehat{H}_{22} \end{bmatrix} \tag{B.10}$$

from which the rotational energy eigenvalues can be determined as [32, 33]:

$$E = BJ(J+1) + (A-B)K_a^2 \pm 2AK_a\xi\ell \tag{B.11}$$

Similarly, for an oblate symmetric top one obtains:

$$E = BJ(J+1) + (C-B)K_c^2 \pm 2CK_c\xi\ell \qquad \text{(B.12)}$$

Appendix C: Characterizing the Rotational Symmetry of CO_2-Kr

To determine the transformation properties of an asymmetric top molecule like CO_2-Kr the effect of the rotation operators (R_z^{β}, R_{α}^{π}) must first be applied to a symmetric top wavefunction ($|JKM\rangle$), where R_z^{β} is a rotation of β radians about the z-axis, R_{α}^{π} is a rotation of π radians about an axis in the *xy*-plane making an angle α with the x-axis, and $|JKM\rangle$ is the wavefunction of the molecule with quantum numbers *J* (total angular momentum), *K* (projection of the total angular momentum onto the symmetry axis of the molecule in the molecules frame), and *M* (projection of total angular momentum in the lab-frame). *J* is an integer 0,1,2…, *K* and *M* run from ± *J*. Applying the rotation operators to the symmetric top wavefunctions is done via the following formula:

Prolate symmetric tops [29]:

$$R_z^{\beta}|JK_aM\rangle = e^{ik\beta}|JK_aM\rangle \tag{C.2}$$

$$R_{\alpha}^{\pi}|JK_aM\rangle = (-1)^J e^{-2Jik\alpha}|J-K_aM\rangle \tag{C.3}$$

$$R^0 = R^0{}_z \quad R^{\pi}{}_a = R^{\pi}{}_z \quad R^{\pi}{}_c = R^{\pi}{}_0 \quad R^{\pi}{}_b = R^{\pi}{}_{\pi/2} \tag{C.4}$$

Oblate symmetric tops [29]:

$$R_z^{\beta}|JK_cM\rangle = e^{ik\beta}|JK_cM\rangle \tag{C.5}$$

$$R_{\alpha}^{\pi}|JK_cM\rangle = (-1)^J e^{-2Jik\alpha}|J-K_cM\rangle \tag{C.6}$$

$$R^0 = R^0{}_z \quad R^{\pi}{}_a = R^{\pi}{}_0 \quad R^{\pi}{}_c = R^{\pi}{}_z \quad R^{\pi}{}_b = R^{\pi}{}_{\pi/2} \tag{C.7}$$

Applying (C.2) and (C.3) in the case of a prolate symmetric top we obtain the following:

For $k_a = 0$:

$$R_z^0|J0M\rangle = |J0M\rangle \tag{C.8}$$

$$R_z^{\pi}|J0M\rangle = |J0M\rangle \tag{C.9}$$

$$R_0^{\pi}|J0M\rangle = (-1)^J|J0M\rangle \quad \text{(C.10)}$$

$$R_{\pi/2}^{\pi}|J0M\rangle = (-1)^J|J0M\rangle \quad \text{(C.11)}$$

For $k_a = \pm k_a$:

$$R_z^0|JK_aM\rangle = |JK_aM\rangle \quad \text{(C.12)}$$

$$R_z^{\pi}|JK_aM\rangle = (-1)^{K_a}|JK_aM\rangle \quad \text{(C.13)}$$

$$R_0^{\pi}|JK_aM\rangle = (-1)^J|J{-K_a}M\rangle \quad \text{(C.14)}$$

$$R_{\pi/2}^{\pi}|JK_aM\rangle = (-1)^{J+K_a}|J{-K_a}M\rangle \quad \text{(C.15)}$$

$$R_z^0|J{-K_a}M\rangle = |J{-K_a}M\rangle \quad \text{(C.16)}$$

$$R_z^{\pi}|J-K_aM\rangle = (-1)^{K_a}|J{-K_a}M\rangle \quad \text{(C.17)}$$

$$R_0^{\pi}|J-K_aM\rangle = (-1)^J|JK_aM\rangle \quad \text{(C.18)}$$

$$R_{\pi/2}^{\pi}|J{-K_a}M\rangle = (-1)^{J+K_a}|JK_aM\rangle \quad \text{(C.19)}$$

The character representation of the wavefunction is obtained from the trace of the rotation operator in matrix form. This is done as follows:

For $k_a = 0$:

$$\chi(R_z^0) = tr\begin{bmatrix}1 & 0\\ 0 & 0\end{bmatrix} = 1 \quad \text{(C.20)}$$

$$\chi(R_z^{\pi}) = tr\begin{bmatrix}1 & 0\\ 0 & 0\end{bmatrix} = 1 \quad \text{(C.21)}$$

$$\chi(R_0^{\pi}) = tr\begin{bmatrix}(-1)^J & 0\\ 0 & 0\end{bmatrix} = (-1)^J \quad \text{(C.22)}$$

$$\chi\left(R_{\pi/2}^{\pi}\right) = tr\begin{bmatrix}(-1)^J & 0\\ 0 & 0\end{bmatrix} = (-1)^J \quad \text{(C.23)}$$

For $k_a = \pm k_a$:

$$\chi(R_z^0) = tr\begin{bmatrix}1 & 0\\ 0 & 1\end{bmatrix} = 2 \quad \text{(C.24)}$$

$$\chi(R_z^{\pi}) = tr\begin{bmatrix}(-1)^{K_a} & 0\\ 0 & (-1)^{K_a}\end{bmatrix} = 2(-1)^{K_a} \quad \text{(C.25)}$$

$$\chi(R_0^{\pi}) = tr\begin{bmatrix}0 & (-1)^{J}\\ (-1)^{J} & 0\end{bmatrix} = 0 \quad \text{(C.26)}$$

$$\chi\left(R_{\pi/2}^{\pi}\right) = tr\begin{bmatrix}0 & (-1)^{J+K_a}\\ (-1)^{J+K_a} & 0\end{bmatrix} = 0 \quad \text{(C.27)}$$

This leads to the following reducible representation:

Table C1: Reducible character representation for rotational states of prolate symmetric top wavefunction

Eq. Rot.	R^0	R^{π}_z	$R^{\pi}_{\pi/2}$	R^{π}_0
Γ (k_a=0)	1	1	$(-1)^J$	$(-1)^J$
Γ (k_a=±k_a)	2	$2(-1)^{ka}$	0	0

Applying the reduction formula to Table C1 we can obtain the irreducible representation of Table C1 as:

k_a = 0, J = even :

$$\#\ A_1 = ¼\ [\ (1•1•1)+(1•1•1)+(1•1•1)+(1•1•1)] = A_1 \quad \text{(C.28)}$$

$$\#\ A_2 = ¼\ [\ (1•1•1)+(1•1•1)+(-1•1•1)+(-1•1•1)] = 0A_2 \quad \text{(C.29)}$$

$$\#\ B_1 = ¼\ [\ (1•1•1)+(-1•1•1)+(1•1•1)+(-1•-1•1)] = 0B_1 \quad \text{(C.30)}$$

$$\#\ B_2 = ¼\ [\ (1•1•1)+(-1•1•1)+(-1•1•1)+(1•1•1)] = 0B_2 \quad \text{(C.31)}$$

$$\Gamma_{rot} = A_1 \quad \text{(C.32)}$$

By the same method we can calculate the following:

k_a = 0, J =odd :

$$\Gamma_{rot} = A_2 \tag{C.33}$$

k_a = even :

$$\Gamma_{rot} = A_1 + A_2 \tag{C.34}$$

k_a = odd :

$$\Gamma_{rot} = B_1 + B_2 \tag{C.35}$$

Included next are the same calculations done for an oblate symmetric top (explanation of steps omitted, but same as in the case of prolate top):

For $k_c = 0$:

$$R_z^0|J0M\rangle = |J0M\rangle \tag{C.36}$$

$$R_z^\pi|J0M\rangle = |J0M\rangle \tag{C.37}$$

$$R_0^\pi|J0M\rangle = (-1)^J|J0M\rangle \tag{C.38}$$

$$R_{\pi/2}^\pi|J0M\rangle = (-1)^J|J0M\rangle \tag{C.39}$$

For $k_c = \pm k_c$:

$$R_z^0|JK_cM\rangle = |JK_cM\rangle \tag{C.40}$$

$$R_z^\pi|JK_cM\rangle = (-1)^{K_c}|JK_cM\rangle \tag{C.41}$$

$$R_0^\pi|JK_cM\rangle = (-1)^J|J-K_cM\rangle \tag{C.42}$$

$$R_{\pi/2}^\pi|JK_cM\rangle = (-1)^{J+K_c}|J-K_cM\rangle \tag{C.43}$$

$$R_z^0|J-K_cM\rangle = |J-K_cM\rangle \tag{C.44}$$

$$R_z^\pi|J-K_cM\rangle = (-1)^{K_c}|J-K_cM\rangle \tag{C.45}$$

$$R_0^\pi|J-K_cM\rangle = (-1)^J|JK_cM\rangle \tag{C.46}$$

$$R_{\pi/2}^\pi|J-K_cM\rangle = (-1)^{J+K_c}|JK_cM\rangle \tag{C.47}$$

For $k_c = 0$:

$$\chi(R_z^0) = tr\begin{bmatrix}1 & 0\\ 0 & 0\end{bmatrix} = 1 \tag{C.48}$$

$$\chi(R_z^\pi) = tr\begin{bmatrix}1 & 0\\ 0 & 0\end{bmatrix} = 1 \tag{C.49}$$

$$\chi(R_0^\pi) = tr\begin{bmatrix}(-1)^J & 0\\ 0 & 0\end{bmatrix} = (-1)^J \tag{C.50}$$

$$\chi\left(R_{\pi/2}^\pi\right) = tr\begin{bmatrix}(-1)^J & 0\\ 0 & 0\end{bmatrix} = (-1)^J \tag{C.51}$$

For $k_c = \pm k_c$:

$$\chi(R_z^0) = tr\begin{bmatrix}1 & 0\\ 0 & 1\end{bmatrix} = 2 \tag{C.52}$$

$$\chi(R_z^\pi) = tr\begin{bmatrix}(-1)^{K_c} & 0\\ 0 & (-1)^{K_c}\end{bmatrix} = 2(-1)^{K_c} \tag{C.53}$$

$$\chi(R_0^\pi) = tr\begin{bmatrix}0 & (-1)^J\\ (-1)^J & 0\end{bmatrix} = 0 \tag{C.54}$$

$$\chi\left(R_{\pi/2}^\pi\right) = tr\begin{bmatrix}0 & (-1)^{J+K_c}\\ (-1)^{J+K_c} & 0\end{bmatrix} = 0 \tag{C.55}$$

Table C2: Reducible character representation for rotational states of oblate symmetric top wavefunction

Eq. Rot.	R^0	R^π_0	R^π_z	$R^\pi_{\pi/2}$
Γ (k_a=0)	1	$(-1)^J$	1	$(-1)^J$
Γ (k_c=±k_c)	2	0	$2(-1)^{kc}$	0

$k_c = 0$, J = even:

$$\#\ A_1 = ¼\ [\ (1•1•1)+(1•1•1)+(1•1•1)+(1•1•1)] = 1A_1 \tag{C.56}$$

$$\#\ A_2 = \tfrac{1}{4}\ [\ (1\bullet1\bullet1)+(1\bullet1\bullet1)+(-1\bullet1\bullet1)+(-1\bullet1\bullet1)] = 0A_2 \quad \text{(C.57)}$$

$$\#\ B_1 = \tfrac{1}{4}\ [\ (1\bullet1\bullet1)+(-1\bullet1\bullet1)+(1\bullet1\bullet1)+(-1\bullet\text{-}1\bullet1)] = 0B_1 \quad \text{(C.58)}$$

$$\#\ B_2 = \tfrac{1}{4}\ [\ (1\bullet1\bullet1)+(-1\bullet1\bullet1)+(-1\bullet1\bullet1)+(1\bullet1\bullet1)] = 0B_2 \quad \text{(C.59)}$$

$$\Gamma_{rot} = A_1 \quad \text{(C.60)}$$

$k_c = 0$, J =odd:

$$\Gamma_{rot} = B_2 \quad \text{(C.61)}$$

k_c = even:

$$\Gamma_{rot} = A_1 + B_2 \quad \text{(C.62)}$$

k_c = odd:

$$\Gamma_{rot} = A_2 + B_1 \quad \text{(C.63)}$$

The symmetry species of the asymmetric top (CO_2-Kr) is then determined by correlating between the findings for the oblate and prolate symmetric top. The result, which depends on the state of K_a and K_c is as follows:

Table C3: Rotational symmetry species of CO_2-Kr

Γ_{rot}	k_a k_c
A_1	ee
A_2	eo
B_1	oo
B_2	oe

Appendix D: Selection Rules for Rovibronic Transitions in CO_2-Kr and CO2-D_2O/HDO

Selection rules for CO2-Kr

We first consider the rovibrational selection rules for trantisions from the degenerate intramolecular bending state of CO_2 to a state with one quantum of excitation of the intramolecular bend plus a quantum of excitation of the asymmetric stretching of the CO_2 unit. The in-plane and out-of-plane bends were determined to have symmetries of A_1 and B_1 respectively, while the asymmetric stretch was determined to have symmetry of B_2. Using these symmetries we can determine that these transitions are both vibrationally and rovibrationally allowed. First, using Equation 2.59, we can determine that they are vibrationally allowed.

$$\text{In-plane: } (A_1 \otimes B_2) \otimes A_1 \otimes (A_1 \otimes B_2) \supset A_1 \text{ (allowed)} \tag{D.1}$$

$$\text{Out-of-plane: } (B_1 \otimes B_2) \otimes A_1 \otimes (B_1 \otimes B_2) \supset A_1 \text{ (allowed)} \tag{D.2}$$

Then using the rovibronic selection rules from Equation 2.61 (in-plane):

Table D1: Rovibronic states for in-plane CO_2 bend + asymmetric stretch

Γ_{rot}	Γ^{vib}_{init}	Γ^{vib}_{final}	Γ^{rve}_{init}	Γ^{rve}_{init}
A_1 (ee)	A_1	B_2	A_1 (ee)	B_2 (ee)
A_2 (eo)	A_1	B_2	A_2 (eo)	B_1 (eo)
B_1 (oo)	A_1	B_2	B_1 (oo)	A_2 (oo)
B_2 (oe)	A_1	B_2	B_2 (oe)	A_1 (oe)

$$A_1(\text{ee}) \otimes A_2(oo) \supset A_2 \text{ (allowed)} \tag{D.3}$$

$$A_2(\text{eo}) \otimes A_1(oe) \supset A_2 \text{ (allowed)} \tag{D.4}$$

$$B_1(\text{oo}) \otimes B_2(ee) \supset A_2 \text{ (allowed)} \tag{D.5}$$

$$B_2(\text{oe}) \otimes B_1(eo) \supset A_2 \text{ (allowed)} \quad \text{(D.6)}$$

Table D2: Rovibronic transition types for in-plane CO_2 bend + asymmetric stretch

Δk_a	Δkc	Transition Type
± 1	± 1	b-type

Rovibronic selection rules (out-of-plane):

Table D3: Rovibronic states for out-of-plane CO_2 bend + asymmetric stretch

Γ_{rot}	Γ^{vib}_{init}	Γ^{vib}_{final}	Γ^{rve}_{init}	Γ^{rve}_{init}
A_1 (ee)	B_1	A_2	B_1 (ee)	A_2 (ee)
A_2 (eo)	B_1	A_2	B_2 (eo)	A_1 (eo)
B_1 (oo)	B_1	A_2	A_1 (oo)	B_2 (oo)
B_2 (oe)	B_1	A_2	A_2 (oe)	B_1 (oe)

$$A_1(\text{oo}) \otimes A_2(ee) \supset A_2 \text{ (allowed)} \quad \text{(D.7)}$$

$$A_2(\text{oe}) \otimes A_1(eo) \supset A_2 \text{ (allowed)} \quad \text{(D.8)}$$

$$B_1(\text{ee}) \otimes B_2(oo) \supset A_2 \text{ (allowed)} \quad \text{(D.9)}$$

$$B_2(\text{eo}) \otimes B_1(oe) \supset A_2 \text{ (allowed)} \quad \text{(D.10)}$$

Table D4: Rovibronic transition types for out-of-plane CO_2 bend + asymmetric stretch

Δk_a	Δkc	Transition Type
± 1	± 1	b-type

Selection Rules for CO_2-D_2O

The total internal wavefunction for CO_2-D_2O must belong to the species A_1' *or* A_2', as the wavefunction must be invariant under permutation of both sets of identical bosons (O in the CO_2 unit and D in the D_2O unit). Having already determined the symmetry of the rotational, spin and tunnelling states (which are the same as CO_2-H_2O) the transitions connecting the ground state to the CO_2 ν_3 asymmetric stretching state and the D_2O ν_3 asymmetric stretching state can be determined as follows

For the ground (A_1') to CO_2 ν_3 asymmetric stretching state (B_2') transition:

Table D5: Calculated symmetries of the total internal wavefunction of the ground vibrational state of CO_2-D_2O

$\Gamma_{rot} \otimes \Gamma_{spin} \otimes \Gamma_{tun} \otimes \Gamma_{vib}$	$\Gamma_{tot} = A_1'$ or A_2'
A_1' (ee) A_2' (eo) B_1'(oo) B_2' (oe) $\otimes$ A_1' (6) B_2'' (3) $\otimes$ A_1' A_1'' $\otimes$ A_1'	$6A_1'$ (ee, A_1') $6A_2'$ (eo, A_1') $3A_2'$ (oo, A_1'') $3A_1'$ (oe, A_1'')

Table D6: Calculated symmetries of the total internal wavefunction of the CO_2 ν_3 asymmetric stretching state of CO_2-D_2O

$\Gamma_{rot} \otimes \Gamma_{spin} \otimes \Gamma_{tun} \otimes \Gamma_{vib}$	$\Gamma_{tot} = A_1'$ or A_2'
A_1' (ee) A_2' (eo) B_1'(oo) B_2' (oe) $\otimes$ A_1' (6) B_2'' (3) $\otimes$ A_1' A_1'' $\otimes$ B_2'	$3A_1'$ (ee, A_1'') $3A_2'$ (eo, A_1'') $6A_2'$ (oo, A_1') $6A_1'$ (oe, A_1')

Table D7: Determination of the ground-to-CO_2 asymmetric stretching vibration transition for the CO_2-D_2O complex

Γ_{init}^{rve}	⊗	Γ_{final}^{rve}	⊃A_2'
$6A_1'$ (ee, A_1')		$3A_1'$ (ee, A_1'')	$6A_1'$ (ee, A_1') → $6A_2'$ (oo, A_1')
$6A_2'$ (eo, A_1')	⊗	$3A_2'$ (eo, A_1'')	$6A_2'$ (eo, A_1') → $6A_1'$ (oe, A_1')
$3A_2'$ (oo, A_1'')		$6A_2'$ (oo, A_1')	$3A_2'$ (oo, A_1'') → $3A_1'$ (ee, A_1'')
$3A_1'$ (oe, A_1'')		$6A_1'$ (oe, A_1')	$3A_1'$ (oe, A_1'') → $3A_2'$ (eo, A_1'')

The transition from the ground vibrational state to the CO_2 asymmetric stretching state is a *b*-type transition ($\Delta k_a = \pm 1$, $\Delta k_c = \pm 1$). This transition connects the (ee) and (eo) rotational states in the lower tunnelling state (A_1') of the ground vibrational state to the (oo) and (oe) rotational states in the lower tunnelling state of the CO_2 asymmetric stretch as well as the (oo) and (oe) states in the upper tunnelling state (A_1'') of the ground vibrational state to the (ee) and (eo) states in the upper tunnelling state of the CO_2 asymmetric stretch. These transitions are depicted below

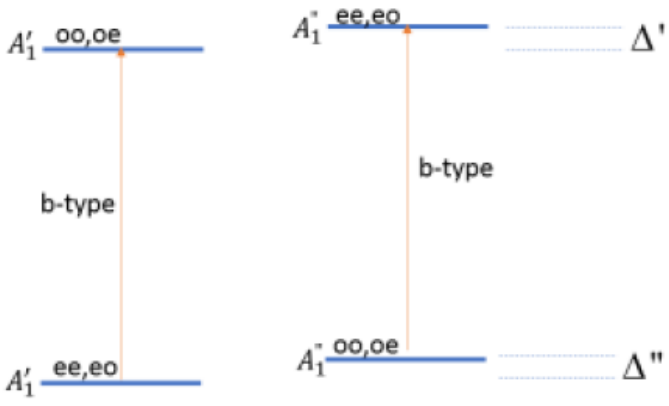

Figure D1: Tunneling diagram for the CO_2 ν_3 transition of CO_2-D_2O. Δ' and Δ'' indicate the tunneling splitting's for the ground and excited states

For the ground (A_1') to D_2O ν_3 asymmetric stretching state (B_2'') transition:

Table D8: Calculated symmetries of the total internal wavefunction of the D_2O ν_3 asymmetric stretching state of CO_2-D_2O

$\Gamma_{rot} \otimes \Gamma_{spin} \otimes \Gamma_{tun} \otimes \Gamma_{vib}$					$\Gamma_{tot} = A_1'$ or A_2'
A_1' (ee) A_2' (eo) B_1'(oo) B_2' (oe)	$\otimes$	A_1' (6) B_2'' (3)	$\otimes$	A_1' A_1''	$\otimes$ B_2''	$3A_1'$ (ee, A_1') $3A_2'$ (eo, A_1') $6A_2'$ (oo, A_1'') $6A_1'$ (oe, A_1'')

Table D9: Determination of the ground-to-D_2O asymmetric stretching vibration transition for the CO_2-H_2O complex

Γ_{init}^{rve}	$\otimes$	Γ_{final}^{rve}	$\supset A_2'$
$6A_1'$ (ee, A_1')		$3A_1'$ (ee, A_1')	$6A_1'$ (ee, A_1') → $6A_2'$ (oo, A_1'')
$6A_2'$ (eo, A_1')		$3A_2'$ (eo, A_1')	$6A_2'$ (eo, A_1') → $6A_1'$ (oe, A_1'')
$3A_2'$ (oo, A_1'')	$\otimes$	$6A_2'$ (oo, A_1'')	$3A_2'$ (oo, A_1'') → $3A_1'$ (ee, A_1')
$3A_1'$ (oe, A_1'')		$6A_1'$ (oe, A_1'')	$3A_1'$ (oe, A_1'') → $3A_2'$ (eo, A_1')

The transition from the ground vibrational state to the D_2O asymmetric stretching state is a *b*-type transition ($\Delta k_a = \pm 1$, $\Delta k_c = \pm 1$). This transition connects the (ee) and (eo) rotational states in the lower tunnelling state (A_1') of the ground vibrational state to the (oo) and (oe) rotational states in the upper tunnelling state (A_1'') of the D_2O asymmetric stretch as well as the (oo) and (oe) states in the upper tunnelling state of the ground vibrational state to the (ee) and (eo) states in the lower tunnelling state of the D_2O asymmetric stretch. These transitions are depicted below

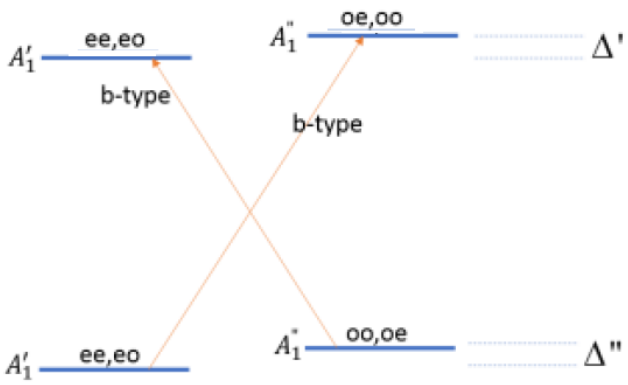

Figure D2: Tunneling diagram for the D_2O ν_3 transition of CO_2-D_2O. Δ' and Δ'' indicate the tunneling splitting's for the ground and excited states

Selection Rules for CO_2-HDO

For the ground (A_1) to OH stretching state (A_1) transition:

The total internal wavefunction for CO_2-HDO must belong to the species A_1 *or* A_2 , as the wavefunction must be invariant under permutation of the identical bosons in the molecule (O in the CO_2 unit). Having already determined the symmetry of the rotational, spin and tunnelling states the transitions connecting the ground state to the OD stretching state can be determined as follows

Table D10: Calculated symmetries of the total internal wavefunction of the ground state and the OD stretching state of CO_2-HDO

$\Gamma_{rot} \otimes \Gamma_{spin} \otimes \Gamma_{tun} \otimes \Gamma_{vib}$						Γ_{tot} = A_1 or A_2
A_1 (ee) A_2 (eo) B_1 (oo) B_2 (oe)	⊗	A_1 (1)	⊗	A_1 B_2	⊗	A_1	A_1 (ee, A_1) A_2 (eo, A_1) A_2 (oo, B_2) A_1 (oe, B_2)

Table D11: Determination of the ground-to-OD stretching vibration transition for the CO_2-HDO complex

Γ_{init}^{rve}	⊗	Γ_{final}^{rve}	⊃A_2
A_1 (ee, A_1)		A_1 (ee, A_1)	A_1 (ee, A_1) → A_2 (eo, A_1), A_2 (oo, B_2)
A_2 (eo, A_1)	⊗	A_2 (eo, A_1)	A_2 (eo, A_1) → A_1 (ee, A_1), A_1 (oe, B_2)
A_2 (oo, B_2)		A_2 (oo, B_2)	A_2 (oo, B_2) → A_1 (ee, A_1), A_1 (oe, B_2)
A_1 (oe, B_2)		A_1 (oe, B_2)	A_1 (oe, B_2) → A_2 (eo, A_1), A_2 (oo, B_2)

The transition from the ground vibrational state to the OD stretching state is represented by a two hybrid *a*- *(Δk_a=0, Δk_c=$\pm$1).*, *b*-type transitions *(Δk_a=$\pm$1, Δk_c=$\pm$1).*

The *b*-type transitions connect the (ee) and (eo) rotational states in the lower tunnelling state (A_1) of the ground vibrational state to the (oo) and (oe) rotational states in the upper tunnelling state (B_2) of the OD stretch as well as the (oo) and (oe) states in the upper tunnelling state of the ground vibrational state to the (ee) and (eo) states in the lower tunnelling state of the OD stretch

The *a*-type transitions connect the (ee) and (eo) rotational states in the lower tunnelling state (A_1) of the ground vibrational state to the (ee) and (eo) rotational states in the lower tunnelling state of the OD stretch as well as the (oo) and (oe) states in the upper tunnelling state of the ground vibrational state to the (oo) and (oe) states in the upper tunnelling state of the OD stretch. The *a*-type transitions will appear as weaker lines in the spectra due to the protection of the transition moment onto the *a*-axis being smaller than for the *b*-axis. These transitions are depicted below

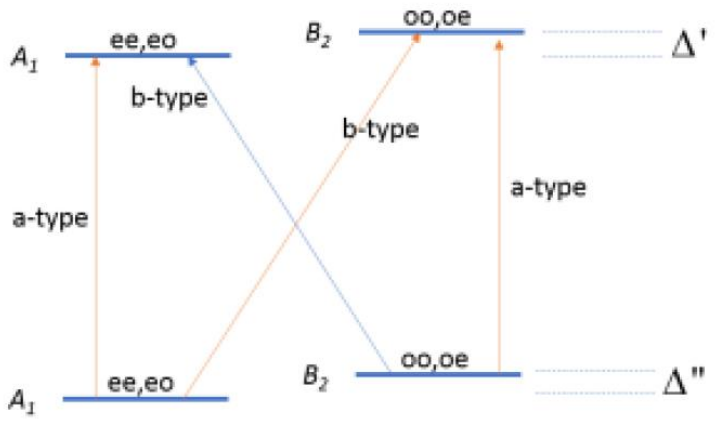

Figure D3: Tunneling diagram for the OH stretching transition of CO_2-HDO. Δ' and Δ'' indicate the tunneling splitting's for the ground and excited states

Appendix E: Evanescent Field Ratio (EFR) of SoS Waveguide

The ERF (η) of a rib waveguide can be written as [87], where **S** is denoted as the typical Poynting vector.

$$\eta = \frac{\iint_{clad} \vec{S}\cdot\vec{n}\, dx\, dy}{\iint_{\infty} \vec{S}\cdot\vec{n}\, dx\, dy} \tag{E.1}$$

This surface integration is carried out directly in COMSOL for varying TE waveguide geometries and is shown in Figure E1.

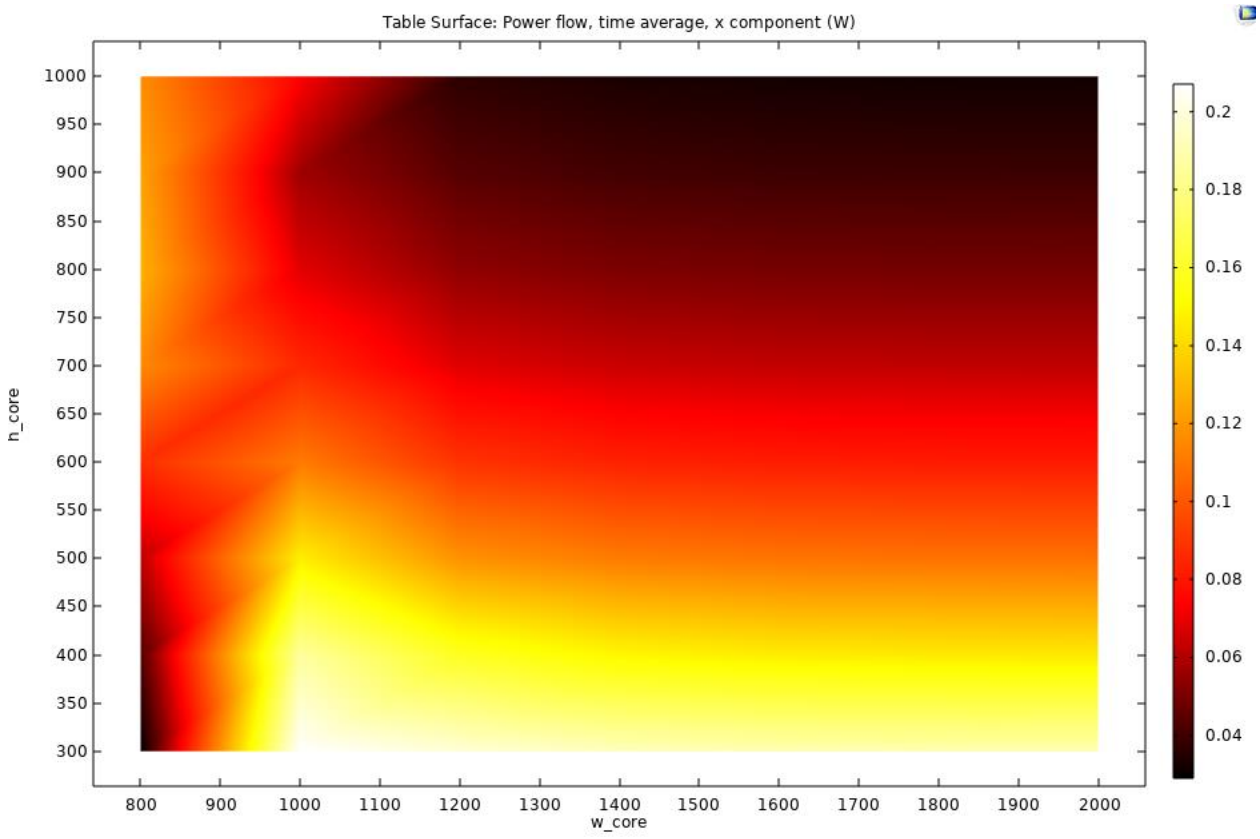

Figure E1: EFR as a function of waveguide core width and height for an air clad SoS wafer

This surface integration agrees well with other theoretical values reported in a SoS waveguide sensing analysis by Huang *et al.* [87].

Appendix F: FDTD Boundary Conditions

Due to the computational limitations imposed by large scale optical FDTD models it is necessary to restrict the total simulation domain to a manageable size such that solutions of the electromagnetic wave equations can be solved for sufficiently small mesh. While it would be preferable to expand the total simulation domain to as large a size as possible to best approximate real world light-matter interactions this would come at great computational cost. As such most FDTD models can approximate light waves escaping the simulation domain and travelling to an infinite distance by the imposition of either scattering boundary conditions or perfectly matched layers.

In order to truncate the simulation domain in FDTD solvers it is necessary to impose a physical boundary in the simulation that reduces reflections of the propagating fields at the boundary back into the simulation region. This is approximated in COMSOL (and other FDTD solvers) as either a first or second order scattering boundary or a perfectly matched layer at the utmost exterior of the geometry. If one assumes an electromagnetic wave propagation in the xy-plane, polarized in the z-direction, then a first order boundary condition can be imposed as a line (2D) or plane (3D) in the geometry that takes the form [88]

$$\mathbf{n} \cdot (\nabla E_z) + ik_0 E_z = 0 \tag{F.1}$$

Where **E** is the electric field and *k* is the wave number. This condition is exactly non-reflecting if the angle of incidence on the boundary is 90 degrees; all other scattering angles are partially reflected. Taking the tangential derivative of the first order condition yields a second order boundary of the form [88]

$$\mathbf{n} \cdot (\nabla E_z) + ik_0 E_z - \frac{i}{2k_0}\nabla_t^2 E_z = 0 \tag{F.2}$$

This boundary condition reflects less over a broader range of incidence angles thus better approximating a real-world scenario for long range electromagnetic wave dynamics.

If the geometry of the system under study allows, one may also model a domain at the exterior of the simulation which absorbs rather than reflects outgoing waves; these domains are called perfectly matched layers (PML). A PML is a domain with an anisotropic and complex valued permittivity and permeability [88]. Discretization of the domain by mesh elements results in some reflection at the PML boundary which cannot be totally removed, however this reflection is noticeably smaller than its scattering condition counterparts. These domains are modelled as any other physical domain in the simulation and include a mesh size in which the wave equation is discretely solved. The use of a PML in FDTD simulation requires that the model in question belongs to either a purely cartesian, cylindrical, or spherical geometric structure and as such a PML may not always be a viable boundary choice.

Figure F1 gives a general idea of the reflectivity of these boundary conditions in terms of scattering angle. Clearly a PML layer is a preferred choice as a boundary condition as it reduces reflectivity over a broader incidence angle, however given the geometry of systems under study it may not always be viable.

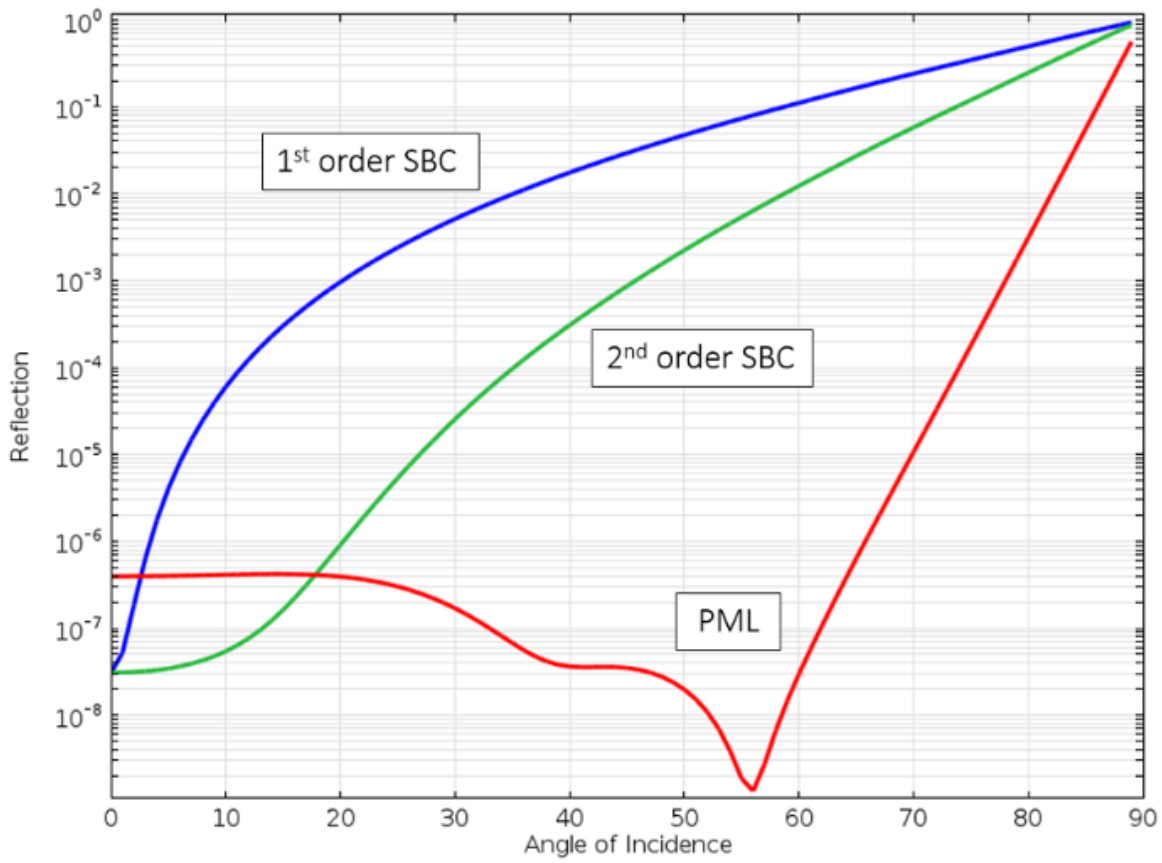

Figure F1: Reflection of FDTD electromagnetic waves at various types of boundary conditions by angle of incidence [88]

In this thesis analysis, waveguide mode calculations were carried out with the use of a cartesian PML layer in COMSOL as the rectangular nature of the waveguide structure allows for modelling of a cartesian PML. Ring resonator analysis was implemented with a second ordering boundary condition in COMSOL due to geometric considerations. Two-dimensional and three-dimensional grating simulations were modelled with a PML layer in Lumerical at the simulation extremes.